Motion-Compensation for Complementary-Coded Medical Ultrasonic Imaging

Cormac Cannon

A thesis submitted for the degree of Doctor of Philosophy.
The University of Edinburgh.
October 2009

Abstract

Ultrasound is a well-established tool for medical imaging. It is non-invasive and relatively inexpensive, but the severe attenuation caused by propagation through tissue limits its effectiveness for deep imaging. In recent years, the ready availability of fast, inexpensive computer hardware has facilitated the adoption of signal coding and compression techniques to counteract the effects of attenuation. Despite widespread investigation of the topic, published opinions vary as to the relative suitability of discrete-phase-modulated and frequency-modulated (or continuous-phase-modulated) signals for ultrasonic imaging applications. This thesis compares the performance of discrete binary-phase coded pulses to that of frequency-modulated pulses at the higher imaging frequencies at which the effects of attenuation are most severe.

The performance of linear and non-linear frequency modulated pulses with optimal side-lobe characteristics is compared to that of complementary binary-phase coded pulses by simulation and experiment. Binary-phase coded pulses are shown to be more robust to the affects of attenuation and non-ideal transducers. The comparatively poor performance of frequency-modulated pulses is explained in terms of the spectral characteristics of the signals and filters required to reduce side-lobes to levels acceptable for imaging purposes.

In theory, complementary code sets like bi-phase Golay pairs offer optimum side-lobe performance at the expense of a reduction in frame rate. In practice, misalignment caused by motion in the medium can have a severe impact on imaging performance. A novel motion-compensated imaging algorithm designed to reduce the occurrence of motion artefacts and eliminate the reduction in frame-rate associated with complementary-coding is presented. This is initially applied to conventional sequential-scan B-mode imaging then adapted for use in synthetic aperture B-mode imaging. Simulation results are presented comparing the performance of the motion-compensated sequential-scan and synthetic aperture systems with that of simulated systems using uncoded and frequency-modulated excitation pulses.

Declaration of Originality

I hereby declare that the research recorded in this thesis and the thesis itself was composed and originated entirely by myself in the School of Engineering at The University of Edinburgh.

Cormac Cannon

Acknowledgements

I would like to thank my supervisors, John and Steve, for their guidance in matters academic and understanding in relation to matters not-so over the course of the last few years. Breda, for putting up with a three-and-a-bit year long-distance relationship and my piping - though I'm sure the one made the other easier to bear - not to mention my flatmates, Piero and Matteo, for putting up with my piping at close range. Luis for good friendship and company, and for not mentioning the thesis any more than was absolutely necessary. Anne & Jim; Jamie & Laura; and Lamond & Sally for providing safe havens in Glasgow and Edinburgh for an Irishman abroad. Benjamin Lamboul, Michael Bennet, Said Assous and Claire Hopper for their assistance with experiments. My "aul' pair", Eamonn and Kathleen Cannon, for their unstinting support and care over the last 31 years. Willie Clancy, Padraig O'Keefe and Micí "Cúmbá" O'Sullivan for playing the music they did, and the collectors and folklorists who had the foresight to record them for the rest of us. I would also like to acknowledge the financial support of the BIAS project, which was funded by the Engineering and Physical Sciences Research Council (EPSRC), UK, as part of their Basic Technology Programme.

Contents

List of figures

List of tables

Nomenclature

α_a^b	Gain correction factor for motion within beam
α_k	Desired side-lobe level for Kaiser window function
β_k	Side-lobe/main-lobe argument to Kaiser window function
$\delta(t)$	The Dirac delta function
ϵ_a^b	Motion estimate error
λ	Signal wavelength
λ_t	Transducer "wavelength", $\frac{1}{B_t}$, a measure of axial resolution
$\phi[l]$	A discrete phase code
$\phi_c[n,l]$	A complementary set of discrete phase codes
$\phi(t)$	Phase modulation function
$\phi_{\text{nl}}(f)$	Desired phase spectrum of a non-linear FM signal
$\phi_{\text{nl}}[m]$	Discrete version of $\phi_{\text{nl}}(f)$
ρ	Density
ρ_p	Back-scattering coefficient
$\tau_f(e,j,l,t)$	Dynamic focusing delays for STA imaging
$\tau_f[e,j,l]$	Discrete focusing delays for STA imaging
$\tau_n[\vec{f}]$	Focusing delay for element n and focal vector $\vec{f}$
$\tau_n(\vec{l},t)$	Dynamic focusing delay function for element n and scan line $\vec{l}$
τ_a^b	Round-trip delay due to motion between acquisitions
$\tau_p[i,j,e]$	Bi-directional propagation delay for a point, p
θ_g	Grating lobe angle
$\theta_i(t)$	Instantaneous phase of a signal
A	Signal amplitude (constant)
$A_{\text{nl}}(f)$	Desired amplitude spectrum of an NLFM signal
$A_{\text{nl}}[m]$	Discrete version of $A_{\text{nl}}(f)$
B	Signal bandwidth
B_t	Transducer bandwidth
D_f	Depth of focus

$D_{\text{nl}}(f)$	Desired spectrum of NLFM signal
$D_{\text{nl}}[m]$	Discrete version of $D_{\text{nl}}(f)$
E	Number of elements in a synthetic transmit aperture
E_A	Total signal energy
$E(t)$	Signal energy as a function of time
F_f	f-number of an aperture
G_f	Focal gain of an aperture
$G(f)$	Fourier transform of an imaging pulse $g(t)$
I_0	The zeroth-order modified Bessel function
I_{pk}	Peak flux limit
I_{spta}	Spatial peak, temporal average incident flux
I_{sptp}	Spatial peak, temporal peak incident flux
$K(f)$	Kaiser window function
$K_t[n]$	Time normalisation factor for generalised NLFM polynomial
L	Length of a discrete phase code
N, N_c	Number of codes in a complementary set
N_{Acq}	Number of acquisitions required for a full B-mode scan
N_f	Number of transmit focal depths
N_l	Number of scan-lines
$P^a_{\text{Ch}}(x)$	a^{th} term of the Chebyshev polynomial of x
P_{noise}	Thermal noise at room temperature
SNR_{inh}	Inherent SNR of a pulse-echo imaging system
T	Pulse duration
T_a	Aperture-cycle duration
T_b	Duration of bit or “chip” period
T_r	Pulse repetition period, $\frac{1}{F_R}$
T_K	Temperature in degrees Kelvin
$W[\ldots,\ldots]$	Fourier matrix
$W_{\text{Ch}}(n)$	Dolphy-Chebyshev window function
$W_{\text{ET}}(n)$	Elliptical-Tukey window function
Z	Specific Acoustic Impedance
$a(t)$	Amplitude modulation function

$a_n[\vec{f}]$	Apodisation weighting for a given element, n, and focal vector, $\vec{f}$
$a_n(\vec{l}, t)$	Dynamic apodisation weighting function for element n and scan line $\vec{l}$
$a_r(t)$	Impulse response of receive aperture
$a_t(t)$	Impulse response of transmit aperture
$a_{tr}(t)$	Combined impulse response of transmit and receive apertures
$b(t)$	Basis or "chip" sequence for discrete-phase signal modulation
$b_{tr}(t)$	Basis sequence including effects of bi-directional transducer response
c	Speed of sound
$c[l]$	Sequence of complex phasors corresponding to the discrete phase sequence $\phi[l]$
$c_c[n, l]$	Complementary set of complex phasors sequences corresponding to $\phi[n, l]$
$c_{xx}[i]$	Discrete auto-correlation sequence of $c[l]$
$c(t)$	Continuous modulation sequence for a discrete-phase coded pulse
$c(n, t)$	Set of complementary continuous modulation sequences
$c_{xx}(\tau)$	Auto-correlation function of $c(t)$
$c_{xx}(n, \tau)$	Auto-correlation function of $c(n, t)$
e_i	Transducer element index
$\vec{f}$	Focusing vector
f_c	Pulse/transducer centre frequency
f_d	Frequency shift due to the Doppler effect
$f_d[m]$	A discrete set of frequencies
f_h	Upper limit of frequency band swept by an FM pulse
$f_i(t)$	Instantaneous frequency
f_l	Lower limit of frequency band swept by an FM pulse
f_r	Pulse repetition frequency
f_s	Sampling frequency
$g(t)$	Imaging pulse
$g_n(\vec{f}, t)$	Signal transmitted from element n of a focused array transducer
$g_{\text{cpc}}(n, t)$	Set of complementary discrete-phase coded pulses
$g_{\text{fm}}(n, t)$	Frequency-modulated pulse
$g_{\text{pc}}(n, t)$	Discrete-phase coded pulse
k_B	Boltzmann's constant, 1.3807×10^{-23} Joules per degree Kelvin
$m_c(\ldots, t)$	Compensated sum of complementary filter outputs
$m_m(\ldots, t)$	Mirror-compensated sum of complementary filter outputs

$m_s(\ldots,t)$	Reference / desired sum of complementary filter outputs
$m_u(\ldots,t)$	Uncompensated sum of complementary filter outputs
$m_{cc}(i,e,l,t)$	Aperture compensation block outputs
m_i	Aperture-cycle index
o_i	Code index
$q_c(i,l,t)$	Motion-compensated STA image
$q_u(i,l,t)$	Uncompensated STA image
r_a	Radius of a circular aperture
$r_p(i,j,t)$	Echo from point p at receiving element j during the i^{th} acquisition interval
$r(\ldots,t)$	Received ultrasonic echo signals
$r_f(\ldots,t)$	Compression filtered version of $r(\ldots,t)$
$r_c(\ldots,t)$	Motion-compensated compression-filter outputs
$r_s(\ldots,t)$	Reference / desired compression-filter outputs
$r_{bf}(\ldots,t)$	Beam-formed version of $r_f(\ldots,t)$ (STA only)
rect(t)	Rectangular function
rect$_c(t)$	Causal version of rect(t)
$s(i,j,t)$	Lumped scattering impulse response of receiving element j during acquisition interval i
$s_{bf}(i,t)$	Lumped reflectivity function
$s_p(i,j,t)$	Point impulse response
$s_p[i]$	Point spatial coordinates
$u(t)$	Heaviside step function
v	Velocity
$w(t)$	An analysis window function for Fourier analysis
$w_a(e,j,l,t)$	Dynamic apodisation weighting function for STA imaging
$w_a[e,j,l]$	Discrete apodisation weighting function for STA imaging
w_f	Beam width at focal point
z_f	Geometrical focal distance
z_A	Geometrical focal distance at which aperture is fully open
z_R	Rayleigh distance

Mathematical Symbols and Conventions

$\mathbb{N}_0$	The set of natural numbers including zero. $\mathbb{N}_0 = \{0, 1, 2, \ldots, \infty\}$
$\mathbb{N}_1$	The set of natural numbers excluding zero. $\mathbb{N}_1 = \{1, 2, \ldots, \infty\}$
$\mathbb{R}$	The set of rational numbers
$\lfloor a \rfloor$	Nearest integer less than or equal to some value $a \in \mathbb{R}$
$\lceil a \rceil$	Nearest integer greater than or equal to some value $a \in \mathbb{R}$
$a(t)$	A continuous sequence
$a[n]$	A discrete-valued sequence
$a\%n$	a modulo n, the remainder on division of a by n, i.e. $a - \lfloor \frac{a}{n} \rfloor n$
$\arg(x)$	Phase angle (or argument) of a complex phasor, x
$\mathcal{F}\{a\}$	The Fourier transform of a
$\mathcal{F}^{-1}\{a\}$	The inverse Fourier transform of a
$\mathcal{F}_M\{a\}$	The M-point discrete Fourier transform of a
$\mathcal{F}_M^{-1}\{a\}$	The M-point inverse discrete Fourier transform of a
$\tilde{a}$	Approximation to a
$\hat{a}$	Estimate of a

Acronyms and Abbreviations

A-mode	Amplitude mode
ADC	Analogue-to-Digital Converter
BFT	Beam-Formation Toolkit
BGS	British Geological Survey
BPC	Binary-Phase Coded
B-mode	Brightness Mode
CCM	Cross-Correlation Model
C3M	Complex Cross-Correlation Model
CFI	Colour Flow Imaging
CW	Continuous-Wave
DFT	Discrete Fourier Transform
EAM	Extended Auto-correlation Method
FDA	Federal Food and Drug Administration (USA)
FFT	Fast Fourier Transform
FM	Frequency-Modulated
FT	Fourier Transform
GSNR	Gain in Signal-to-Noise Ratio
LFM	Linear Frequency-Modulated
M-mode	Motion Mode
MI	Mechanical Index
NLFM	Non-Linear Frequency-Modulated
PRF	Pulse Repetition Frequency
PSF	Point Scattering Function
PW	Pulsed-Wave
Q-factor	Quality factor
RF	Radio-Frequency
SAU	Synthetic Aperture Ultrasound
SNR	Signal-to-Noise Ratio
SRA	Synthetic Receive Aperture

SSD	Sum Squared Difference
STA	Synthetic Transmit Aperture
STRA	Synthetic Transmit and Receive Aperture
TB-product	Time-Bandwidth product
TGC	Time-Gain Control
TI	Thermal Index

Chapter 1
Introduction

1.1 Background

The research described in this thesis was conducted under the aegis of the BIAS (Biologically Inspired Acoustic Systems) consortium, which was funded by the basic technology program of RCUK (Research Councils UK). The BIAS project brought together researchers working in a number of different disciplines and institutions throughout the UK with the goal of developing sonar technologies inspired by biosonar systems found in bats and aquatic mammals, which exhibit superior spatial resolution and material discrimination capabilities to current electronic systems. Some species of bat can consistently fly between a narrow gap between two wires of sub-wavelength diameter, while dolphins are capable of identifying different materials based on ultrasonic reflections. Both show evidence of excellent acoustic focusing characteristics and use complex modulated ultrasonic signals. The work presented in this thesis was part of a research strand within BIAS investigating the contributions that could be made to signal processing technologies in particular application areas. Its initial focus was on the application of coded waveforms in medical ultrasound imaging.

Ultrasound is a well-established tool for medical imaging. It is non-invasive and relatively inexpensive, but its range and resolution are limited by the severe attenuation caused by propagation through tissue. Attenuation causes the strength of reflected signals to decrease in proportion to propagation distance, limiting the depth from which clinically useful images may be obtained. Both resolution and the severity of the effects of attenuation increase in proportion to pulse centre frequency, so an increase in resolution typically comes at the expense of a reduction in depth of imaging.

Signal coding and compression techniques, using modulated signals like those found in bioacoustic systems, have been widely investigated as a method of overcoming this limitation. In recent years, the ready availability of fast, inexpensive computer hardware has facilitated the adoption of these techniques in commercial systems. There are varying opinions as to the relative suitability of discrete-phase modulated and frequency-modulated (or continuous-phase

modulated) signals for ultrasonic imaging applications. Complementary sets of coded signals offer optimum side-lobe performance in theory, though this comes at the expense of a reduction in frame rate. In practice, misalignment caused by motion in the medium can have a severe impact on side-lobe levels.

1.2 Contributions

This thesis describes a systematic comparison of the performance of binary-phase coded and frequency-modulated pulses for medical ultrasonic imaging, particularly at high pulse centre frequencies and in the presence of attenuation. A detailed review is presented of the current literature on signal and filter design for frequency-modulated ultrasonic imaging. The performance of complementary binary-phase coded waveforms is compared to that of linear and non-linear frequency-modulated pulses and a reference unmodulated sinusoidal pulse using results from computer-based imaging simulations and experiments conducted in collaboration with our research partners. These demonstrate the superior resolution properties of binary-phase coded signals and their increased robustness to the effects of the strong frequency-dependent attenuation caused by propagation through tissue. This robustness to attenuation is particularly evident at higher imaging frequencies, providing a significant increase in the depth in tissue from which clinically useful images may be obtained. A novel explanation is offered for this phenomenon based on the time-frequency characteristics of the different signal types.

Complementary binary-phase coded signals were found to combine robustness to attenuation with ideal side-lobe performance. Concern has been expressed in work published by other authors with regard to the potential degradation in side-lobe performance due to motion, while the increased number of pulse emissions required using sets of complementary signals can increase image acquisition time considerably. A novel algorithm for motion-compensated complementary-coded ultrasonic imaging was developed in response to these concerns. It is designed to reduce motion artefacts and allow data to be used recursively, eliminating the frame-rate reduction usually associated with complementary codes. Interpolated motion compensation is performed based on established methods of velocity estimation and mirrored compensation stages are used to reduce the occurrence of artefacts due to partial compensation. Results are presented which demonstrate the efficacy of the algorithm in reducing motion artefacts in conventional pulse-echo B-mode imaging. Misalignment side-lobes are reduced to levels comparable to those exhibited by longer continuous-phase modulated pulses while preserving

the desirable resolution characteristics and robustness to propagation effects of complementary binary-phase codes.

The motion-compensated complementary-coded imaging algorithm was subsequently adapted for use in synthetic aperture ultrasonic imaging, a relatively new modality in diagnostic imaging which has huge potential for real-time scanning of three-dimensional volumes, among other applications. A simulated synthetic transmit aperture imaging system was developed and simulation results are presented demonstrating the viability of motion-compensated complementary coding in this context.

1.3 Thesis Organisation

Chapter 2 begins with a short history of ultrasound in medicine and an introduction to the fundamentals of ultrasonic wave propagation in tissue. The transducer configurations typically encountered in diagnostic imaging are described, as are the characteristics of the ultrasonic fields they generate. The mechanics of image acquisition are described for both conventional sequential-scan imaging using focused pulses and aperture synthesis using unfocused pulses, and the chapter concludes with a review of a number of methods of ultrasonic velocity estimation.

Signal modulation and pulse compression are introduced in Chapter 3, which also contains a review of the literature on pulse compression in ultrasonic imaging and a discussion of some of the issues surrounding compression filtering in a highly attenuating inhomogeneous medium. Chapter 4 describes the results of simulated and experimental comparisons of a range of signal and filter-design methods for use in B-mode imaging. The methods used to design signals and filters with optimal side-lobe characteristics are described in detail.

Motion-compensation for complementary-coded B-mode imaging is introduced in Chapter 5, accompanied by simulation results that demonstrate its efficacy in reducing the side-lobes introduced by motion between simulations. The method is applied to synthetic aperture ultrasound in Chapter 6, which also includes results from synthetic aperture simulations. Some conclusions and suggestions for continuation of the work are outlined in Chapter 7.

Chapter 2
Medical Diagnostic Ultrasound

2.1 Introduction

This chapter presents an introduction to medical ultrasound systems, beginning with a short overview of the historical development of ultrasound in medicine in Section 2.2. Section 2.3 describes the propagation of ultrasonic waves in attenuating media, while Sections 2.4 and 2.5 describe the characteristics of single-element and array transducers, respectively. Some considerations impacting on ultrasonic image quality are discussed in Section 2.9 and the chapter concludes with a review of methods of ultrasonic velocity estimation and a short note on the Field II ultrasound simulation tool used to generate some of the results reported in later chapters. More comprehensive treatments of some of these areas may be found in [5, 6, 30].

2.2 Ultrasound in Medicine: History and Fundamentals

The first mathematical theory of sound wave propagation was published in Isaac Newton's *Principia Mathematica* in 1686, two millenia after Aristotle's assertion that sound was generated by a source "thrusting forward in like manner the adjoining air, to that the sound travels unaltered in quality as far as the disturbance of the air manages to reach [76]." Sound waves are mechanical vibrations that can propagate through all types of matter as *longitudinal* (or *compressional*) waves of alternating pressure deviations from the equilibrium pressure of the medium. In solids, sound may also propagate as a *transverse wave* consisting of oscillations perpendicular to the direction of propagation.

The term *ultrasound* is used to refer to sound waves with frequencies in excess of the 20KHz or so detectable by the human ear. Although the potential of ultrasound for underwater echo-ranging was demonstrated by Langevin in 1917, the earliest medical applications of the technology were therapeutic rather than diagnostic: the heating effects of ultrasound were widely employed throughout the 1930's and 1940's in attempts to inhibit tumour growth [71]. The technology was initially greeted with considerable enthusiasm, but it was concluded at the

1949 Ultrasound in Medicine conference in Erlangen, Germany that it was ineffective for cancer therapy and that its clinical use should be discontinued. Subsequent developments indicate that this resolution was premature: more recent trials using ultrasound in combination with radiation therapy have shown promise, and the commercial development of clinical focused ultrasound surgery devices has been underway since the 1990s [22].

Some of the earliest experiments in medical ultrasonic imaging were conducted by Karl Dussik in the late 1930s. Prompted by research in radar and ultrasonic detection of flaws in metal, Dussik used transducers placed on either side of the skull to measure differences in the amount of energy transmitted through it at different locations, recording the intensity of received signals using photographic paper. The procedure was christened *hyperphonography* and the images it produced were known as *ventriculograms*, as Dussik mistakenly thought they represented the ventricular structure of the brain. They were later shown to be artefacts due to the attenuation characteristics of the skull itself rather than its contents [97].

Modern diagnostic ultrasound is based on the analysis of reflected ultrasonic echoes rather than the through-transmission method employed by Dussik. Its development was facilitated by the availability of fast electronic circuitry resulting from radar and sonar research during the second world war. In its simplest form, ultrasonic *reflectometry* requires a transmitter, a receiver and their associated control and signal processing systems. Transmitter and receiver, usually piezoelectric devices, are coupled to the medium to be imaged. The transmitter *insonates* the medium by propagating a mechanical wavefront whose shape (the *ultrasonic field*) is determined by the characteristics of the transducer and those of the medium itself. The receiver has an associated *reception zone*, again determined by the characteristics of transducer and medium. The receiver is arranged so that its' reception zone has some degree of overlap with the transmitted field, as illustrated in Figure 2.1. This overlapping region defines the ultrasound *beam*. When the transmitter is driven with a signal at an ultrasonic frequency, the received signal will consist of reflections from within the volume contained by the beam and may be analysed to obtain information on the reflecting elements within that volume. Most medical ultrasound systems may be broadly categorised as either *pulsed-wave* (PW) or *continuous-wave* (CW) devices.

2.2.1 Pulsed-Wave (PW) Ultrasound

In a pulsed-wave or pulse-echo mode system, the transmitter is driven with an ultrasonic pulse of finite duration, T, propagating a pressure wave into the ultrasonic medium to which it is cou-

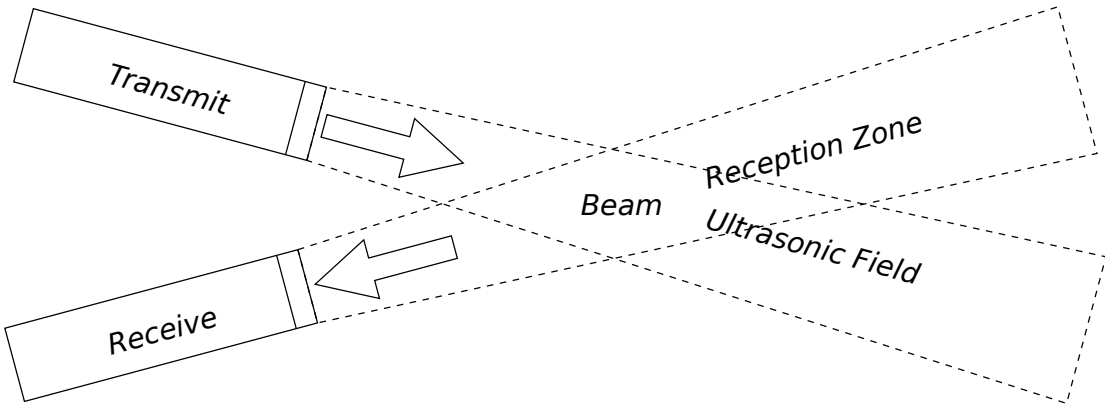

Figure 2.1: Transmission and reception zones and the ultrasonic "beam"

pled. Assuming transmitter and receiver are coincident, the reflected signal received between times t_1 and t_2 correspond to reflections from the volume bounded by the ultrasound beam between a distance of $\frac{c(t_1-T)}{2}$ and $\frac{ct_2}{2}$ metres from the transducer, where c is the velocity of ultrasound in tissue. On the basis of this observation the received data may be split into individual short segments known as *sample volumes*, each of which corresponds to a distinct region of the beam. These can then be processed individually to build up a one-dimensional image of the entire volume contained within the beam. This process may be repeated at different locations to build up a two- or three-dimensional image or at the same location to track time-varying features within the beam.

The basis for pulse-echo imaging in medicine is considered to be Firestone's patent for flaw detection in metal, filed in 1942. Applying similar techniques to medical diagnosis, Howry initially demonstrated the detection of tissue interfaces in ultrasonic echoes in the late 1940s [71]. The pace of development was rapid, and two-dimensional pulse-echo ultrasound scanners developed for medical use were demonstrated in the early 1950s by two independent research groups: one led by Wild in Minneapolis and another led by Howry in Denver, Colorado. Some images produced by Howry's apparatus have been reproduced in Figure 2.2. Ian Donald, a medical doctor and researcher in obstetrics and gynaecology, attended a talk given by Wild in England in 1954. Shortly afterwards, he took up a post as Regius Chair of Midwifery at Glasgow University where he pioneered development of compact scanning equipment and the use of ultrasound in medical diagnosis [96].

In a pulse-echo system, the same transducer may be used to transmit and receive as the two functions need not be performed concurrently. Besides the obvious cost benefits, this allows for

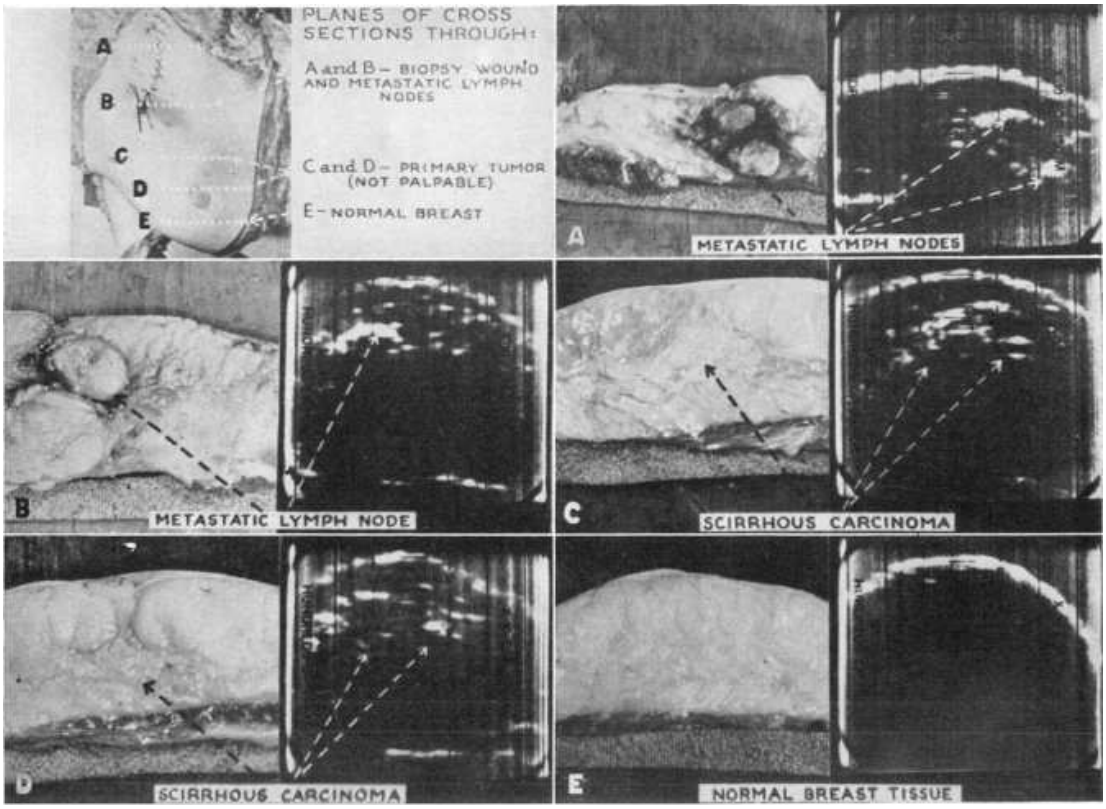

Figure 2.2: Early "Sonograms" produced by Howry et. al. [47]

coincident transmission and reception of the ultrasonic pulse. Most current ultrasonic imaging systems use high-density arrays of transducers and the use of a single device for transmission and reception also allows for a higher concentration of sensing units, which has a beneficial impact on the focusing characteristics of the system.

2.2.2 Continuous-Wave (CW) Ultrasound

The period spanning the 1950s and 1960s saw rapid development of equipment for measuring flow and motion using ultrasound. The first successful non-invasive system for ultrasonic blood-flow measurement was a dual transducer CW system developed by Satomura in the late 1950s [80]. One transducer was used to insonate an artery with a continuously transmitted ultrasonic signal, while the reflected signal received at the other transducer exhibited a Doppler frequency shift proportional to the velocity of flow in the artery (see Section 2.3).

CW systems transmit and receive continuously and require at least one dedicated transducer element for each of the two functions, though these may be housed in the same probe. Unlike PW ultrasound, this arrangement doesn't allow for the discrimination of reflections from elements at different positions within the beam except in the sense that reflections originating closer to the transducer are less attenuated than those originating further away. Nonetheless, some control may be exercised over the depth of the region to be interrogated by manipulating the relative positions of the transmit and receive elements to control the shape of the beam. Although the majority of current systems estimate motion based on the time-shifts between consecutive PW echoes, CW devices still offer some advantages in that they are highly sensitive, cheap to manufacture and not susceptible to aliasing [79], properties useful for measuring the high velocities encountered in valvular and congenital heart disease.

2.2.3 Representation of Ultrasound Data

A large number of echo display methods have been used in ultrasonic imaging applications over the years. Some of the more common and/or historically important of these are listed below [30]. Although potentially rich in informational content, the dimensionality of signals acquired using a CW system is lower than that of echoes acquired using PW equipment and these signals are generally represented as a stereo audio signal or used to generate a spectral Doppler image.

A-mode In Amplitude-mode, the intensity of the received signal envelope is represented by the height of a trace on an oscilloscope type display. Reflection from a boundary between anatomic regions with different propagation characteristics causes a spike in the oscilloscope trace.

B-mode / B-scan In B-mode or Brightness-mode, the instantaneous intensity of the received signal is converted to a series of grey-levels known as a *scan line* for display. Each scan line represents a one-dimensional image of the region encompassed by the beam. In B-mode or B-scan imaging, a series of scan lines is acquired by transmitting pulses in different directions and combined to form a single two- or three-dimensional image. The two terms are used interchangeably in the literature.

M-mode In M-mode or motion-mode, a succession of B-mode lines captured from the same transducer position are displayed side by side. This allows an experienced operator to track changes in the region of interest over time.

Spectral Doppler A spectral Doppler image presents a visual record of the variation of flow velocities over time, with Doppler frequency shift on the vertical axis and time on the horizontal. This method may be used to display PW or CW data.

Colour Flow Imaging (CFI) In CFI, colour velocity information is overlaid on a section of a B-mode image. While this imaging mode doesn't represent velocity information in as much detail as M-mode or Spectral Doppler, it provides a useful overview of motion within a two-dimensional section of the scan region and is often used in conjunction with one or other of them.

Many modern commercial devices combine multiple complementary imaging modes in a single display. A duplex image of cardiac motion may be seen in Figure 2.3: the upper half of the display contains a B-mode image and the lower half an M-mode display of the region under the green line. Figure 2.4 is a triplex image of what appears to be arterial flow: the upper half of the display contains a B-mode image with overlaid colour flow information and the lower half a Spectral Doppler representation of the region under the line running through its centre.

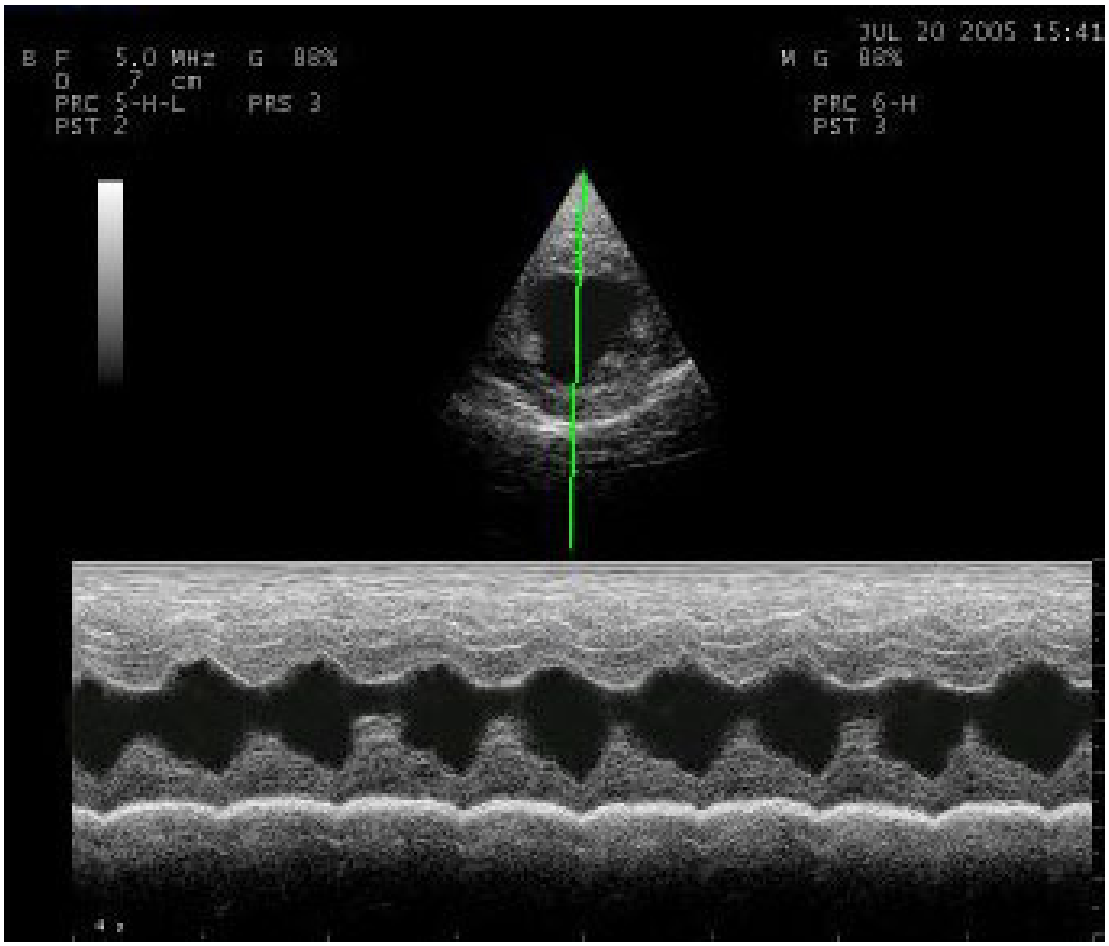

Figure 2.3: Duplex Imaging: B-mode above, M-mode below [from www.gehealthcare.com]

2.3 Ultrasonic Wave Propagation

The waves used in medical ultrasonography are longitudinal ultrasonic waves produced by the push-pull action of the transducer on the medium. Medical imaging techniques tend to employ frequencies in the 2 to 20 MHz range, corresponding to wavelengths of about 0.77 to 0.077 mm in soft tissue. A human subject represents a highly attenuating medium consisting of various layers of skin, blood, fat, muscle, bone etc, all of which have different physical characteristics which affect wave propagation.

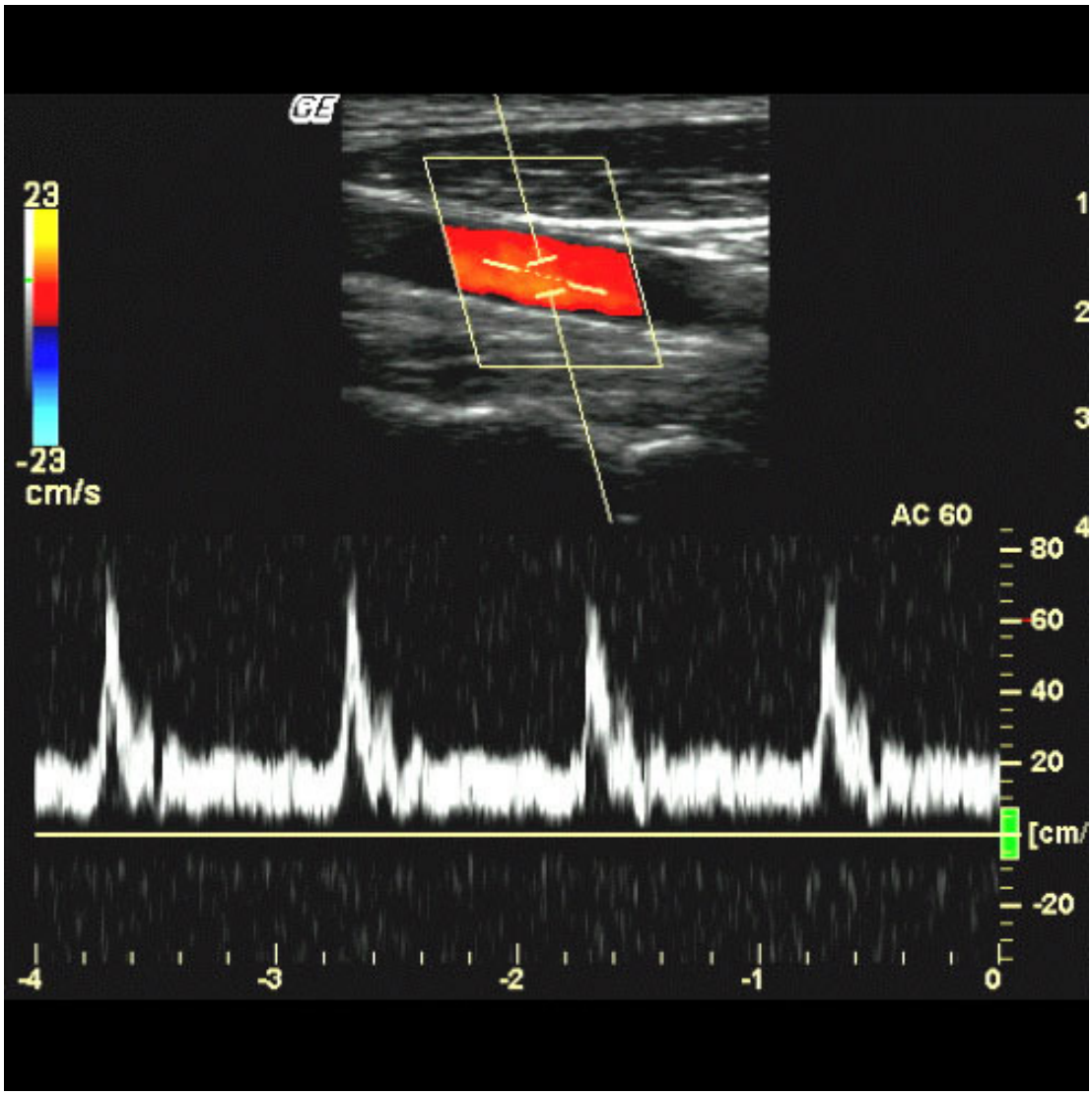

Figure 2.4: Triplex Imaging: B-mode with overlaid CFI above, Spectral Doppler below [from www.gehealthcare.com]

2.3.1 Variations in Speed of Sound and Acoustic Impedance

The value for c, the speed of sound, used to calculate propagation time for an ultrasonic signal in the body is generally taken to be about 1540 m/s, the *soft tissue average*. The speed of sound in any material varies in inverse proportion to its compressibility, so each of the layers encountered by a wavefront has an associated speed of sound. The *characteristic impedance* or *specific acoustic impedance* of a material, $Z = \rho c$, is the product of the density of the medium and its associated velocity of sound propagation.

Medium	Velocity	Acoustic Impedance
Air	343 m/s	0.0004 kg/m^{2}s
Water	1480 m/s	1.48 kg/m^{2}s
Blood	1550 m/s	1.62 kg/m^{2}s
Fat	1450 m/s	1.38 kg/m^{2}s
Myocardium	1550 m/s	1.62 kg/m^{2}s
Liver	1570 m/s	1.65 kg/m^{2}s
Bone	3360 m/s	6.00 kg/m^{2}s

Table 2.1: Sound velocities and acoustic impedances of various media [8]

Table 2.1 lists typical sound velocities and acoustic impedances for a number of different media. The variation in propagation velocity along the beam path can also lead to ranging difficulties, particularly when layers of fat (with c = 1450 m/s) are to be found in the beam path. More importantly, the differences in sound velocity and acoustic impedance at either side of a boundary between materials give rise to the twin phenomena of reflection and refraction.

2.3.2 Scattering, Reflection and Refraction

Reflection and scattering refer to the same phenomenon, namely the redistribution of incident energy into other angular directions. Scattering occurs when a pressure wave strikes a discontinuity of dimensions similar to or less than a wavelength and the wave energy is scattered in all directions. Reflection occurs when a pressure wave strikes a discontinuity of dimensions significantly larger than the wavelength and is directional. In diagnostic ultrasound, received signals consist primarily of superimposed echoes from multiple sub-wavelength scatterers. In B-mode imaging, interference between reflections from randomly distributed sub-wavelength scatterers causes the emergence of a noise-like pattern known as *speckle*, which degrades the spatial and contrast resolution of images. The term *fully developed speckle* is used to describe the situation in which there are sufficient randomly distributed sub-wavelength scatterers in an

image resolution cell to ensure a true speckle pattern develops.

When a pressure wave reaches a boundary between media m_a and m_b, a proportion of the incident energy is reflected back into m_a while the remainder of the signal energy is transmitted into m_b. The angle of reflection is equal to that of the incident wave. The angle of the refracted wave propagated into m_b is a function of the ratio of the velocities of sound in the two media:

$$\theta_r = \sin^{-1}\left(\frac{c_b \sin(\theta_a)}{c_a}\right) \tag{2.1}$$

where θ_a is the angle between the direction of propagation in $m_a$and the layer boundary and c_a and c_b are the velocities of sound in the respective media. If the boundary is at a right angle to the beam, refraction will cause the beam to diverge or converge depending on the ratio of velocities of sound in the two media. Otherwise, refraction will result in a combination of beam divergence/convergence and a change in beam direction.

The values of c for tissue, blood and other fluids are reasonably tightly clustered around the 1540 m/s mark and the effects of reflection and refraction are relatively minor at boundaries between them. Bone, on the other hand, should generally be avoided due to its high acoustic velocity and impedance. Reflection and beam divergence at a bone/tissue boundary are very high, significantly reducing signal penetration.

2.3.3 Non-Linear Propagation

Another effect of the relationship between compressibility and propagation speed is *non-linear propagation*. The portions of tissue influenced by the positive half-cycles of pressure will be slightly compressed and therefore less compressible, leading to a higher velocity of propagation. The opposite is true of those portions of tissue affected by the negative half-cycle of the wave. This causes the positive half cycles to catch up on the negative half-cycles, distorting the waveform. The distortion becomes more profound with depth. Eventually the peak of the positive half-cycle overlaps with the trough of the negative half-cycle causing destructive interference and forming a shock wave. This effect is highly frequency-dependent: the wavelength is shorter at higher frequencies, as is the initial distance between peak and trough, and shock wave formation will occur more rapidly than for a lower frequency signal of the same peak amplitude. Shock wave formation can introduce higher harmonics into the pulse spectrum, a phenomenon which may exploited to achieve greater depth and focus of imaging.

2.3.4 Absorption

As a pressure wave propagates through the body, a proportion of its energy is converted into heat by the process of absorption. The largest contribution to absorption of ultrasound energy in the body is that due to relaxation mechanisms [30]. As a pressure wave propagates through a homogeneous medium, its constituent particles are pushed into new positions and then released. A finite period of time elapses before a given particle returns to its neutral positions. If this relaxation time is comparable to the wave period, the particle may not have returned to its neutral position before the next pressure peak arrives, i.e. the particle is moving in the opposite direction to the wave and energy is expended reversing the direction of particle motion [8].

2.3.5 Attenuation

The total attenuation of the wave is due to the effects of absorption combined with those of the mechanisms of scattering, reflection, refraction and non-linear propagation described above. Attenuation rises rapidly over the range of frequencies used for ultrasonic signals due to the high level of frequency-dependence of most of its contributing factors. The net result is a depth-dependent distortion of reflected signals caused by a reduction in signal bandwidth and spectral centroid.

2.3.6 Motion Effects

Reflections from moving scatterers in the beam path also affect the spectrum of the received RF signal. This is due to a phenomenon known as the *Doppler Effect*, which causes reflections from moving scatterers to be shifted in frequency by an amount $f_d = \frac{2f_c v \cos\theta_d}{c}$ relative to the transmitted pulse, where f_c is the transmitted pulse centre frequency, v is the velocity of the moving scatterers, θ_d is the angle between the beam and direction of motion and c is the velocity of ultrasound in the medium. The $\cos\theta_d$ term indicates that this shift in frequency is proportional to the velocity component parallel to the beam. If θ_d is known, the velocity of the moving scatterers may be estimated from a measurement of f_d.

The velocity component perpendicular to the beam affects the bandwidth of the reflections. This phenomenon is known as *intrinsic spectral broadening* as it is due to characteristics of the measurement system itself. The finite width of the transducer and beam mean that the effective Doppler angle, θ_d, changes as the scatterers traverse the beam so that the reflected energy is

spread out across a range of velocities proportional to their transverse velocity.

2.4 Characteristics of Ultrasonic Fields

2.4.1 Pressure Amplitude, Power and Sound Intensity

At any point in a sound field, spatial coordinates $\vec{p} = \{x_p, y_p, z_p\}$, the pressure deviation from the equilibrium pressure of the field may be represented by a time-varying function $s_p(t)$. The *instantaneous power* of such a function is

$$P(t) = |s_p(t)|^2 \tag{2.2}$$

The *energy* of such a signal in joules (J) is

$$E_{\mathrm{A}} = \int_{-\infty}^{\infty} P(t)dt = \int_{-\infty}^{\infty} |s_p(t)|^2 dt \tag{2.3}$$

The *average signal power*, measured in watts (W), is defined as its energy per unit time and may be written

$$P = \lim_{T\to\infty} \frac{1}{T} \int_{-\frac{T}{2}}^{\frac{T}{2}} P(t)dt = \lim_{T\to\infty} \frac{1}{T} \int_{-\frac{T}{2}}^{\frac{T}{2}} (|s_p(t)|)^2 dt \tag{2.4}$$

For a periodic signal with period T, (2.4) may be simplified to

$$P = \frac{1}{T} \int_{-\frac{T}{2}}^{\frac{T}{2}} P(t)dt = \frac{1}{T} \int_{-\frac{T}{2}}^{\frac{T}{2}} (|s_p(t)|)^2 dt \tag{2.5}$$

The expression in (2.5) also describes the average power of a signal of finite duration, T, over the duration of the signal.

Sound *intensity*, measured in watts-per-square-metre (W/m^2), is defined as the power per unit area. The *instantaneous intensity* [2] at a point in the field is

$$I(t) = \frac{s_p(t)^2}{Z} \tag{2.6}$$

where Z represents the characteristic impedance of the medium, described in Section 2.3. The *average intensity* is then

$$I_{\mathrm{A}} = \frac{1}{T}\int_0^T I(t)dt = \frac{1}{T}\int_0^T \frac{s_p(t)^2}{Z}dt \tag{2.7}$$

The *Sound Intensity Level (SIL)*, I_{dB}, is usually expressed on a logarithmic scale based on the ratio of the average intensity to a reference intensity, I_0, of 1 picowatt per square metre ($10^{-12}\mathrm{W/m}^2$) [3].

$$I_{\mathrm{dB}} = 10\log_{10}\frac{I_{\mathrm{A}}}{I_0} \tag{2.8}$$

2.4.2 The Huygens Principle

The acoustic field generated by an ultrasonic transducer is a function of the element geometry, the pulse spectrum and the characteristics of the medium. It may be estimated using the *Huygens principle*, which states that any single source may be considered to consist of a series of sources, small with respect to wavelength, all of which radiate uniformly in all directions. The field generated by any source of finite aperture at any point in space and time may then be determined by considering the instantaneous amplitude and phase of the waves propagated from each of the incremental sources. These incremental sources are known as *Huygens sources* or *spherical point sources* and produce spherical pressure waves. The energy of a spherical wavefront is distributed over a surface of area $4\pi r^2$. In a lossless medium this energy is conserved as the wavefront propagates, i.e. the average field intensity decreases in proportion to the square of the radial distance from its centre.

2.4.3 Unfocused Sources

An axial section of the idealised acoustic field from a plane circular 'piston' source is shown in Figure 2.5. The source is assumed to be vibrating sinusoidally with frequency f_c in the direction perpendicular to its surface, meaning all of the Huygens sources are emitting spherical waves of identical amplitude and phase. The resulting field is symmetric about the central axis of the transducer due to the radial symmetry of the source. The field is conventionally divided into two regions based on the changing nature of wave propagation with distance from the transducer.

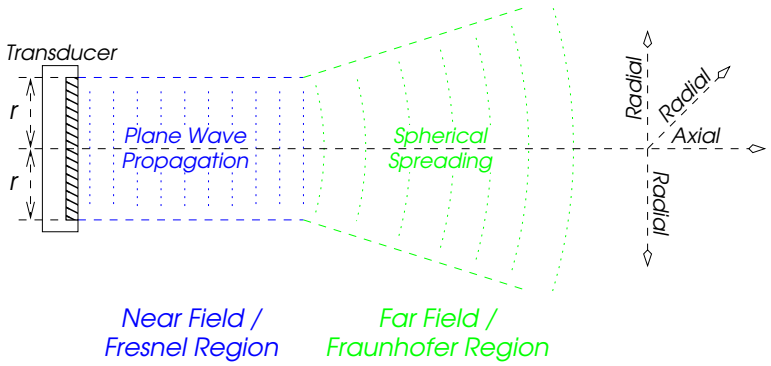

Figure 2.5: Axial section of the idealised acoustic field from a plane circular transducer

The *near field* is the region close to the surface of the transducer in which the effects of constructive and destructive interference between the spherical wave fronts emanating from the individual Huygens sources cause large fluctuations in field intensity along the transducer axis. This is accompanied by off-axis amplitude modulation, i.e. in the direction parallel to the surface of the transducer. This region is sometimes referred to as the *Fresnel zone*. Propagation of the combined wavefront in this region is conventionally approximated as planar. The *far field* or *Fraunhofer zone* is the region in which the difference between any two points on the transducer surface is negligible in comparison to their distance from a given field point. Individual pressure waves exhibit less curvature due to spherical expansion and combine constructively to form an approximately spherical wavefront originating at the centre of the transducer surface. The field intensity is at a maximum along an axis perpendicular to the centre of the element's surface and declines relatively smoothly with increasing axial distance from the transducer and radial distance from the central transducer axis.

The *Rayleigh distance* [6], z_R is the approximate point at which the transition between the near and far field occurs:

$$z_R = \frac{\pi r_a^2}{\lambda} \tag{2.9}$$

where r_a is the radius of the transducer, $\lambda = \frac{c}{f_c}$ is the wavelength and c is the velocity of sound in the medium. It is clear from (2.9) that the length of the near field increases in proportion to the square of the transducer radius. Expressing the transducer radius as a multiple of the wavelength, $r_a = m\lambda$, (2.9) becomes

$$z_R = \pi m^2 \lambda \tag{2.10}$$

i.e. for a fixed ratio of transducer radius to wavelength, m_k, the length of the near field increases linearly in inverse proportion to the pulse centre frequency.

In the far field, the beam diverges at an angle ϕ_b:

$$\phi_b = \sin^{-1} \frac{0.511\lambda}{r_a} = \sin^{-1} \frac{0.511}{m} \tag{2.11}$$

Interpreting (2.10) and (2.11), the length of the near field increases with m, the ratio of the aperture radius to pulse wavelength, while the angle of beam divergence decreases.

The beam illustrated in Figure 2.5 is the main-lobe radiation pattern of the transducer. The full field generated by a transducer of this type consists of a main lobe and several side-lobes, the number and magnitude of which depend on the size and shape of the aperture. For a circular disc transducer, the first side-lobe occurs 17dB below the main-lobe. Spatial side-lobe levels may be reduced by driving the central portion of the aperture at a higher amplitude than the regions toward the edge, a process known as *apodisation*. For a single-element transducer, this may be accomplished using mechanical methods.

2.4.4 Focused Sources

A geometrically focused acoustic field may be generated using a curved transducer or by using an acoustic lens (or mirror) in conjunction with an unfocused source.

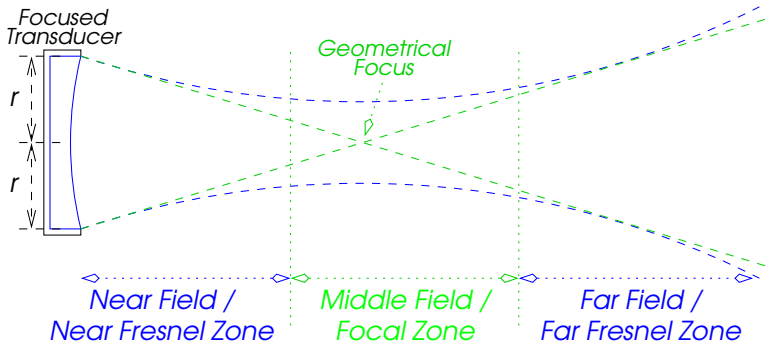

Figure 2.6: Axial section of the acoustic field from a focused circular transducer

The amplitude gain associated with geometric focusing from a source with radius of curvature or Geometrical focal point z_f is:

$$G_f = \frac{z_R}{z_f} = \frac{\pi r_a^2}{\lambda z_f} \tag{2.12}$$

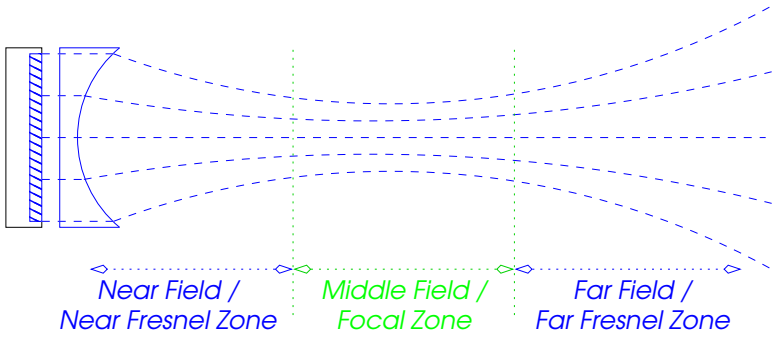

Figure 2.7: Focusing with an acoustic lens

An unfocused transducer is sometimes said to have a *natural focus* at $z_f = z_R$, i.e. the Rayleigh distance. Using this in (2.12), the amplitude gain at the natural focus of an unfocused transducer is $G_f = \frac{z_R}{z_R} = 1$, as one would expect.

2.4.5 Resolution

The axial and lateral resolutions of an aperture are determined by the duration of the emitted pulse (convolved with the impulse response of the aperture) and the beam-width of the transducer [7]. At the focal point of an aperture, the beam-width, w_f is:

$$w_f \cong F_f \lambda \tag{2.13}$$

where $F_f = \frac{z_f}{2r_a}$ is the *f-number* of the aperture, defined as the ratio of focal distance to aperture width. The *depth of focus*, D_f, is the axial length of the region in which the intensity of the beam is within 1.5dB of the maximum at the focus and is defined as:

$$D_f \cong F_f^2 \lambda \tag{2.14}$$

Using (2.10), the f-number for an unfocused transducer may be rewritten as:

$$F_f = \frac{m^2 \lambda}{2m\lambda} = m/2 \tag{2.15}$$

Combining (2.13) and (2.14) with (2.15)

$$w_f \cong \frac{m\lambda}{2} \tag{2.16}$$

$$D_f \cong \frac{m^2\lambda}{2} \tag{2.17}$$

i.e. for a fixed ratio of aperture-width to wavelength, the beam-width and depth of focus decrease linearly with increasing frequency.

2.5 Imaging with Array Transducers

The two- or three-dimensional data sets required for B-mode imaging are usually acquired on a line by line basis by transmitting and receiving pulses in a number of different directions. This may be accomplished either by physically moving the transducer between pulse emissions or, as is more often the case in practice, by using different elements or combinations of elements of a multi-element transducer array. The elements of a transducer array are usually identical. The distance between adjacent element centres is referred to as the element *pitch*, while the distance between individual elements is referred to as the element *kerf width*, as illustrated in Figure 2.8 for a one-dimensional array transducer. Some of the array configurations most commonly

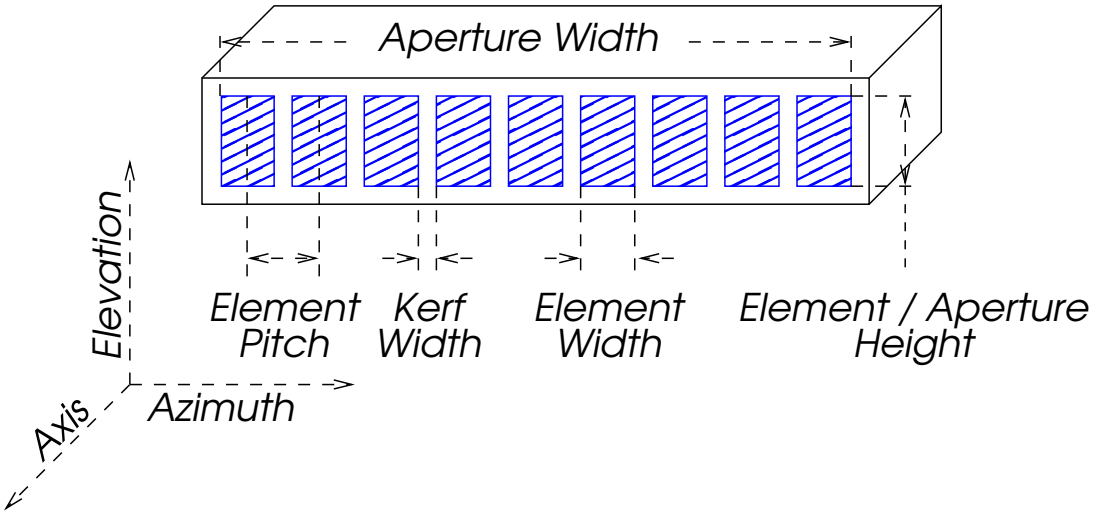

Figure 2.8: Geometry of a one-dimensional transducer array

encountered in diagnostic imaging are described in Section 2.5.1. The characteristics of the fields generated by array transducers and non-circular elements are described in Section 2.5.2, while multi-element beam-formation is described in Section 2.5.3.

2.5.1 Array Configurations

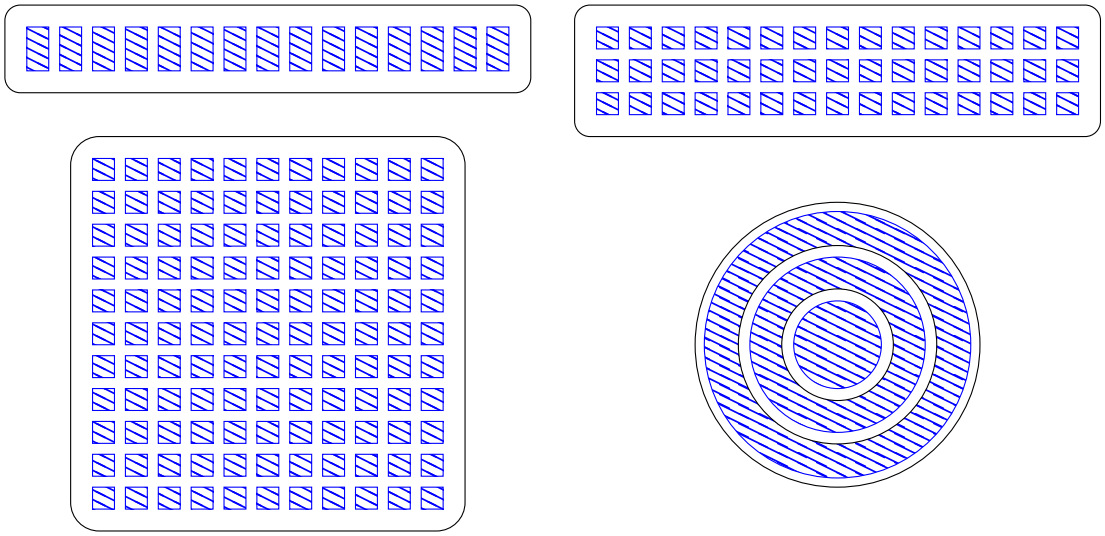

Figure 2.9: 1-D, 1.5-D, annular and 2-D transducer arrays (clockwise from top-left)

A wide range of array configurations are used in diagnostic ultrasound. Some of the most common are:

1-D arrays The most common array configuration. These consist of a row of equally spaced elements arranged laterally, providing control over azimuthal focus of the aperture. Individual elements are usually unfocused in the azimuthal plane though an acoustic lens may be used to focus the beam in the elevation plane.

2-D arrays These are typically used for 3-D imaging. The elements are usually square, unfocused and arranged in a regular grid pattern.

"1.5-D" arrays A 2-D array of elements in which the number of elements in the lateral dimension significantly exceeds that in the vertical. These are typically used for 2-D imaging. The small number of elements in the vertical plane allow limited elevational focusing. This arrangement offers increased resolution in the elevation plane in the near and mid-field regions, but the aperture is not sufficiently large to improve far-field elevational resolution significantly.

Annular arrays In its simplest form, an annular array consists of a number of concentric ring elements, allowing variable beam focusing along the transducer access. In a more complex annular array, the ring elements may be sub-divided to allow beam-steering in addition to focusing.

2.5.2 Beam Characteristics of Array Transducers

Individual elements of a transducer array are usually square or rectangular i.e. they do not exhibit the radial symmetry of the ideal sources described in Section 2.4. Taking a simplified view of beam formation, the length of the near field is controlled separately by the two orthogonal dimensions of the source. Allowing x_a and y_a to represent the element dimensions in the azimuth and elevation directions, if $x_a = y_a$, individual elements will behave somewhat like circular sources of radius $\frac{x_a}{2}$, exhibiting a field maximum at $z \cong \frac{\pi x_a^2}{4\lambda}$, although the near field amplitude modulation will not be as pronounced [6]. If $x_a \neq y_a$, then there will be a shorter region exhibiting amplitude-modulation section in one direction than the other and the beam will exhibit increased divergence.

In array imaging, multiple elements are used simultaneously to provide a larger effective aperture. An aperture made up of a number of discrete array elements exhibits similar beam characteristics to a single source of similar dimensions. The array transducer could be viewed as a coarse physical analogue of the Huygens principle. The spatial periodicity of elements introduces potential complications with grating lobes, which are described in detail in [7]. These are essentially secondary beams occurring at an angle θ_g to either side of the main beam:

$$\theta_g = \sin^{-1}(\frac{n\lambda}{x_p}) \tag{2.18}$$

where x_p is the element pitch. Reducing the ratio of element pitch to wavelength increases the grating lobe angle at the expense of a reduction in sensitivity due to the reduced surface area of the transducer. An increase in θ_g reduces the magnitude of grating lobe artefacts as the sensitivity of individual array elements varies with angle of incidence. Reducing the element pitch to $\frac{\lambda}{2}$ eliminates grating lobes by increasing θ_g to 90°, effectively moving them behind or in line with the surface of the transducer.

2.5.3 Electronic Focusing, Beam-Steering and Apodisation

Using an array transducer, the effects of an acoustic lens or geometrical focusing may be simulated by manipulating the relative delays of the signals used to drive different elements of the array to electronically focus the transmission zone. This process is illustrated in Figure 2.10 (a) for a 1-dimensional transducer array. Similarly, signals received at adjacent elements may be time-shifted and added together to artificially focus the reception zone. *Beam-steering* is an

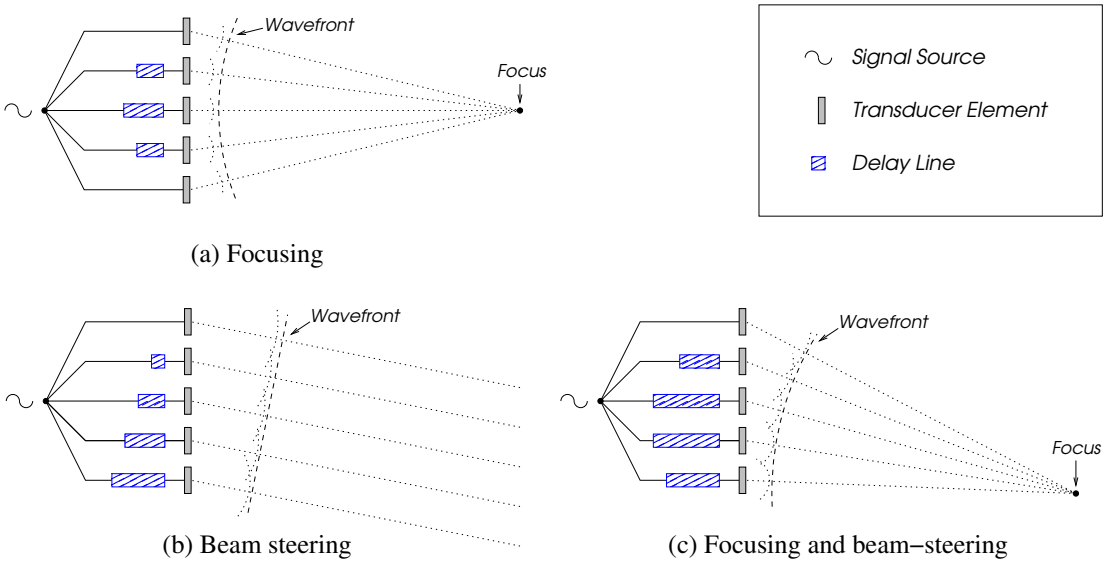

(a) Focusing

(b) Beam steering

(c) Focusing and beam−steering

Figure 2.10: Focusing and beam steering using a 1-D transducer array

extension of this method used to acquire data along a line other than that perpendicular to the face of the transducer, as illustrated in Figure 2.10 (b). Beam-steering can increase the strength of grating lobes, as a result of the angular dependence of element sensitivity: the strength of the main beam is reduced as it is steered away from the axis perpendicular to the face of the transducer, while the strengths of any grating lobes steered closer to the transducer axis are increased.

Using an electronically focused 1-dimensional array transducer with an aperture width of $a_x = m_x\lambda$, the f-number at a focal point z_f is $F_f = \frac{z_f}{a_x}$. Using this in (2.13) the lateral beam width is approximately:

$$w_f \cong \frac{z_f\lambda}{a_x} = \frac{z_f}{m_x} \tag{2.19}$$

i.e. the beam width increases with increasing focal depth but decreases with increasing aperture width. A wide aperture provides excellent lateral resolution at depth at the expense of an increase in the length of the near-field. Electronic apodisation is often adopted to reduce the impact of this trade-off. The width of the aperture may be controlled by varying the number of elements used in transmit and receive with imaging depth in order to maintain a relatively constant f-number. An amplitude apodisation weighting may also be applied to the aperture elements, reducing the amplitude of transmitted and received signals in proportion to the distance of the transmitting/receiving element from the centre of the transducer. As with focusing and beam-steering, variation of the aperture width and apodisation weightings on transmit requires

multiple pulse emissions but *dynamic apodisation* may be applied to received signals.

The process of manipulating the delays and apodisation weightings applied to transmitted and received signals in order to focus and steer the beam is known as *delay-sum beam-forming*. The signals emitted from the individual elements of an electronically focused and apodised N-element transducer array may be written:

$$g_n(\vec{f},t) = a_n[\vec{f}]g(t-\tau_n[\vec{f}]) \tag{2.20}$$

where $g(t)$ represents the excitation pulse, n represents an element index and $a_n[\vec{f}]$ and $\tau_n[\vec{f}]$ represent the apodisation weighting and the combined focusing and beam-steering delay, respectively, for a given element, n, and focal point, $\vec{f}$. Similarly, the beam-formed received signal $r(\vec{f},t)$ may be written in terms of the individual signals received at each element, $r_n(t)$, as:

$$r(\vec{f},t) = \sum_n a_n[\vec{f}]r_n(t-\tau_n[\vec{f}]) \tag{2.21}$$

Although the use of multiple focal regions on transmit requires multiple emissions, the focal delays used on receive may be varied as a function of depth, a process known as *dynamic focusing*. Using dynamic focusing (2.21) becomes:

$$r(\vec{l},t) = \sum_n a_n(\vec{l},t)r_n(t-\tau_n(\vec{l},t)) \tag{2.22}$$

where $\vec{l}$ is a vector representing the direction of the scan line. Unlike (2.21), the dynamic focusing described by (2.22) is not a time-invariant process.

In [72], the gain of an electronically focused array is given as

$$G_f = \begin{cases} \frac{1}{(\lambda F_f)^2} & z_f \leq z_A \\ \frac{1}{(\lambda F_f)^2}\frac{z_A^2}{z_f^2} & z_f > z_A \end{cases} \tag{2.23}$$

where z_A is the point at which the aperture is fully open, i.e. beyond this point the f-number declines linearly with distance. This expression assumes a rectangular apodisation window.

2.5.4 Signal-to-Noise Ratio

In signal processing, noise is sometimes defined as any unwanted signal. In ultrasonic imaging, this includes radio-frequency interference as well as random noise associated with the transducer and receiving circuitry. The signal-to-noise ratio (SNR) relates the average power of received signals to the total average power of all noise sources present within the system. In a medical ultrasonic imaging system, SNR is a function of the total noise power level, the peak and average transmitted power levels, and the focusing and apodisation settings of the system.

In a well-designed system, the principal source of random noise should be the transducer and its associated circuitry. A number of types of noise may be generated within a transducer, including thermal or Johnson noise, shot noise and flicker or $\frac{1}{f}$ noise [70].

Shot noise is a form of quantisation noise associated with the finite charge of individual electrons. It occurs in proportion to steady-state current and can therefore be disregarded as there is no steady-state current in the piezoelectric transducers typically used in medical ultrasonic imaging.

Flicker noise power varies in inverse proportion to frequency. Its origin is not well understood, however experiments have shown that it is not significant for ultrasound transducers operating in the MHz frequency range and can also be disregarded in this context.

Thermal or Johnson noise is due to thermal agitation of electrons in any conductor. It occurs independently of applied voltage and varies in proportion to the ambient temperature. Johnson noise may be represented as voltage source in series with an impedance. For an ultrasonic transducer, the open-circuit voltage [70] may be expressed as

$$V_{\text{noise}} = \sqrt{4k_{\text{B}}T_{\text{K}}RB} \tag{2.24}$$

where T_{K} is the temperature in degrees Kelvin, R is the real part of the transducer impedance, B is the system bandwidth in Hz and k_{B} is Boltzmann's constant, which relates the energy generated by random thermal motion at the molecular level to temperature.

The thermal noise power is

$$P_{\text{noise}} = \frac{V_{\text{noise}}^2}{R} = 4k_{\text{B}}T_{\text{K}}B \tag{2.25}$$

In medical ultrasound, transmitted power levels must be kept within limits set by various regulatory bodies. The International Electrotechnical Commission (IEC) has published safety recommendations for diagnostic ultrasound equipment [49], although approaches to regulation vary from one country to another [27]. In the US, recommendations made by the American Institute of Ultrasound in Medicine (AIUM) have been incorporated in the regulations of the Food and Drug Administration (FDA) [25, 31], while the Medical Devices Directive [28] contains safety guidelines for devices sold within the EU and requires manufacturers to provide relevant information to purchasers and diagnosticians. In the majority of cases, regulatory limits are defined in terms of incident flux rather than incident power. The *Thermal Index* (TI) is related to I_{spta}, the *spatial peak, temporal average* incident flux, and is an estimate of the local temperature increase due to tissue absorption of ultrasound. The *Mechanical Index* (MI) is:

$$\text{MI} = \frac{I_{\text{sptp}}}{f_c^2} \tag{2.26}$$

where I_{sptp} is the *spatial peak, temporal peak* incident flux, and f_c is the pulse centre frequency. The mechanical index is a measure of the danger of physical effects caused by high pressure levels, e.g. *cavitation*, the formation of gas bubbles at high negative pressure.

Commercial systems typically operate at, or close to, peak power limits but well below average power limits. Increasing average power while maintaining peak power requires the duration of the transmitted pulse to be increased, which tends to reduce axial resolution and introduce other issues discussed in Chapters 3 and 4. In [72], the following expression is derived for the maximum SNR obtainable for a given bandwidth, B, and peak flux limit, I_{pk}:

$$\text{SNR}_{\text{inh}} = \left(\frac{\pi c}{2B}\right) \eta I_{\text{pk}} / P_{\text{noise}} / G_f \tag{2.27}$$

where the term in brackets represents the length of an axial resolution cell, η represents a backscattering coefficient for the group of scatterers contained in a resolution cell, normalised to a unit volume, and P_{noise} and G_f represent the thermal noise power and focal gain of the aperture, as defined in equations (2.25) and (2.23), respectively.

A more detailed treatment of this topic may be found in [70], in which expressions are derived for the SNR of a multi-element transducer based on a parametrised model and taking the effects of the receiver amplifier into account as well as thermal noise generated in the transducer.

2.5.5 2-D Imaging

The most common array configurations used in two-dimensional imaging are one-dimensional *linear array transducers* and *phased array transducers*. A linear array transducer may be used to perform a *linear scan* of an approximately rectangular region perpendicular to the transducer surface. Using this approach, individual scan-lines are parallel to one another and acquired using identical focal settings applied to a different group of array elements, as illustrated in Figure 2.11.

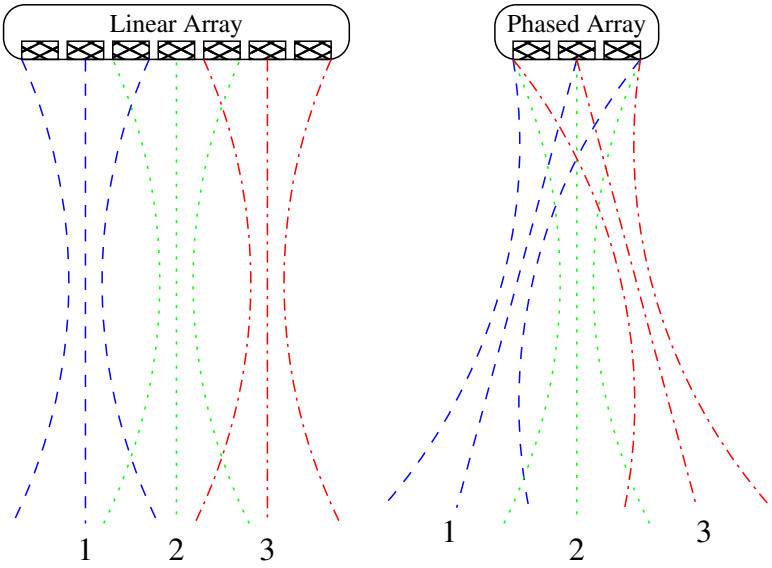

Figure 2.11: Successive scan line acquisitions for linear (L) and sector (R) scan imaging

Phased array transducers are used to perform a *sector scan* by sweeping the beam radially through a wedge shaped region: successive scan lines are acquired using the same group of elements but using a different set of focusing delays to steer the beam in another direction. Beam-formed data must undergo *scan conversion* in order to avoid geometrical distortion in the displayed image. Sector scanning allows a relatively large area to be imaged through a small acoustic window, particularly useful in applications like cardiac imaging, for example, where ultrasound must be propagated through the narrow gap in the centre of the ribcage.

Both linear and phased array transducers may be constructed along similar lines. A phased array transducer might be expected to have a lower element count to keep size down and a finer element pitch due to the increased danger of grating lobe artefacts introduced by beam-steering.

2.6 Simulation of Ultrasonic Fields

The simulations reported throughout this thesis were carried out using the *Field II* simulation program [32, 33], which runs under MATLAB® and uses a spatial impulse response method based on the work of Tupholme [88] and Stepanishen [84, 85]. Large apertures are modelled as collections of small square or triangular sub-elements allowing a wide-range of transducer geometries to be simulated. The contributions of individual sub-elements may be weighted to simulate different apodisation settings. The small size of the individual elements reduces computational complexity by allowing a far-field approximation to be used for beam calculations as described in Chapter 2.

Tissue is modelled as a collection of point scatterers. A two-way spatial impulse response is calculated for each scatterer and convolved with a depth-dependent filter to simulate the effects of attenuation. The received signal is obtained by convolving the linear sum of these individual contributions with the transmitted signal and the electromechanical impulse responses of the transmit and receive apertures, which are passed as parameters to the simulator.

Field II has a number of limitations: based on linear systems theory, it doesn't include a model of non-linear propagation and the spatial accuracy of simulated scatterer placement is a function of the simulator sampling frequency. The scattering model employed is based on the Born approximation, i.e. the intensity of the scattered field is assumed to be very low in comparison to the incident field and secondary scattering is ignored.

Over the course of this thesis research, an issue affecting the simulation of wide-band discrete-phase coded signals (introduced in Chapter 3) with Field II was identified. This introduced side-lobes at levels that were found to vary in proportion to the simulator sampling frequency and to the ratio of the length of the simulated transducer response to the distance between discrete phase transitions. This was identified as an aliasing issue and successfully addressed by filtering discrete-phase coded signals with a filter matched to the transducer pass-band prior to simulated propagation.

2.7 Synthetic Aperture Ultrasound

Synthetic aperture techniques have a long history in radar. The basic principle is that multiple spatially divergent pulse-echo measurements made using a single antenna mounted on a moving

platform may be synthesised to provide azimuthal resolution equivalent to that of a large array of fixed antennae, provided the motion of the platform may be measured accurately and any motion of the imaging target is low in relation to the synthesis period over which the individual measurements were made. This allows detailed images of terrain to be formed using a single antenna mounted on a plane, for example.

In medical ultrasonic imaging using array transducers, pulse-echo measurements made using different combinations of transmitting and receiving elements may be combined to *synthesise* an aperture. In this context, a number of variations of synthetic aperture ultrasound (SAU) imaging are possible:

Synthetic Transmit Aperture (STA): A single element or subset of elements is used in transmit and all elements used in receive.

Synthetic Receive Aperture (SRA): All elements are used in transmit and a single element or subset of elements used in receive.

Synthetic Transmit and Receive Aperture (STRA): A single element or subset of elements is used in both transmit and receive. Synthetic aperture radar could be described as a synthetic transmit and receive aperture imaging system.

A detailed discussion of the merits and demerits of the different variations on aperture synthesis may be found in [69]. In brief, the only advantage of synthetic receive aperture imaging over conventional B-mode imaging is that it can reduce manufacturing costs by allowing a large receive aperture to be synthesised using a limited number of receive channels, with a proportional increase in acquisition time. Synthetic transmit aperture imaging, on the other hand, allows dynamic focusing and apodisation to be used on transmit as well as receive and potentially allows large volumes to be scanned using a small number of acquisitions, making it particularly attractive for 3D imaging. Dynamic transmit focusing is particularly attractive at high frequencies as the depth of focus decreases with increasing frequency. These advantages come at the expense of significant increases in data storage and computational requirements and potential ghosting artefacts introduced by motion between acquisitions.

The majority of current commercial scanners acquire B-mode images on a line-by-line basis using focused pulses. This approach is efficient for two-dimensional scanning in the sense that memory requirements are low and comparatively little post-processing of received signals

is required prior to display. The method is inefficient in its use of received data, however. The small elements constituting an array transducer transmit energy in all directions and the received signals used to form individual scan lines contain reflections from elements outside the scan-line boundaries, the amplitudes of which are minimised by the effects of transmit and receive focusing and apodisation. A substantial portion of the information received during each acquisition interval is discarded using this *sequential scan* approach to ultrasonic imaging.

In STA imaging, received signals are recorded using all of the array elements while a unfocused pulses are emitted using each element of the transducer array in turn, as illustrated in Figure 2.12 (a). Once a full set of reflection data has been acquired, the transmit aperture may be synthesised: each scan line is formed by combining data acquired using each of the transmitting elements. As single elements are used in transmit, dynamic transmit focusing and apodisation may be applied during the aperture synthesis phase by scaling and delaying the data recorded during discrete acquisition intervals.

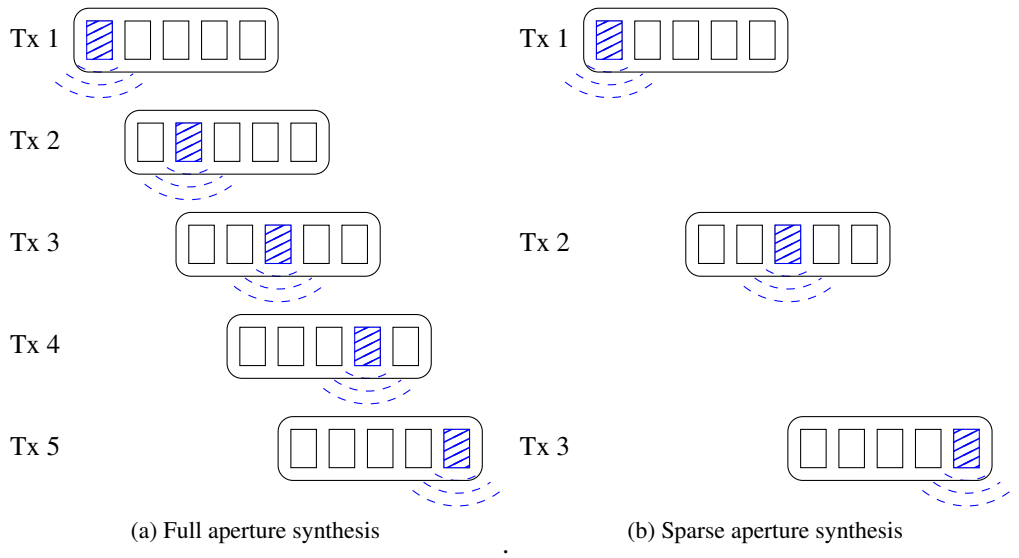

(a) Full aperture synthesis (b) Sparse aperture synthesis

Figure 2.12: STA acquisition sequences for full and sparse aperture synthesis

The STA acquisition time may be reduced significantly by using a *sparse synthetic transmit aperture*, i.e. acquiring data using only some of the array elements on transmit as illustrated in Figure 2.12 (b). This will not affect the resolution of the system provided the two outermost array elements are both used, as the beam-width and depth-of-focus are controlled by the pulse wavelength and the overall width of the aperture (see Equations (2.13) and (2.14)). The grating lobe angle is related to the element pitch, however, and the use of a sparse aperture is likely

result in grating lobe angles of less than 90°. The amplitude of these may be reduced by varying the distances between adjacent transmitting elements, thus ensuring inter-element spacing is not periodic. The effective surface area of a sparse synthetic aperture is also reduced, resulting in a decrease in focusing gain. This effect may be counteracted using *virtual sources* consisting of a number of elements.

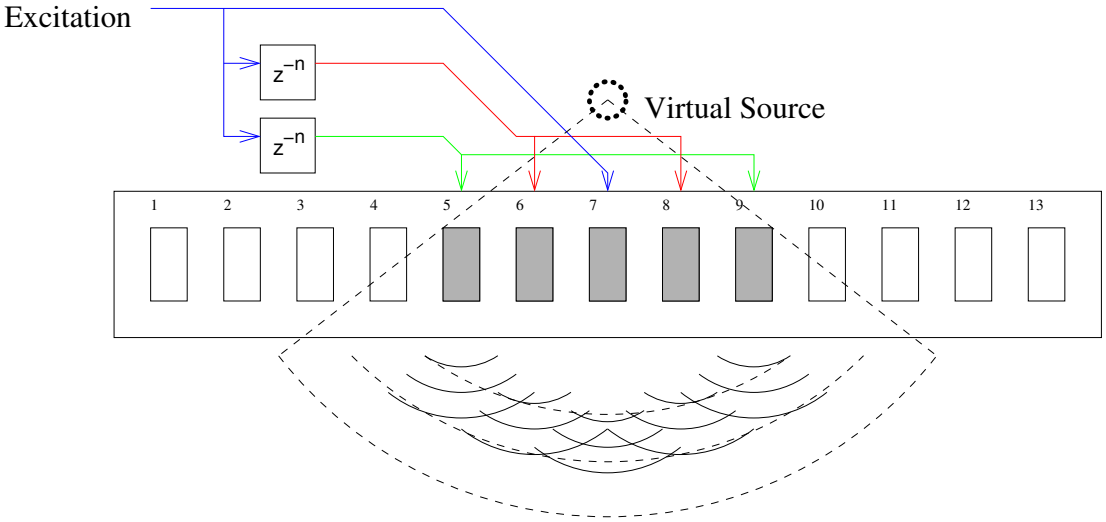

Figure 2.13: A virtual ultrasound source behind the transducer

The delays for each element comprising the virtual source are chosen to create an approximately spherical or cylindrical wavefront. This can emanating from the centre-most of the elements comprising the source, or from a point located in front of or behind the transducer. Figure 2.13 depicts a virtual source located behind the transducer. Virtual sources may be placed at locations unrelated to the element pitch. This property may be exploited to reduce the magnitude of grating lobe artefacts in sparse STA imaging by breaking up the periodicity of the elements in the synthesised aperture.

2.8 Ultrasonic Velocity Estimation

The earliest ultrasound velocity measurement devices [35, 80, 96] were Doppler flow meters: continuous-wave devices that estimated blood flow velocity using the Doppler effect (see Section 2.3). Modern ultrasonic velocity estimation systems are usually PW devices that compare two or more time-adjacent received pulses to build up a profile of the velocities present within the transducer's field. The velocity information is typically displayed using different colours

to represent the direction of motion and colour intensity to indicate its magnitude. For historical reasons, this is often still referred to as *Doppler ultrasound*, although few of the velocity estimation algorithms currently in use actually rely on the Doppler shift.

The majority of motion estimation techniques estimate the component of velocity in the direction of beam propagation. This is Doppler ultrasound in the conventional sense. *Transverse Doppler* techniques [67] estimate the velocity component perpendicular to the beam. Vector Doppler systems combining the techniques have been proposed in the literature [66] but not, to the best of this author's knowledge, commercially implemented. Only methods that estimate the component of velocity in the direction of the ultrasound beam axis will be discussed in the next section as these are the most relevant to this thesis. During an early stage of this thesis research, a range of these methods were implemented in MATLAB and evaluated using some experimental data provided by Bennett, collected during the course of his own thesis research [13]. Some broader reviews of the velocity estimation literature can be found in [30, 41, 45].

Ultrasound velocity estimation may be viewed as a two dimensional spectral estimation problem. Blood flow and tissue velocities cannot usually be determined from a single measurement as any frequency shift due to the Doppler effect is significantly smaller than and obscured by the frequency-shift due to attenuation, unless the vessel of interest is very close to the skin. Instead, reflection data is usually recorded from two or more pulses transmitted towards the same focus and velocity estimates are made based on the similarities and differences between successive reflections. The number of consecutive pulse echoes used to form a single velocity estimate is commonly referred to as the *ensemble length*. Echo data is generally organised in 2-D form, with one axis representing depth or *fast time* and the other representing ensemble length or *slow time*.

Two dimensional Fourier analysis of a series of ultrasonic echoes from the same sample volume can reveal a wealth of information on the velocities present within it. A number of considerations render this approach unsuitable for real-time colour-flow imaging, however. An inherent limitation of the approach is the high number of signal samples required to obtain a fine frequency-resolution. In the context of a CW device, this entails a loss of time resolution and, in many velocity imaging applications, the time-varying behaviour of the anatomical feature under observation is of interest. This is also the case in a pulsed-wave context, with the additional consideration that the spatial resolution of a pulse-echo system is determined by the length of the analysis window used. In the context of colour-flow imaging, an FFT based

approach reveals more information per sample volume than can be usefully overlaid on a B-mode image - i.e. a large amount of computational effort is expended to obtain data on all the velocities present within each sample volume, but only a single value is displayed for each.

The majority of algorithms developed for real-time velocity imaging try to track the changes in the spectrum between two or more time-adjacent pulses. They implicitly assume that the sample volume under analysis is sufficiently small (or the feature to be imaged sufficiently large) that the majority of the fluid or tissue it contains is moving in approximately the same direction at approximately the same velocity. This assumption is reasonable for moving tissue and for blood in regular pulsatile flow.

The received signal from each sample volume consists of the overlaid echoes of the randomly-distributed scattering-centres contained within (or passing through) it during one pulse-period. If the volume is static, the round-trip times for the received echoes remain constant between one pulse-repetition period and the next, as do the phase-relationships between them. If the scattering centres are in motion the round trip times for echoes received from the sample volume vary from one pulse-repetition period to the next but the phase-relationships between the echoes are preserved, provided that the centres are moving coherently and that the PRF is high enough that the majority of the scattering centres remain in the sample volume between one pulse and the next.

There is a certain amount of confusion in the terminology used in the velocity estimation literature which can be traced to two slightly different ways of looking at a set of pulses. Some authors regard a set of time-adjacent received pulses as separate sets of one-dimensional data, denoted by $r_i(t)$, say, while others choose to regard the same data as a single two dimensional signal, denoted $r(i,t)$. As a result, the first set of authors tend to discuss their algorithms in terms of the *cross*-correlation of the one-dimensional signals $r_i(t)$ whereas the second set will describe the same operation in terms of the 2-dimensional *auto*-correlation function of the signal $r(i,t)$. In this document, the first approach has been used to describe those techniques that estimate velocity using two time-adjacent received signals. For those methods that use a larger set of received signals for the calculation of individual velocity estimates, the second approach was felt to be more appropriate as it allows for clearer mathematical notation.

Another potential source of confusion stems from attempts at categorisation of the velocity algorithms. This can be done along a number of lines:

Phase-shift vs. Time-shift estimation methods: Phase-shift estimation methods derive their velocity estimates from the phase relationships between time-adjacent received ultrasonic signals, whereas time-shift estimation methods aim to track groups of scattering centres from one pulse period to the next using the correlation function or some other measure of similarity.

Narrow-band vs. Wide-band systems: In a narrow-band system, the transmitted pulse is comparatively long and most of the signal energy is concentrated in a narrow band of frequencies. In a wide-band system, the excitation pulse is shorter (although this is not necessarily the case for systems using pulse compression – see Chapters 3 and 4) and the signal energy is spread over more of the available spectrum. There is a tendency to associate phase-shift estimation methods with narrow-band systems and time-shift estimation methods with wide-band systems, a generalisation which holds of the 1-D Auto-correlator 2.8.1 described below and for RF cross-correlation 2.8.2 but is inappropriate for some of the more sophisticated algorithms. Long narrow-band pulses are often used in blood-flow velocity estimation, as the back-scatter coefficient for blood is very low and the low SNR obtained using the shorter pulses typically used in B-mode imaging can reduce estimation accuracy.

Base-band vs. Radio-frequency methods: Base-band velocity-estimation methods work with quadrature-demodulated Doppler signals, whereas RF methods work directly with the received ultrasonic signals. Working with base-band signals allows a significant reduction in sampling frequency and computational requirements, but the demodulation of ultrasonic echo signals can be problematic as the various physical processes acting on a wave propagating through the body combine to affect its shape and spectral content in a depth-dependent fashion. The 1-D Auto-correlator takes base-band signals as its input whereas the RF Cross-correlation algorithm works directly with the RF signals. Other methods, like the 2-D Auto-correlator, can be adapted to work with either. The growth in processing power in recent years has made it more feasible to work directly with the RF signals, and this approach is now encountered more often in the literature.

There is nothing inherently problematic about any of the classifications listed above, but they relate more to the implementation details or context of a given algorithm than they do to their performance. A more meaningful set of categories for these algorithms may be constructed based on the information content of the input signal [58]. Methods like the 1-D Auto-correlator

reduce the full 2-dimensional set of back-scattered echo data to a 1-dimensional set of demodulated quadrature samples. Others, like the RF Cross-correlator and the 2-D Auto-correlator, rely on the full 2-D data set and exhibit greater resistance to depth-dependent and non-linear effects.

2.8.1 The Kasai Algorithm / 1-D Auto-Correlator

The first real-time velocity imaging systems were developed by Namekawa and Kasai in the early 80s and used a phase-shift velocity estimation technique based on the work of Miller and Rochwarger [61]. Their algorithm is known as the auto-correlation algorithm as it is derived from the relationship between the power spectrum of a signal and its auto-correlation function. Variations on this auto-correlation algorithm are still at the heart of a large proportion of the clinical scanners in use today although some more recently proposed algorithms that work directly on the received RF signals offer a number of advantages and have been the focus of much more research effort in recent years. Kasai's auto-correlation algorithm [50] estimates the change in phase of the demodulated quadrature components of the received signal between two or more time-adjacent pulses. In effect, this methods track $\delta\theta$, the change in phase of the dominant echo emanating from within the sample volume, from one pulse period to the next. The velocity corresponding to this change in phase may then be calculated using the relationship $v = \frac{\delta\theta f_s}{2\pi f_c}$, where f_c is the centre frequency of the transmitted pulse and f_s is the system sampling frequency. Hoeks et al. [43] reported a significant reduction in estimate variance using a modification of the auto-correlation method. As scattering centres are distributed randomly throughout the volume, integrating over more than one period of f_c fails to improve the estimate of the instantaneous quadrature components. They have proposed an approach whereby the observation window is divided into sub-sample volumes, each with a length of one period of f_c. The change of angle is calculated independently for each sub-sample volume and the average of the individual values of $\delta\theta$ used to estimate the overall velocity. A disadvantage of phase-shift based methods is that they are prone to aliasing in the presence of velocities corresponding to a phase shift of greater than $\pm\pi$ radians in one pulse period. One advantage of Kasai's algorithm is its lack of computational complexity when compared to some of the time-shift estimation methods. If the demodulation and integration of quadrature samples is performed prior to digitisation of the signals, a phase-shift velocity estimation system may safely be sampled at a frequency considerably lower than that required for an equivalent time-shift estimation system. With the advent of relatively cheap, fast digital processing hardware in

recent years, real-time processing of RF ultrasound signals has become more feasible and these last considerations have become less relevant.

2.8.2 The RF Cross-Correlation Algorithm

Time-shift velocity estimation methods estimate the change in position of a group of scatterers between two or more time-adjacent pulses. The simplest of these is the RF cross-correlation algorithm, which serves as a good starting point for a discussion of this family of velocity estimation techniques.

In the absence of motion within a given sample volume, the cross-correlation function of two time-adjacent received echo signals should have a peak at zero lag. If the majority of the scattering centres contained in the sample volume are moving coherently with velocity v_d, this central peak of the cross-correlation function will occur at a lag value of about $\frac{v_d}{f_r} \times \frac{f_s}{c}$, where f_r is the pulse repetition frequency and c the speed of sound in the medium.

At first glance, this method would appear to be immune to aliasing problems provided the analysis window is no shorter than the excitation pulse, as it measures the change in position of a group of scatterers. For an unmodulated excitation sequence, this is not necessarily the case. Consider a conventional pulse-echo Doppler system, in which the transmitted pulse is a number of cycles of an ultrasonic wave. The auto-correlation of such a sequence can be seen in Figure 2.14 (a). It has a strong central peak but very high side-lobes at intervals of λ, the wavelength of the transmitted pulse. The received signal from each sample volume in such a system is the sum of a number of reflections of different amplitudes and phases, each of which has been affected by non-linear propagation, frequency-dependent attenuation and the other physical processes discussed earlier. The cross-correlation sequence of two such signal segments from Bennett's experimental data can be seen in Figure 2.14 (b). These particular signal segments are time-adjacent echoes from a sample volume whose contents are moving at an average velocity of about 23 mm/s, received about 1ms apart. Their cross-correlation sequence has a strong component at f_c, the central peak of which occurs at a shift of about 1.7 samples to the left of zero lag (interpolating visually), corresponding to a velocity estimate of about 25mm/s. A search for the maximum peak would pick that found about 20 samples to the right of zero lag, a shift corresponding to a much higher velocity in the opposite direction. In order to avoid this issue, it is necessary to constrain the peak search to 0.5λ in either direction. Velocities corresponding to a shift in excess of this value will give rise to aliased estimates.

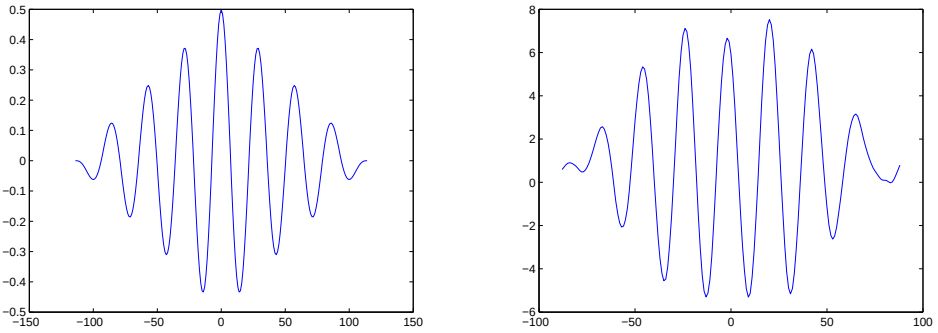

(a) Auto-correlation of a 4-cycle pulse

(b) Cross-correlation of received echoes

Figure 2.14: Correlation of transmit pulse and received echoes

Some authors have reported success using the Sum Squared Difference (SSD) in place of the cross-correlation sequence of time-adjacent returns as a measure of similarity, particularly in spectral elastography and 2-D velocity tracking [48, 55, 89].

2.8.3 The Cross-Correlation Model

The Correlation Interpolation Algorithm, or Cross-Correlation Model (CCM), [24], [44] is based on the notion that a given spectral power distribution will produce a cross-correlation (or 2-D auto-correlation) function of known shape and offers a number of advantages over the RF cross-correlation algorithm. This signal model allows the velocity to be expressed in terms of the 2-D auto-correlation function evaluated at five fixed points as opposed to the $2N - 1$ (where N denotes the length in samples of one cycle of the transmit pulse) estimates required by the RF cross-correlation algorithm. Unlike the RF cross-correlator, this method doesn't require a separate interpolation stage as the velocity estimate is calculated directly from the five points on the auto-correlation surface and the only sampling requirement is that the RF signal is sampled properly according to the Nyquist criterion. Although the model is based on the assumption of a narrow signal bandwidth, it also performs well with wide-band signals. Its performance is determined mainly by the number of samples used, i.e. the two-dimensional "area" in the fast-time/slow-time plane to which it is applied.

2.8.4 The 2-D Auto-Correlator / Complex Cross-Correlation Model

The 2-D Auto-correlator [58] [59] derives the mean axial velocity by estimating both the Doppler and mean RF frequencies. This compensates for random fluctuations in the RF frequency which cause similar fluctuations in the Doppler frequency. In addition, it can potentially compensate for bias due to frequency-dependent attenuation. It can be described in terms of the 2-D Fourier transform of the set of consecutive RF returns. When successive RF returns are translated versions of each other (due to target motion), the 2-D spectrum is non-zero only along radial line segments of the frequency plane with slope proportional to the amount of translation. It is possible to estimate this slope directly in the time domain by evaluating the phase of the auto-correlation of the analytic version of the received signal at just two lags. A useful property of the 2-D auto-correlator is that it can be applied either to the analytic version of the RF signal or to the complex demodulated signal.

The Extended Auto-correlation Method (EAM) [53] is an attempt to correctly identify velocity shifts beyond the Nyquist limit. A candidate phase shift, θ_c in the interval $\pm\pi$ is identified using the 2-D Auto-correlator and the magnitude of the correlation function calculated at points corresponding to $\theta_c \pm 2n\pi$. The maximum value is then taken to be the most likely estimate, though this author remains unconvinced of the validity of the approach for the same reasons alluded to in Section 2.8.2.

The Complex Cross-correlation Model (C3M) [15] [54] may also be used as the basis of a 2-D mean frequency estimator. It produces a velocity estimate mathematically identical to the 2-D Auto-correlator, but also allows the derivation of explicit expressions for the bandwidth, SNR and quality factor (Q-factor) of the system. It is derived from the same complex cross-correlation model as the CCM, facilitating a comparison of the two (and, by extension, of the CCM and 2-D Auto-correlator). The CCM is based on the real part of the model and assumes a narrow spatial bandwidth. This assumption will cause a small bias in the estimate, the magnitude of which is a function of the mean velocity and of the Q-factor of the signals received. The C3M makes no such assumption and gives an unbiased estimate of the velocity, one independent of the bandwidth of the transmitted pulse. It requires the computation of a number of complex cross-correlation coefficients and the calculation of the Hilbert transform of the received RF signal, involving in excess of twice as many calculations per sample point as the CCM.

2.9 Conclusions

The performance of an imaging system is typically described in terms of quantitative features: primarily resolution and dynamic range or SNR. In ultrasonic imaging, the axial resolution is determined by the pulse duration or, if using signal compression as discussed in Chapters 3 and 4, its bandwidth. Azimuthal and elevational resolution are both functions of pulse frequency and aperture width, which is likely to be determined by constraints imposed by the application rather than by the manufacturing process.

An increase in the frequency of the imaging signals used will increase axial resolution by increasing pulse bandwidth while simultaneously increasing azimuthal and elevational resolutions. As described in Section 2.3, however, the majority of the mechanisms contributing to attenuation in ultrasonic media are highly frequency-dependent and increases in imaging frequency can result in significant increase in signal attenuation, which can drastically reduce the useful depth of imaging in systems with limited SNR.

Sinusoidal excitation signals have traditionally been used in medical ultrasonic pulse-echo imaging systems since the advent of the technology in the 1940s. Using these unmodulated excitation signals, the peak power limit is reached long before the average power limit if image resolution is to be maintained, as discussed earlier in this chapter. Beyond this point, an increase in pulse length offers the only avenue for further gains in SNR (and thus depth-of-imaging). Simply lengthening the pulse, however, will have the effect of degrading the range resolution of the system, as the bandwidth (and thus resolution) of such a system is inversely proportional to the duration of the transmitted pulse, giving rise to a compromise between imaging depth and resolution.

Since the early 1970s [91], pulse compression techniques have been proposed in the ultrasound literature as a method of maintaining range-resolution while increasing SNR. In pulse-compression imaging systems, frequency- or phase-modulation is used to maintain bandwidth while increasing pulse length. Received reflections are correlated with the emitted pulse or a related sequence designed to optimise some desired parameter at the output. This compresses the majority of the energy of individual pulse reflections into a duration shorter than that of the transmitted signal, usually related to the reciprocal of the signal bandwidth, and increases SNR at the filter output. Chapter 3 contains an introduction to pulse compression and review of the literature related to pulse-compression imaging, while a range of signals and filters are com-

pared in Chapter 4, using the simulation tools described earlier in this chapter and experimental facilities provided by our research partners.

Chapter 3
Coded Waveforms in Medical Ultrasound

3.1 Introduction

Pulse compression techniques have been used in radar and sonar applications since the 1950s [83]. The use of coded excitation in medical ultrasound, although initially suggested in the late 1970s [86, 87], has until relatively recently attracted less research interest than in its sister disciplines. The frequency- and depth-dependent effects alluded to in Chapter 2 degrade the integrity of the reflected waveform causing difficulties in the design of an appropriate receiver. A mismatch in the receiver can occlude the effects of scatterer velocity on the received signal, particularly when combined with the various other physical processes at work on the propagating signal . The high dynamic-range requirements of diagnostic imaging methods also translate to more stringent requirements for the correlation properties of the transmitted signal. In recent years, the ready availability of fast, inexpensive digital hardware has facilitated the development of commercial systems using pulse compression, the first of which were manufactured by General Electric in the late 1990s [46]. Continued growth in computing power in the last decades has facilitated the refinement of existing techniques and the development of new signal coding schemes and processing methods for medical ultrasonic imaging.

This chapter provides the theoretical background to the simulation study of coded waveforms for high-frequency imaging in Chapter 4 as well as a review of previous research in the area of coded signals for ultrasonic imaging. Section 3.2 contains an introduction to coded waveforms and pulse compression. A range of signal coding and filtering schemes current in the literature are reviewed in Section 3.3 and their relative merits and demerits discussed in terms of the challenges surrounding the adoption of pulse compression techniques in diagnostic ultrasound. Some conclusions are presented in Section 3.4.

3.2 Signal Modulation and Pulse Compression

A sinusoidal signal of duration T, amplitude A, and centre frequency f_c may be written:

$$e_{\text{unc}}(t) = A\cos(2\pi f_c t) \tag{3.1}$$

A signal of this form has a bandwidth $B = \frac{1}{T}$ and a unity *time-bandwidth (TB) product*. Altering the instantaneous amplitude and/or phase of such a pulse according to a predefined pattern can increase its bandwidth without reducing its duration or increase its duration while preserving its bandwidth, resulting in a TB product greater than unity. Any signal of this type is referred to as a *coded waveform* or a *pulse compression waveform*. When a long modulated pulse is processed with an appropriate filter, the majority of the signal energy may be *compressed* into a shorter duration to provide an increase in SNR, known as the *coding gain* or *GSNR*, relative to the unfiltered pulse. This process may be used to increase SNR in peak-power limited systems.

The TB product, sometimes referred to as the *compression factor* or *coding gain* [78], is frequently used as a figure of merit when discussing pulse compression. For a signals with a constant amplitude envelope, the associated increase in SNR is

$$GSNR = 10\log_{10}(TB)^2 = 20\log_{10}(TB) \tag{3.2}$$

3.2.1 Signal Modulation

The signals used in ultrasonic imaging can typically be expressed in the form:

$$g(t) = a(t)\cos\left(2\pi f_c t + \phi(t)\right) \tag{3.3}$$

where f_c represents the pulse carrier or centre frequency, $a(t)$ represents the pulse amplitude envelope as a function of time, t, and $\phi(t)$ is a phase or frequency modulation term.

The instantaneous phase of a pulse of this form is:

$$\theta_i = 2\pi f_c t + \phi(t) \tag{3.4}$$

and its instantaneous frequency is:

$$f_i = \frac{1}{2\pi}\frac{d}{dt}\left(2\pi f_c t + \phi(t)\right) \tag{3.5}$$

$$= f_c + \frac{1}{2\pi}\frac{d}{dt}\phi(t) \tag{3.6}$$

Amplitude modulation reduces the ratio of average to peak transmission power, reducing transmission efficiency, and as such is less attractive for use in pulse-compression systems. The phase function may be varied continuously (continuous-phase modulation or frequency modulation) or in steps (discrete-phase modulation or phase-coding).

The complex-valued *analytic representation* or *pre-envelope* [77] of a real-valued signal is useful in the description and derivation of signal modulation techniques. The spectrum of any real-valued signal displays Hermitian symmetry, i.e. the negative frequency components are the complex conjugates of the positive frequency components. Given a real signal $g(t)$ with Fourier transform $G(f)$:

$$G(f) = E^*(-f) \tag{3.7}$$

where $E^*(f)$ represents the complex conjugate of $G(f)$. The analytic representation of $g(t)$, written $\dot{g}(t)$, is a complex valued signal, formed as:

$$\dot{g}(t) = g(t) + j\hat{g}(t) \tag{3.8}$$

where $\hat{g}(t)$ represents the Hilbert transform of $g(t)$ [1]. The Fourier transform of $\dot{g}(t)$ is:

$$\dot{G}(f) = G(f) + jG\hat{(}f) = \begin{cases} 2G(f) & f > 0 \\ G(f) & f = 0 \\ 0 & f < 0 \end{cases} \tag{3.9}$$

Using the analytic signal representation, manipulations of real signals involving multiplication of sinusoids become manipulations of complex signals involving multiplication of powers of e, e.g $\sin(\omega_1 t)\sin(\omega_2 t + \theta)$ becomes $e^{j\omega_1 t}e^{j[\omega_2 t+\theta]} = e^{j[(\omega_1+\omega_2)t+\theta]}$. This property helps simplify the convolution integrals encountered regularly in signal modulation and facilitates the separation of amplitude and phase envelopes.

In analytic form, Equation (3.3) becomes:

$$\dot{g}(t) = a(t)e^{j(2\pi f_c t + \phi(t))} \tag{3.10}$$

$$= a(t)e^{j2\pi f_c t}e^{j\phi(t)} \tag{3.11}$$

The amplitude and phase modulation terms may be grouped together as the *complex envelope* $\ddot{g}(t)$, such that:

$$\ddot{g}(t) = a(t)e^{j\phi(t)} \tag{3.12}$$

Equation (3.10) may then be re-written in terms of the complex envelope as

$$\dot{g}(t) = \ddot{g}(t)e^{j2\pi f_c t} \tag{3.13}$$

3.2.2 Pulse Compression / Filtering

The reference filter for processing pulse compression waveforms is the *matched filter*. It may be realised simply by time reversing a copy of the transmitted pulse and is the filter that yields the maximal SNR in the presence of additive stochastic noise. This increase in SNR comes at the cost of range side-lobes introduced by the decoding process, as a portion of the signal energy is spread out over the region to either side of the filter main-lobe. The side-lobe characteristics of a purely phase-modulated signal are unacceptably high for imaging purposes and may be manifested as "ghosting" artefacts or cause a highly reflective element in the field to mask less highly reflecting elements nearby. A wide-range of side-lobe reduction techniques have been investigated in the literature, a number of which are discussed with reference to ultrasonic imaging in Section 3.3 and Chapter 4. Side-lobe reduction is more readily accomplished for the continuous-phase modulated signals described in Section 3.2.3 than for the discrete-phase modulated signals described in Section 3.2.4.

3.2.3 Continuous-Phase Modulation / Frequency Modulation

The instantaneous phase of an continuous-phase modulated signal varies continuously as a function of time: this means that its instantaneous frequency is a continuous function and its time-response exhibits no sharp phase transitions or discontinuities as illustrated in Figure 3.1 (a). Signals of this type are occasionally referred to as *chirps*, due to the nature of the sounds they produce at audible frequencies, or, more commonly, as *frequency-modulated* (FM) signals.

The example in Figure 3.1 (a) is an upward (in frequency) sweeping *Linear-FM* (LFM) signal,

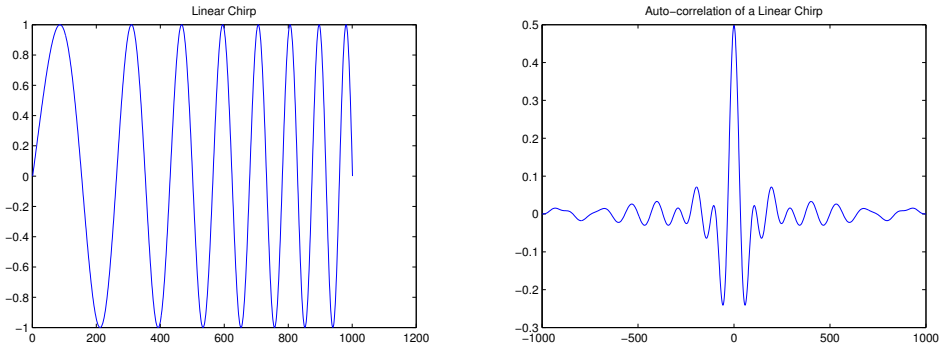

(a) Linear FM-Chirp (b) Auto-correlation of Linear Chirp

Figure 3.1: Linear FM signal and its auto-correlation sequence

or LFM up-chirp, so called as its instantaneous frequency increases as a linear function of time. Equation (3.14) represents a Linear FM signal of duration T and bandwidth B in analytic form:

$$\dot{g}_{fm}(t) = a(t)e^{j2\pi(f_c+\frac{B}{T}t)t}, \qquad -\frac{T}{2} \leq t \leq \frac{T}{2} \tag{3.14}$$

This expression is *acausal*, i.e. non-zero for $t < 0$. It may be expressed in *causal* form [74] as:

$$\dot{g}_{fm}(t) = a(t)e^{j2\pi(f_c+\frac{B}{T}[t-\frac{T}{2}])t}, \qquad 0 \leq t \leq T \tag{3.15}$$

with complex envelope:

$$\ddot{g}_{fm}(t) = a(t)e^{j2\pi\frac{B}{T}[t-\frac{T}{2}]t}, \qquad 0 \leq t \leq T \tag{3.16}$$

FM signals are perfectly *band-limited*: they contain no frequency components outside the range $f_c \pm \frac{B}{2}$ due to the lack of discontinuities in their instantaneous phase and frequency functions.The auto-correlation sequence (or matched filter response) of a linear FM chirp may be seen in Figure 3.1 (b). The side-lobe levels tend to fall off with increasing distance from the main-lobe of the filter response, as is typical of LFM signals. Side-lobe levels may be reduced somewhat by replacing the linear phase term in (3.15) with a more complex expression designed to optimise some parameter at the filter output, producing a *non-linear FM* (NLFM) signal.

As the instantaneous frequency of an FM signal changes continuously, time-domain amplitude

weighting can also be used to shape the frequency spectrum of the signal. A comprehensive review of the characteristics and effects of various data windows may be found in a seminal paper by Harris [40]. The time-frequency domain mapping is straightforward for an LFM signal: as its instantaneous frequency increases linearly, time domain multiplication of the signal by an amplitude weighting function equates directly to multiplication of the signal frequency spectrum by the same amplitude weighting function scaled to match the signal bandwidth. A weakness of this approach is that it produces an asymmetrical spectrum in the presence of the frequency shifts caused by attenuation, distorting the weighting effect and potentially introducing high side-lobes. This can be addressed by bilateral weighting of the excitation pulse spectrum and that of the receive filter [78]. All of these measures tend to reduce the signal bandwidth and thus increase the main-lobe width, decreasing resolution. Amplitude weighting also reduces the transmission efficiency, thereby decreasing the SNR gain provided by signal coding. These topics are discussed in detail in relation to the construction of FM signals and filters for use in ultrasonic imaging in Chapter 4.

3.2.4 Discrete-Phase Modulation / Phase Coding

A discrete-phase coded pulse of duration T is divided into L sub-intervals of equal duration, $T_b = \frac{T}{L}$. Each sub-interval is assigned an initial phase according to an L-bit phase code, $\phi[l]$. The bit period, T_b, is usually defined in relation to the pulse centre frequency f_c. The analytic form of a signal of this type is given in Equation (3.17). Throughout this thesis, the square brackets "[]" are used to represent discrete sequences, whereas parentheses "()" are used to represent functions or signals that are defined continuously on at least one dimension.

$$\dot{g}_{\text{pc}}(t) = \sum_{l=0}^{L-1} c[l]\text{rect}_c\left(\frac{t - lT_b}{T_b}\right) e^{jf_c t} \tag{3.17}$$

where $\text{rect}_c(t) = \text{rect}(t - \frac{1}{2})$ is a causal version of the rectangular function:

$$\text{rect}(t) = u(t + \tfrac{1}{2}) - u(t - \tfrac{1}{2}) \tag{3.18}$$

$$\text{rect}_c(t) = u(t) - u(t - 1) \tag{3.19}$$

and $u(t)$ is the *Heaviside step function*:

$$u(t) = \begin{cases} 1 & t \geq 0 \\ 0 & t < 0 \end{cases} \tag{3.20}$$

and $c[l] = e^{j\phi[l]}$. The individual phases $\phi[l]$ may be chosen freely (*poly-phase* codes) or from a discrete set of phases.

The complex envelope of (3.17) is:

$$\ddot{g}_{\text{pc}}(t) = \sum_{l=0}^{L-1} c[l]\text{rect}\left(\frac{t - lT_b}{T_b}\right) \tag{3.21}$$

Some sources [78] define the phase-coded pulse differently, as:

$$g_{\text{bb}}(t) = \sum_{l=0}^{L-1} \cos(\phi[l])\text{rect}\left(\frac{t - lT_b}{T_b}\right) \tag{3.22}$$

$$= \text{re}[\ddot{g}_{\text{pc}}(t)] \tag{3.23}$$

i.e. the real part of Equation (3.21). Strictly speaking, (3.22) does not represent a phase-modulated signal but rather a signal modulated with the discrete amplitude sequence $\cos(\phi[l])$. Binary-phase coding is a special case of phase coding, where the phases $\phi[l] \in \{0, \pi\}$ radians and $c[l] \in \{1, -1\} \quad \forall l$. In this case, $\ddot{g}_{\text{pc}}(t)$ is wholly real and $g_{\text{bb}}(t) = \ddot{g}_{\text{pc}}(t)$. A binary-phase coded signal of this type is sometimes referred to as a *base-band* or *direct-sequence* phase-coded signal.

A wide range of discrete phase codes have been developed for use in communications and data storage applications. The feature of particular interest in selecting codes for imaging is the range side-lobe level. The optimal codes in this sense are the Barker codes [10] in that the height of their maximum auto-correlation side-lobes are $\frac{1}{L}$ times that of the main-lobe, where L is the code length. An example of a direct-sequence Barker-coded signal and its auto-correlation sequence may be seen in Figure 3.2.

In many applications, a phase-code is used to modulate a *chip* or *basis* function $b(t)$ matched

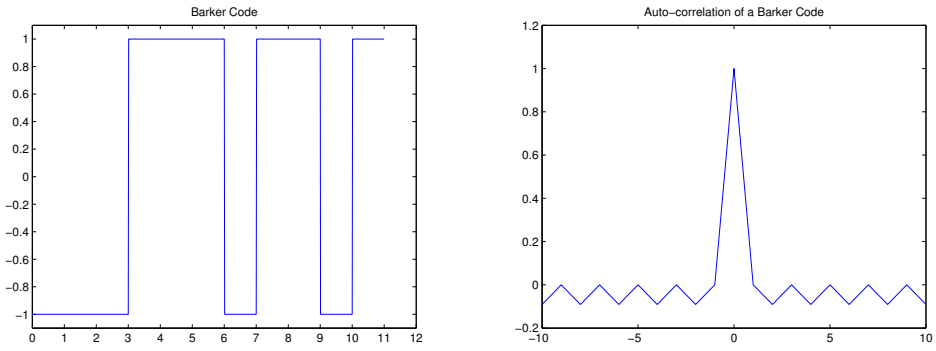

(a) 11-bit Barker Code (b) Auto-correlation of Barker Code

Figure 3.2: 11-bit Barker code and its auto-correlation sequence

to the characteristics of a transducer or communication channel. This may be expressed as:

$$b(t) = \begin{cases} a_b(t)\cos(2\pi f_c t + \phi_b(t)) & 0 \leq t \leq T_b \\ 0 & t > T_b \end{cases} \tag{3.24}$$

or in analytic form:

$$\dot{b}(t) = e^{j2\pi f_c t} a_b(t) e^{j\phi_b(t)}, \qquad 0 \leq t \leq T_b \tag{3.25}$$

which has complex envelope:

$$\ddot{b}(t) = a_b(t) e^{j\phi_b(t)}, \qquad 0 \leq t \leq T_b \tag{3.26}$$

Replacing rect$(t - lT_b)$ with $\dot{b}(t)$ in Equation (3.17):

$$\dot{g}_{\text{pc}}(t) = \sum_{l=0}^{L-1} c[l]\dot{b}(t - lT_b), \qquad 0 \leq t \leq LT_b \tag{3.27}$$

which has complex envelope:

$$\ddot{g}_{\text{pc}}(t) = \sum_{l=0}^{L-1} c[l]\ddot{b}(t - lT_b), \qquad 0 \leq t \leq LT_b \tag{3.28}$$

Defining a continuous modulation sequence $c(t)$ such that:

$$c(t) = \sum_{l=0}^{L-1} c[l]\delta(t - lT_b) \tag{3.29}$$

If $c_{xx}[i]$ represents the discrete auto-correlation sequence of the phase sequence $c[l]$ then $c_{xx}(\tau)$, the auto-correlation sequence of the continuous modulation sequence $c(t)$, may be written:

$$c_{xx}(\tau) = \sum_i c_{xx}[i]\delta^2(\tau - iT_b) = \sum_i c_{xx}[i]\delta(\tau - iT_b) \tag{3.30}$$

Using (3.29), Equation (3.27) may be rewritten as:

$$\dot{g}_{\text{pc}}(t) = c(t) * \dot{b}(t) \tag{3.31}$$

Filtering for a signal of this form may be separated into two stages: one matched to $c(t)$, which is non-zero only at integer multiples of the bit period, and the other matched to the chip, $b(t)$. If the signal is binary-phase coded (BPC), $c(t)$ is real and ± 1 valued, and the filter $c(T - t)$ may be realised as a series of $(L - 1)$ additions and subtractions. The filter matched to $b(t)$ is of the order of $\frac{1}{L}$ the length of the signal, and the net result is a significant reduction in the computational cost of filtering, particularly advantageous if processing received signals from large transducer arrays.

Another advantageous property of BPC signals is that the magnitude spectra of their two constituent code symbols are identical, as they're related by sign inversion in the time domain. This property makes them particularly robust to the effects of attenuation encountered in ultrasonic imaging, as demonstrated in Chapter 4.

3.2.5 Complementary Code Sets

A family of phase codes known as complementary codes offers a way to avoid the issue of side-lobe reduction, in theory at least. The auto-correlation functions of the individual codes of the complementary set have side-lobes that may be relatively high in comparison to those of other binary phase codes but are opposite in phase. When summed, the complementary side-lobes of the individual auto-correlation functions cancel and the composite auto-correlation function exhibits no filter side-lobes and a GSNR of $20\log_{10}(NL)$ dB, where N and L represent the number of codes in the set and length of the individual codes respectively. The best known of these codes are the binary Golay codes [18, 37, 38], although poly-phase complementary sequences have also been investigated for use in imaging [51]. Side-lobe cancellation is illustrated in Figure 3.3 for a 4-bit Golay code pair. 'A' and 'B' refer to the auto-correlation sequences of the two codes of the complementary set.

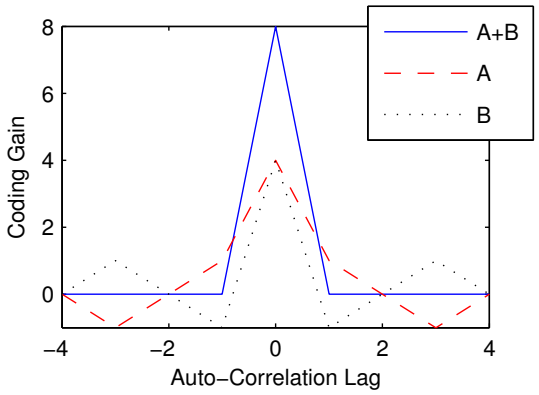

Figure 3.3: Side-lobe cancellation: Auto-correlation sequences of a 4-bit Golay code pair

The expressions for phase-coded signals and their associated filters in Sections 3.2.4 and 3.2.2 may be re-defined for complementary sets of phase codes. Allow $\phi_c[n,l]$ to represent the discrete phases of a complementary set of N phase codes, each of length L, and $c_c[n,l] = e^{j\phi_c[n,l]}$ their associated complex phasors. Define $c_{xx}[n,i]$ as the auto-correlation sequence of the n^{th} code of the set evaluated at the i^{th} lag such that

$$c_{xx}[n,i] = \sum_{l} c_c[n,l]c_c[n,l-i] \tag{3.32}$$

The sum of their auto-correlation sequences is then

$$\sum_{n=0}^{N-1} c_{xx}[n,i] = NL\delta[i] \tag{3.33}$$

Equation (3.29) may be expanded to define a set of modulation sequences $c_c(n,t)$ such that

$$c_c(n,t) = \sum_{l=0}^{L-1} c_c[n,l]\delta(t-lT_b), 0 \leq n \leq N-1 \tag{3.34}$$

and

$$c_{xx}(n,\tau) = \sum_{i} c_{xx}[n,i] * \delta(\tau - iT_b) \tag{3.35}$$

$$\sum_{n=0}^{N-1} c_{xx}(n,\tau) = NL\delta(\tau) \tag{3.36}$$

For a set of complementary codes, Equation (3.31) becomes:

$$\dot{g}_{\text{cpc}}(n,t) = c_c(n,t) * \dot{b}(t) \tag{3.37}$$

$$c_c(n,-t) * g_{\text{cpc}}(n,t) = c_{xx}(n,t) * b(t) \tag{3.38}$$

and the sum of complementary filter outputs may be written:

$$\sum_{n=0}^{N-1} c_c(n,-t) * g_{\text{cpc}}(n,t) = NL\delta(t-T) * b(t) \tag{3.39}$$

3.3 Pulse Compression in Ultrasonic Imaging

The selection of signals for ultrasonic imaging requires a number of often conflicting requirements to be balanced against one another. The primary requirements are to maximise GSNR and signal bandwidth. For any specific imaging system, there are a range of signals which would satisfy these criteria – the challenge is to do so while keeping filter side-lobes below the level at which they will be manifested as visual artefacts in a B-mode image or introduce range ambiguities in velocity estimation applications. The level acceptable in a given system will depend on the system noise floor, GSNR and focal settings, but a main-lobe to side-lobe ratio of 50dB is often quoted in the literature as a desirable target.

Side-lobe issues are exacerbated by filter mismatch due to signal distortions caused by the frequency-response characteristics of the transducer and by propagation through the medium. Received reflections can differ significantly from the signal passed to the transducer, as illustrated in Figure 3.4. A linear frequency-modulated signal signal has been chosen for this illustration due to the direct correspondence between its time-domain and frequency-domain magnitude envelopes.

The LFM signal in Figure 3.4 (a) sweeps a 9.4 MHz bandwidth centred at 7.5 MHz over a period of 10.7 μs, yielding a TB product of 100. It has been weighted with an Elliptical-Tukey window to reduce range side-lobe levels, a process explained in detail in Section 4.4. The finite bandwidth of the transducer effectively weights the frequency-spectrum of the signal on transmit and receive. In Figure 3.4 (b), this effect has been approximated by convolving the weighted-LFM signal of Figure 3.4 (a) with simulated transmit and receive transducer responses. Gaussian-modulated sinusoidal pulses centred at 7.5 MHz with a fractional bandwidth

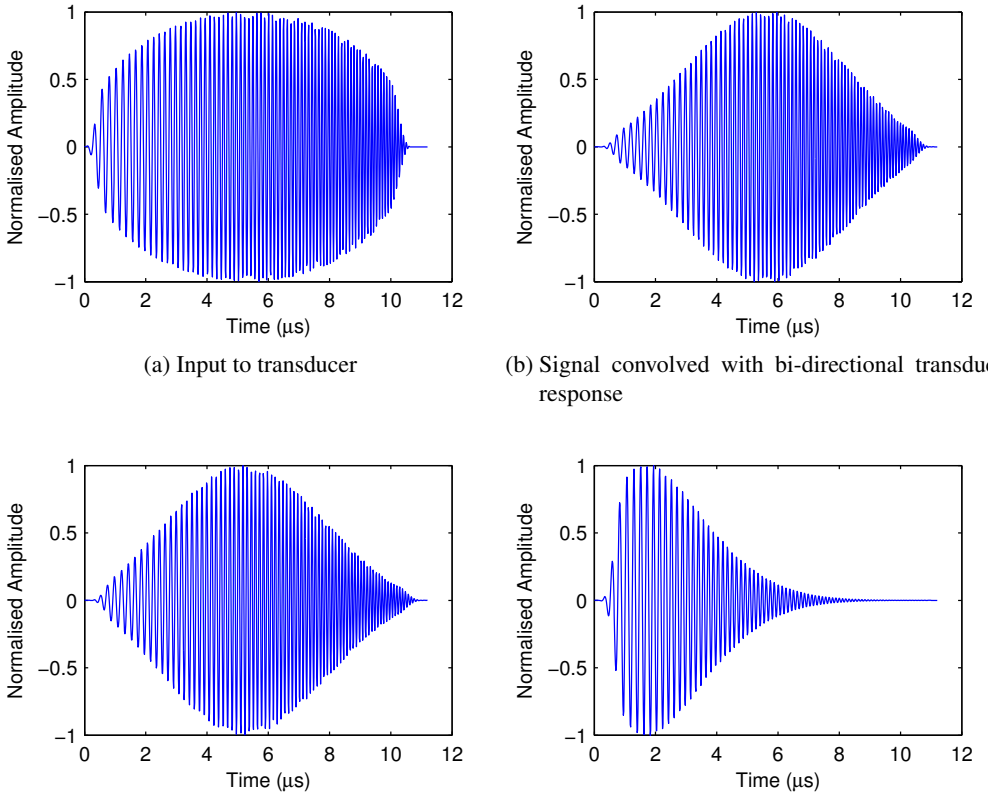

(a) Input to transducer

(b) Signal convolved with bi-directional transducer response

(c) Reflection from point target at 5mm

(d) Reflection from point target at 95mm

Figure 3.4: Effects of the transducer and propagation on a linear-FM pulse

of 83% were used for both.

The effects of propagation in an attenuating medium were simulated using the Field II ultrasound simulation tool described in Section 2.6 and simulated attenuation of 0.5 dB/MHz/cm. The echo from a scatterer at a depth of 5mm shown in Figure 3.4 (c) is relatively unaffected by attenuation, however the highly attenuated echo from a depth of 95mm spectrum in Figure 3.4 (d) shows significant spectral distortion by comparison. In both these figures, propagation delays corresponding to the scatterer depths have been subtracted from the time-scales in order to facilitate comparison with one another and Figures 3.4 (a) and 3.4 (b).

The response characteristics of the transducer may be measured or otherwise estimated and factored into the signal and filter design. The effects of propagation, however, are frequency-dependent and non-linear, causing a mismatch between filter and signal reflections that increases as a function of depth, as illustrated in Figure 3.5. In Figure 3.5 (a), the effects of depth on the spectra of reflected LFM signals have been plotted using a single simulated B-

mode image line through a series of equally spaced point scatterers and the short-time Fourier transform (STFT). Colour has been used to represent magnitude, with red representing higher amplitude frequency components. The effects of attenuation result in a steady reduction in the magnitudes of frequency components across the entire bandwidth of the signal. For Figure 3.5 (b), log-linear Time-Gain Control (TGC) was applied to the data prior to computation of the STFT to highlight the frequency-dependent nature of these effects: the increased attenuation at high frequencies results in a depth-dependent reduction in spectral bandwidth and in the frequency at which the peak signal amplitude occurs. Figures 3.5 (c) and 3.5 (d) provide a further illustration of the effects of attenuation using time- and frequency-domain representations of reflections from single scatterers located at depths of 5mm and 95mm, respectively. Attenuation results in an approximately 60 dB reduction in echo magnitude and shifts the position of the spectral peak from the centre of the pulse (in time and frequency) to the lowest pulse frequency components.

In the majority of cases this mismatch leads to a reduction in GSNR, often accompanied by a degradation in side-lobe performance and/or increase in main-lobe width (and thus reduction in capacity for discrimination/resolution) at the filter output. An increase in side-lobes associated with deep scatterers is not always a cause for concern as the effects of attenuation will have reduced the peak level of the filter output envelope, effectively raising the noise floor relative to the main-lobe peak. Issues will arise, however, if side-lobe levels increase at a greater rate than the SNR loss due to attenuation. The reduction in GSNR is more problematic, as it is most severe at the higher imaging depths at which its benefits are most required.

Hardware implementation considerations also impact on system design. The sampling frequency must be chosen to accommodate the imaging frequency-range of interest, and quantisation of filter coefficients and of sampled signals will affect filter performance and the quality of the final image.

The signal flow for a coded imaging system with an idealised analogue-digital converter (ADC) with an infinitely high sampling resolution is illustrated in Figure 3.6 (a). This idealised system uses *pre-compression*, i.e. filtering is applied to the data from each element in the receive aperture before either ultrasonic beam formation or Time-Gain Control. The order in which these operations take place is relevant as as the latter processes both equate time with depth, while the unfiltered ultrasonic data contains overlapping echo signals from a range of depths that increases in direct proportion to the length of the coded signal.

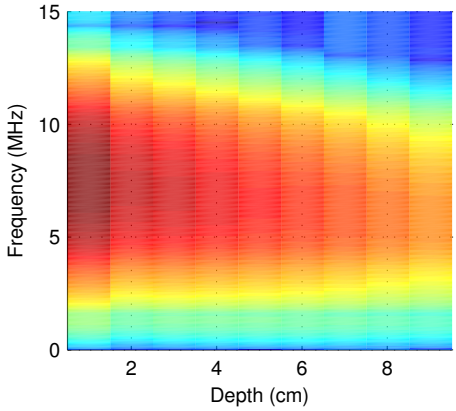

(a) No time-gain compensation

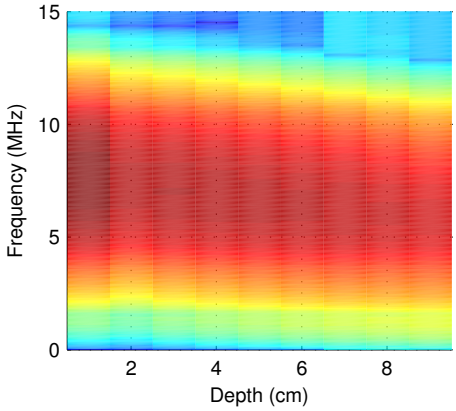

(b) Log-linear time-gain compensation

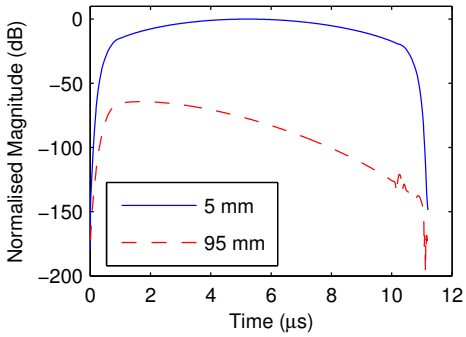

(c) Time-domain magnitude envelopes of point scatterers at 5mm and 95mm

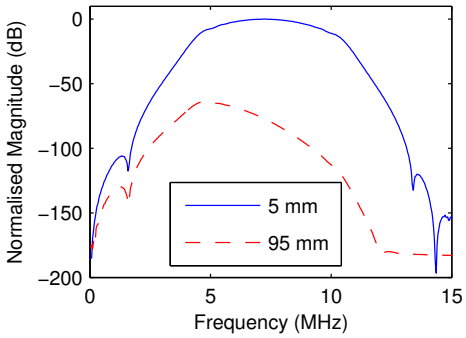

(d) Frequency-domain magnitude envelopes of point scatterers at 5mm and 95mm

Figure 3.5: Variation in spectral characteristics of a linear FM pulse with depth

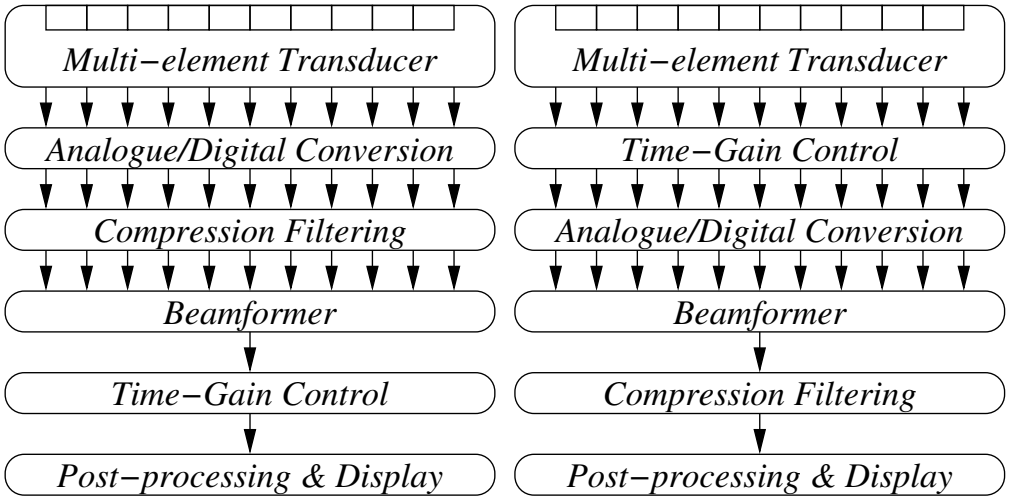

(a) Pre-compression and digital TGC

(b) Post compression and analogue TGC

Figure 3.6: Receive signal paths for an idealised coded imaging system with infinite ADC resolution and for a practical post-filtered coded imaging system

In practical implementations of digital ultrasonic imaging systems, TGC is usually performed in the analogue domain prior to conversion and filtering in order to maximise the limited resolution offered by real-world ADCs. For individual echoes, this deviation from the ideal signal flow is equivalent to an amplitude weighting of the reflected pulse and its impact is minor in comparison to that of frequency-dependent attenuation. In a system using linear FM imaging pulses, the weighting might actually offset some of mismatch caused by attenuation due to the symmetry properties of their magnitude envelopes in the time- and frequency- domains, provided the instantaneous frequency of the pulse sweeps up rather than down.

In some commercial implementations, the order of compression filtering and beam-formation is reversed, as illustrated in Figure 3.6 (b). This is referred to as *post-compression* or *post-filtering*, as the compression takes place after beam-formation, while systems that filter the received signals prior to beam-formation are referred to as *pre-filtering* or *pre-compression* based systems. Post-compression is computationally advantageous in that it reduces the number of filtering operations required by a factor of E, where E is the number of elements in the receive aperture, but its consequences are potentially more severe than are those of moving the time-gain control block. Results published in [14] indicate that the associated error is significant but decreases with increasing depth, as the focusing delays change more rapidly closer to the transducer for geometrical reasons. The error is a complex function of a number of parameters, including the distances between transmit and receive focal points, and is very sensitive to slight errors in the delay values used during beam-formation. A modified beam-formation algorithm is suggested, using which an image line is divided into multiple overlapping regions prior to beam formation and filtering. The window length is a function of the size of focal zone size and the signal length, while the degree of overlap is related only to the signal length. Other authors [52] report that the error associated with post-compression increases with decreasing f-number and suggest the use of orthogonal complementary-coded signal pairs to allow the number of transmits per image line to be increased. Elsewhere, some work published by researchers employed by Hitachi [9] reports a technique called *sub-aperture decoding* in which nested binary-phase codes are used to reduce the decoding error associated with post-compression. The excitation pulse is generated by using a short binary code sequence to modulate a base pulse then modulating the resulting signal with a second short binary code, the rationale being that the decoding error is proportional to the code length and that this approach allows the pulse energy to be maintained while simultaneously using short code sequences and maintaining resolution.

3.3.1 Frequency-Modulated Imaging

The simplest FM signal to transmit is the *pseudo-chirp*, a binary approximation to an FM signal which may be generated using bi-polar pulsers. A system using linear-FM excitation signals of this type is described in [72]. As processing a constant amplitude linear-FM pulse with a matched filter results in side-lobes at about -13dB, a process referred to as *equalisation filtering* is used instead. The filter coefficients are derived by inverting the spectrum of the transmitted pulse. This method offers improved axial resolution to the matched filter but amplifies the relative noise power, reducing the overall GSNR. The side-lobe levels obtained by direct application of this method remain unacceptably high but may be reduced further by zero-padding the spectrum in the frequency domain and allowing the filter to be longer than the transmitted signal, effectively distributing the side-lobe energy over a greater time interval. Side-lobe levels of the order of -40dB are reported. This method for inverse filtering of pseudo-chirp signals has been extended in [57] to include optimisation methods that allow tuning of the main-lobe width and side-lobe levels.

An effective system using weighted LFM excitation signals and a mismatched filter is presented in [62,64,65]. Amplitude weighting of the transmitted pulses is used to reduce the distant range side-lobes associated with ripples in the spectrum of the transmitted signal, while a window function is applied to the filter coefficients to reduce near range side-lobes. Both measures result in a slight reduction in GSNR. The effects of frequency-dependent attenuation are modelled here as a downward shift in the centre frequency of the pulse and it is concluded that the LFM signal is more robust to this effect than either NLFM or BPC signals on the basis of its ridge-shaped ambiguity function. It does, however, require a relatively high time-bandwidth product (of the order of 50 or more) in order to achieve acceptable side-lobe levels, and the long signals this entails increase the likelihood of encountering problems with dynamic focusing and time-gain-control.

In [39], a frequency-domain method is used to design NLFM pulses matched to the transducer bandwidth. First, an ideal magnitude spectrum is constructed in the frequency domain using a Kaiser window centred at the desired imaging centre frequency. This is integrated to obtain an ideal instantaneous frequency curve. A polynomial approximation is fitted to the ideal instantaneous frequency curve using least squares optimisation and the phase spectrum of the desired signal is subsequently obtained by integration of the polynomial. The relaxation of the linear constraint on the frequency-modulation function allows excellent side-lobe performance

to be achieved without resort to mismatched filtering with its implicit reduction in GSNR. Bandwidth-matching increases the transmission efficiency, reducing the amount of energy dissipated as heat at the transducer and results in increased SNR at the filter output. This comes at the expense of a slight reduction in axial resolution due to a reduction in signal bandwidth, although this becomes less evident with increasing depth as the effects of frequency-dependent attenuation on received echoes become more significant. Results are presented indicating that the effects of attenuation are no more severe for NLFM than for LFM.

A technique known as *depth-dependent mismatched filtering* [16], applicable to both LFM and NLFM-based systems, has been suggested as a method of mitigating the effects of attenuation somewhat. Using this approach, received image lines are processed using a bank of filters. Each of its constituent filters is matched to the expected shape of distorted reflections from a different focal depth. The filter coefficients may be derived based on a model of the attenuation characteristics of the medium or on estimates derived from received ultrasonic echoes. The method has been applied successfully for linear FM signals and an improvement in range resolution and penetration depth was reported in [29]. Even with a relatively predictable medium and well designed depth-dependent filter bank, however, some mismatch is inevitable and it is therefore important to choose a robust combination of imaging signal and receive filter.

3.3.2 Phase-Coded Imaging

In systems using BPC signals, an oversampled representation of a binary code is generally used to phase modulate a base sequence or "chip". An advantage of this approach is that it may be implemented using inexpensive bi-polar pulsers. The received pulses may be processed using a decoding filter matched only to the binary code, thus lumping the effects of the transducer response and frequency-dependent attenuation in with the base sequence [19].

Barker codes are widely used in radar and optimal in the sense that they have the lowest uniform side-lobe level of height $\frac{1}{N}$ along the delay axis. The longest of these, however, is the 13-bit Barker sequence. At higher code lengths, the lowest side-lobe levels exhibited by non-Barker codes are of the order of $\frac{2}{N}$ or higher.

A system using BPC signals and extended "spiking" filters derived by spectrum inversion is reported in [92]. Spiking filters for Barker-coded excitation are described in [98]. The method is reported to be effective, although the maximum coding gain achievable is limited by the

maximum Barker code length of 13 and relatively long filters are required in order to bring side-lobe levels below the -50 dB or so typically required for medical imaging. One disadvantage of this approach is that it requires multi-level filter coefficients rather than binary coefficients for matched filtering of a bi-phase code.

Chiao et al. [19] report encouraging results using an oversampled binary code to phase-modulate a base pulse, which can be chosen to compensate for transducer and propagation effects. On receive, the sequence is decoded with the oversampled binary code. This lumps the transducer response, frequency-dependent attenuation and all linear time-invariant effects in with the base pulse so they don't affect decoding.

3.3.3 Complementary-Coded Imaging

The conventional approach to complementary-coded ultrasonic imaging is to transmit all codes of the set sequentially in the same direction before acquiring data for the next transmission focus, thus reducing the system frame rate by a factor of N, where N is the number of codes in the complementary set. This assumes the inter-pulse interval is small enough to cause only minor misalignment – any motion of the subject between acquisition cycles will introduce residual side-lobes due to misalignment of the filter outputs and will broaden and lower the main lobe of the combined filter response, reducing the GSNR.

A range of published work [12,19,20,51,52] suggests exploitation of the potential for waveform diversity inherent to signal coding in order to eliminate the reduction in frame-rate. Two carefully chosen orthogonal coded signals can be transmitted simultaneously and the corresponding reflections separated at the output. If each of the orthogonal codes is a member of a Golay pair and their complements are also orthogonal, complementary coded data may be acquired for two sample volumes over the course of two acquisition intervals. The potential for co-interference may be minimised by using different focusing and apodisation weightings for the orthogonal signals, effectively transmitting them in two different focal directions. This approach successfully addresses the issue of frame-rate reduction, but motion between acquisition intervals can still produce visible misalignment artefacts.

In [51], a mutually orthogonal pair of complementary poly-phase codes is proposed for ultrasonic imaging. As the coded signal pair is simultaneously orthogonal and complementary, both signals may be transmitted in the same focal direction simultaneously, eliminating any issues

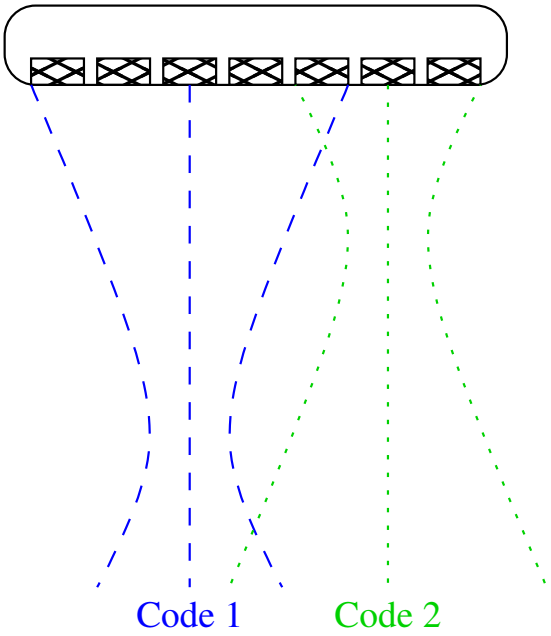

Figure 3.7: Simultaneous parallel beam-forming with orthogonal coded signals

associated with motion between complementary acquisitions. Although the implementation details aren't completely clear, it appears that the real components of the complex phasors were used to amplitude modulate a basis sequence, resulting in a substantial reduction in transmission efficiency and GSNR compared to bi-phase signal coding. In addition, the simulation results presented include only linear depth-dependent attenuation. No assessment of the method's robustness to frequency dependent attenuation can be made on the basis of the published results. In more recent work by the same authors [52], BPC Golay pairs are used and no further reference is made to complementary poly-phase sequences.

Other work [36] suggests exploitation of a property of the 2-bit Golay code pair in order to suppress motion artefacts. Received reflections corresponding to each pulse of the Golay-coded pair are filtered using both codes of the complementary pair. The additional filter outputs are subtracted from the combined Golay filter envelope and apparently cancel misalignment sidelobes. This approach appears to involve gating of decoded signals, meaning cancellation will only be partial for the overlapping reflections encountered in most imaging scenarios. In addition, this cancellation only occurs for the 2-bit Golay pair and fails to compensate for the reduction in compression and axial resolution caused by spreading and lowering of the mainlobe.

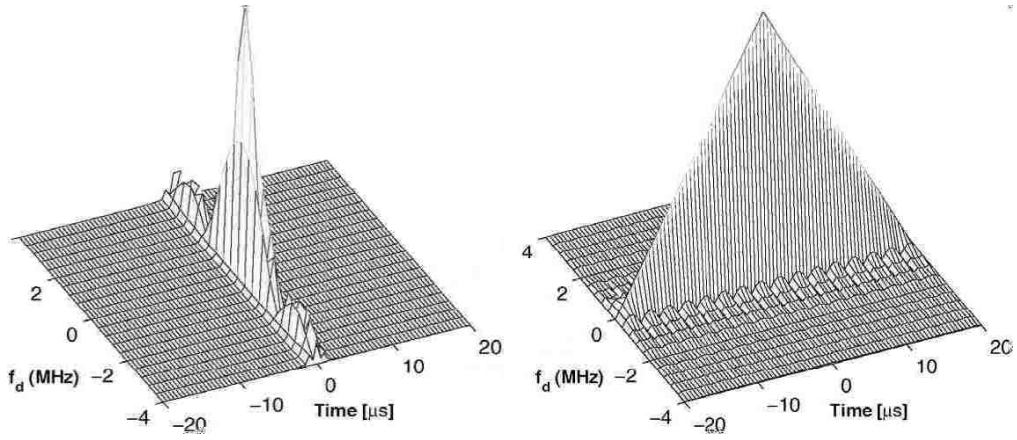

(a) Short Pulse – 4 Cycles (b) Long Pulse – 80 Cycles

Figure 3.8: Ambiguity functions of a 4 MHz unmodulated pulse [62]

3.3.4 Waveform Selection for Medical Ultrasound

Published opinions vary as to the relative suitability of FM and BPC signals for medical ultrasonic imaging. A useful series of articles reviewing the literature on coded excitation in medical ultrasound [62, 64, 65] may be found in a special issue of the *IEEE Transactions on Ultrasonics, Ferro-electrics and Frequency Control*, published in 2005. These display some bias towards FM excitation signals, the focus of the authors' own research efforts. A number of other articles [19,73] in the same special issue focus on some advantages of binary phase-coded waveforms in terms of robustness to attenuation and transducer effects.

The suitability of a range of pulse-compression waveforms for ultrasonic imaging is discussed in [62]. The modulation schemes evaluated were linear FM, tapered linear FM, non-linear FM and binary-phase modulation using a complementary Golay code pair. Simulation results were compared using Matlab and the Field II ultrasound simulation tool [32, 33], both with and without frequency-dependent attenuation. The results are explained with reference to the various signals' ambiguity functions, which estimate a filter's response to a signal which has been shifted in frequency. These are conventionally plotted in three dimensions with one axis representing time another representing frequency mismatch, f_d, and the vertical axis representing GSNR. The matched filter output for a given frequency mismatch may be determined by taking a 2-D section parallel to the time axis through the ambiguity function surface

The ambiguity functions of two unmodulated sinusoidal pulses are plotted in Figure 3.8. Both have a triangular shape on the time axis and a sinc shape on the frequency axis. The temporal

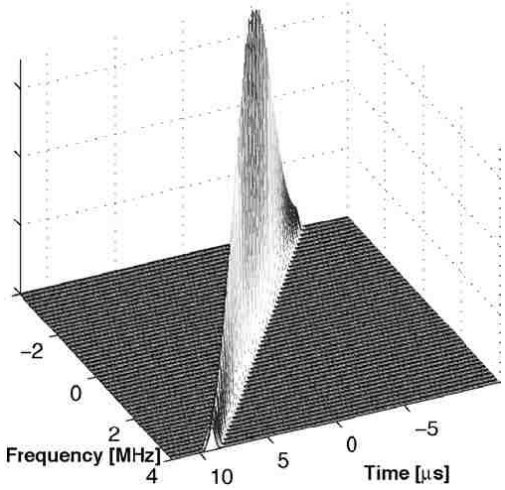

Figure 3.9: Ambiguity function of a linear FM pulse [62]

resolution is of the order of the inverse bandwidth, whereas the frequency resolution is of the order of the inverse of the duration of the pulse. From a practical point of view, this means that a long pulse offers better frequency resolution, but that a short pulse is more tolerant of shift in centre frequency.

The ambiguity function for a linear FM modulated pulse can be seen in Figure 3.9. Its orientation along the time-frequency plane nature indicates that it is relatively tolerant of frequency shift, like the short unmodulated pulse in Figure 3.8 (a). Unlike the short unmodulated pulse, a shift in frequency tends to transpose the compressed pulse in time by an amount proportional to the degree of mismatch. This might cause some geometric distortion in imaging but should not affect the accuracy of velocity estimation as, although the effects of propagation through living tissue are difficult to predict or estimate, they remain relatively constant with depth for a given target.

Figure 3.10 shows the ambiguity functions for two typical binary sequences. Both have the thumbtack shape typical of PN (pseudo-noise) sequences. Codes of this nature offer good resolution in time and in frequency shift, but no compression occurs if the frequency mismatch f_d exceeds $\frac{1}{T_b}$, where T_b is the chip period.

In [62], the Golay sequence provided a greater gain in SNR than either linear or non-linear FM signals in an initial series of simulations without frequency-dependent attenuation. Subsequent simulations included the effects of frequency-dependent attenuation, which leads to a varying depth-dependent frequency shift in the ultrasonic reflections and a resultant mismatch in the

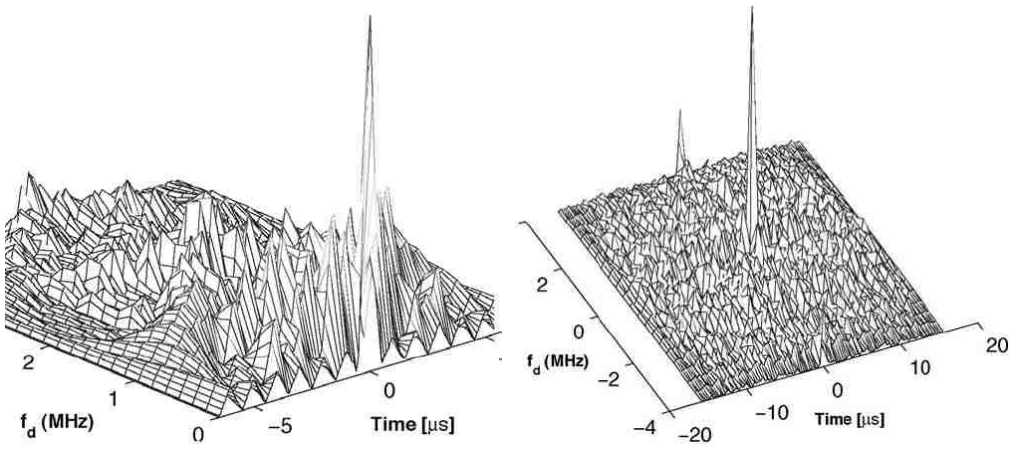

(a) Barker Sequence – 13 bit (b) M-Sequence – 64 bit

Figure 3.10: Ambiguity functions of typical binary sequences [62]

demodulation filter. In these, linear FM modulation provided greater gains in SNR than either non-linear FM or the Golay sequences, particularly at the greater depths at which gains are most required.

On this basis, and also taking the ambiguity function analysis into account, the authors conclude that the linear FM pulse is the most suitable for medical ultrasound. With regard to the first of these considerations, the methods employed to generate the Golay and NLFM signals appear to have been sub-optimal resulting in slightly skewed results. The results reported in [39] suggest that significant improvements in NLFM filter performance are achievable using a spectrum inversion approach to NLFM signal design. The Golay encoded pulses appear to have used a sinusoidal "chip" for the transmitted signals and matched filter. The sharp phase transitions this entails contain significant amounts of energy at high frequencies which would be severely attenuated during propagation and may be responsible for the poor Golay performance reported in the presence of attenuation.

The observations made in [62] regarding the ambiguity functions of LFM pulses and their resilience to frequency shift are perhaps more relevant in radar applications. The frequency mismatch of $\frac{1}{T_b}$ at which complete loss of BPC compression occurs is rather high in proportion to the Doppler shifts likely to occur. In a system with a pulse centre frequency of 5 MHz using a two-cycle sinusoidal chip, for example, this frequency would be 2.5 MHz. Given that the frequency shift due to Doppler may be expressed as $f_d = \frac{v}{c} f_c$, this would equate to a velocity of $\frac{c}{2}$, or approximately 800 m/s. Tissue velocities encountered in diagnostic imaging are typically

much lower. Results compiled from observations of ten healthy subjects published in [82] report maximum tissue velocities of below 10 mm/s associated with superficial breathing, while measured blood flow velocities in the carotid artery during exercise are in the region of 0.7 to 1 m/s [42]. The slight Doppler shifts associated with these motions will be obscured by the effects of attenuation on the signal spectrum, negating the value of any Doppler tolerance inherent to the linear FM waveform. Attenuation causes a downward shift the spectral centroid of echoes that increases steadily with depth, but doesn't affect the modulation frequency of BPC signals as Doppler would. This topic is discussed further with reference to simulation results in Chapter 4.

A detailed comparison of LFM and Golay-coded excitation signals for use in ultrasonic imaging may be found in [19]. The effects of frequency-dependent attenuation and non-linearity on side-lobe levels and SNR are considered, as are those of tissue motion. The results presented are comparable for the two waveforms. The Golay-coded pair provides a higher coding gain than an LFM signal of similar length, as the effective length of a complementary code set is the sum of lengths of the individual codes [56], although it is noted that motion can introduce severe side-lobe artefacts.

3.3.5 Velocity Estimation using Coded Excitation

In the course of this research, relatively little literature has come to this author's attention on the adaptation of velocity estimation techniques to exploit the characteristics of pulse-compression waveforms. An early effort was the pseudo-random Doppler flow-meter, proposed in [91] and further developed in [17], which was a modification of a conventional CW Doppler flow-meter. Like a conventional Doppler flow-meter, this system used separate transmit and receive electrodes but transmitted a sine wave phase-modulated by a pseudo-random binary sequence. Received reflections were filtered with a delayed subsection of the modulating sequence. This arrangement allowed a depth range of interest to be selected by adjusting the length of the filter sequence and its delay relative to the modulation sequence. Wilhjelm and Pedersen published a pair of papers [93, 94] in 1993 in which they describe a velocity estimation system using FM chirp signals. They discuss two different methods of velocity estimation: the first is a phase-shift estimation method equivalent to the 1-D auto-correlator and is affected by the confusion between Doppler-shift and range-depth due to the chirp's ridge-shaped ambiguity function; the second is based on the cross-correlation of the spectra of the receive-filter outputs, which they

describe as being equivalent to RF cross-correlation in a conventional PW-Doppler system, and isn't affected by this issue. A later paper by the same authors [95] compares an improved version of this latter method to conventional PW-Doppler, concluding that the results it provides are comparable but inferior. Chiao et. al. [18] describe significant increases in resolution and dynamic range using a technique they call B-flow imaging, but this is essentially a standard colour-flow system using coded excitation. The novelty lies in using the same pulses for B-mode imaging and blood-flow velocity estimation: the long coded pulses provide sufficient GSNR for blood-flow velocity estimation, while compression filtering allows the same pulses to be used for B-mode imaging while providing an increase in dynamic range. In his PhD thesis [38], Yonael Gorfu mentions an interesting approach to velocity estimation based on the side-lobe cancellation properties of the Golay code. This remained undeveloped in the course of his own research.

3.4 Conclusions

A wide range of coded signals have been explored in the diagnostic imaging literature. Gains in SNR and imaging depth have been reported using both discrete-phase and continuous-phase (FM) modulated signals. Compression filters for BPC signals consist of a small number of ± 1-valued coefficients separated by zeros and may be implemented as a small number of additions and subtractions, reducing the computational cost of filtering significantly. The inverse "spiking" filters mentioned in Section 3.3 introduce non-unity filter coefficients, but the majority of the coefficients remain zero-valued. Complementary BPC signals combine these benefits with ideal side-lobe characteristics without the need for "spiking" filters, although some authors have reported issues with complementary side-lobe cancellation in the presence of motion and attenuation.

A range of FM, BPC and complementary BPC signals are compared under simulated and experimental conditions in Chapter 4. The conclusions reached in relation to the sensitivity of complementary-coded signals to the effects of attenuation are contrary to those published in [62]. This disparity is explained in terms of the bandwidth characteristics of the signals and an apparent aliasing issue with the simulator. The effects of motion on complementary-coded imaging are discussed in detail in Chapter 5

Chapter 4
Coded Waveform Imaging Performance

4.1 Introduction

In this Chapter, a representative range of the coded waveforms originally described in Chapter 3 are evaluated by simulation using MATLAB and the Field II ultrasound simulation tool [32]. Some of the simulation results have also been verified experimentally in collaboration with research partners in the BIAS (Biologically Inspired Acoustic Systems) Consortium.

Sections 4.2 and 4.3 describe the simulation environment and experimental apparatus employed for the research. The parameters and design methods used to generate the signals and filters used in both simulation and experiment are described in Section 4.4. The simulation results presented, in Section 4.5, are divided into two broad categories: results obtained in idealised circumstances with no frequency-dependent attenuation and attendant signal distortion are discussed in Section 4.5.1; the second category, presented in Section 4.5.2, encompasses results which include the effects of attenuation. The measure of axial resolution employed throughout is the -6dB main-lobe width expressed in terms of $\lambda_t = \frac{c}{B_t}$, where c is the average speed of sound in tissue is and B_t is the -6dB bandwidth of the transducer. The results obtained from experiments are presented in Section 4.6 and some conclusions in Section 4.7.

4.2 Simulation Environment

4.2.1 Simulated Imaging System

The signal flow for the imaging system used in simulation is illustrated in Figure 4.1. The simulation results presented here all assume the use of a 192-element linear array transducer with a 7.5MHz centre frequency, a fractional bandwidth of 83.3%, an element width of 0.21 mm and a 50 μm kerf width. A Gaussian-modulated sinusoidal pulse with a 6.25 MHz bandwidth centred at 7.5 MHz was generated using MATLAB's `gausspuls()` function and passed to

the Field II simulator to be used as the electromechanical impulse response of the transducer on transmit and receive. The sampling frequency for the simulated ultrasound system was set to 150MHz, 20 times the centre frequency, as was that of the Field II simulator. This value was chosen to be an integer multiple of the transducer centre frequency in order to minimise sampling effects. The simulations which include the effects of frequency-dependent attenuation used average values of 0.5 dB/MHz/cm or 0.7 dB/MHz/cm. These values are at the lower and upper end of the range typically encountered in soft tissue [4] and are used widely the literature. All the simulated B-mode images which included the effects of attenuation used a value of 0.5 dB/MHz/cm. All of the simulations used a Hanning apodisation weighting, dynamic receive

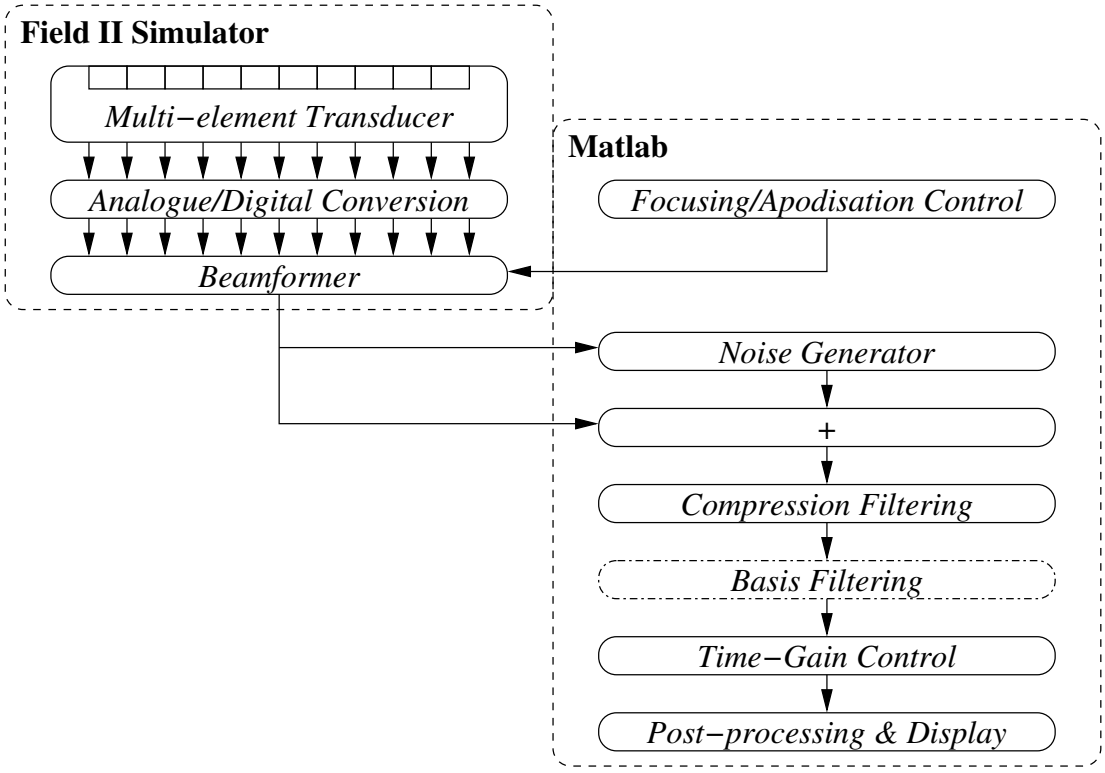

Figure 4.1: Receive signal path for the simulated coded imaging system

focusing and an F-number of 2 on transmit and receive. Three transmit focal depths were used for the B-mode imaging and motion-compensation simulations, while ten were used for the filter envelope simulations in order to minimise the impact of variation in focusing settings on the results. When comparing signals of different types, the signals were scaled to produce the same peak amplitude when convolved with the transmit impulse response of the transducer.

Gaussian white noise was added to the simulated data prior to filtering. The noise level was set relative to a reference peak received signal level obtained using a single simulated scatterer at

a depth of 5mm along the central transducer axis and a fixed focal depth of 5mm for transmit and receive.

During the course of this research, systems were simulated that used both pre- and post-compression, as described in Section 3.3. Pre-compression was implemented using S.I. Nikolov's MATLAB-based Beam-Formation Toolkit (BFT) [11], as the Field II simulator's internal beam-formation functions fail to allow for implementation of a pre-filtered system. The results obtained using pre-compression were similar to those obtained using Field II's internal beam-forming. The simulation results presented here employed post-compression using Field II's internal beam-forming routines, which are implemented in C and computationally significantly less resource-intensive than the manual implementations in MATLAB using the BFT. Log-linear time-gain control was applied to the filtered signals immediately prior to envelope detection and generation of the B-mode images. This minimised the impact of inaccuracies introduced by an additional multiplication operation and MATLAB's finite numerical accuracy.

4.2.2 Simulated Imaging Targets

Two types of phantom were used within the simulations. The first, illustrated in Figure 4.2(a), consisted of 10 simulated point scatterers positioned at 10 mm intervals between 5mm and 95mm from the transducer along its central axis and was used to compare filter envelope characteristics under a range of conditions. The second was a simulated cyst phantom and was used to compare the performance of the signal coding schemes on a more realistic imaging target. The cyst phantom, illustrated in Figure 4.2(b), was based on one of the code examples provided with Field II. It contained 8 high intensity point targets, 8 high-intensity scattering regions of increasing diameter and 8 empty regions (to simulate water-filled cysts) of decreasing diameter in a volume measuring 80mm by 25mm by 3mm and containing 300000 scatterers. This resulted in a scatterer density of approximately twelve per resolution cell, ensuring the scatter was fully developed as described in Chapter 2. The cyst phantom was situated at a distance of 20mm from the simulated transducer. In an experimental situation, a phantom of this form would not be particularly useful as the high intensity scattering regions close to the transducer would mask those further away, while the cyst targets would be likely to introduce refraction artefacts. Both would have significant effects on the average attenuation in the regions they occupy. Grouping them this way is made possible by the limitations of the simulation engine discussed in Section 2.6 and reduces simulation time considerably.

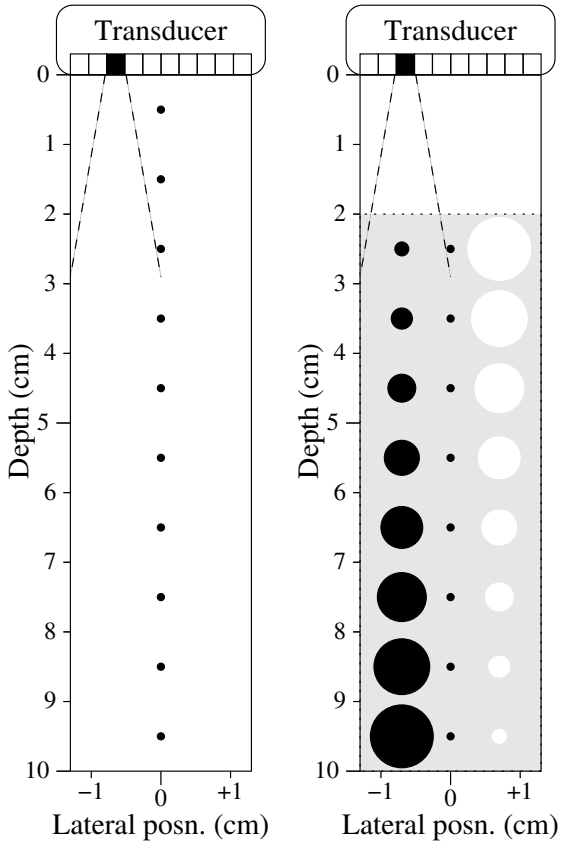

(a) Simulated Point Phantom (b) Simulated Cyst Phantom

Figure 4.2: Simulated phantoms used for coded waveform evaluation

4.3 Experimental Verification

Initial experiments were carried out using an experimental configuration developed by the British Geological Survey (BGS), Keyworth, a partner in the BIAS research consortium [23]. These used two unfocused transducers suspended in a water tank. The transducers available at this facility, designed for materials characterisation, were 9.5cm in diameter with a 120KHz centre frequency, a principal resonance peak at 100KHz and a fractional bandwidth of approximately 80%. Coded signals of 160μs and 400μs duration were compared with an uncoded sinusoid of 10μs duration during these experiments. Some results are presented in Section 4.6. Further experiments were carried out on an experimental configuration developed by members

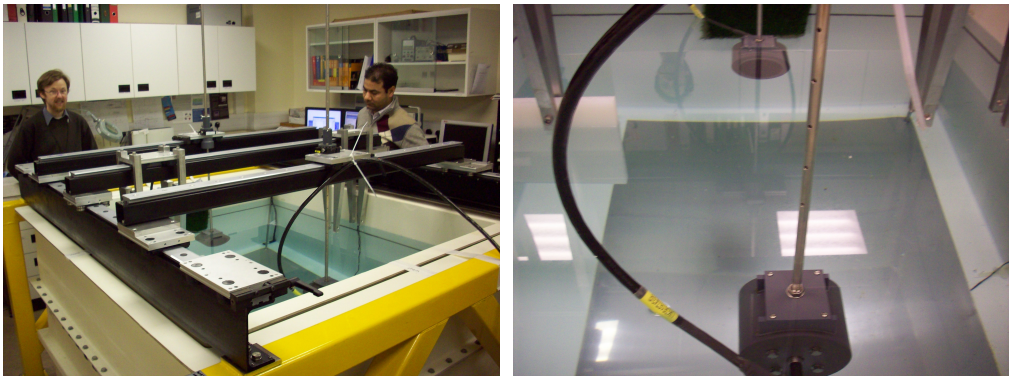

(a) Water Tank (b) Transducers

Figure 4.3: Physical properties experimental rig at the British Geological Survey, Keyworth

of Medical Physics in the Division of Medical and Radiological Sciences at the University of Edinburgh [21]. These used a single unfocused transducer with a centre frequency of 5MHz suspended in a water tank. The transducer mounting could be actuated electronically in two dimensions, while reflected signals were recorded using a data acquisition board and the LABVIEW package. Some results obtained using this facility are presented in Chapter 5 although ongoing development of the system made it impossible to obtain a complete set of results.

The experimental facilities available during the course of this research were not adequate to perform coded B-mode imaging. Both sets of experiments were used to verify fundamental results: to confirm that the performance of the various coded waveforms and filters corresponded to the simulated results when propagated through real transducers; and to confirm the viability of the motion compensation algorithm under similar conditions.

4.4 Signals and Filtering

The simulation studies, which made up the bulk of the work on which this chapter is based, focused on four signal coding schemes: a binary-phase coded complementary pulse pair; a single-cycle sinusoidal pulse; a windowed linear FM pulse with mismatched filter; and a non-linear FM pulse processed with a matched filter.

Both the linear and non-linear FM pulses used in simulations swept a bandwidth, B, of 9.4 MHz about a centre frequency, f_c, of 7.5 MHz. A pulse duration, T, of 10.7μs was chosen to match that of an 80-bit binary-phase coded signal. The resulting signals have a time-bandwidth product of 100, ensuring excellent side-lobe performance. Linear FM pulses with time-bandwidths of 16 and 40 were used during experiments. These lengths were dictated by the physical characteristics of the experimental apparatus. No experimental results are presented for the NLFM pulse. This was included in the simulation study at a later stage of the thesis research, at which point time and funding constraints prevented the conduction of additional experiments.

4.4.1 Linear FM

A constant amplitude linear FM pulse and its matched filter response are shown in Figures 4.4 (a) and 4.4 (b). In the absence of transducer effects, the matched-filter response exhibits a main-lobe width of 0.8 λ_t and near side-lobes at -13.5dB which tail off to about -40dB near the edges of the response. Convolution with the electromechanical transmit-receive response of the transducer reduces the near side-lobes to about -34 dB and increases the distant side-lobe levels to about -38 dB while increasing the width of the main-lobe to 1.2 λ_t.

In [64], matched filter coefficients are weighted with an appropriate window in to further reduce near side-lobe levels and time-domain amplitude-tapering is used at the beginning and end of the signal to reduce the levels of distant side-lobes associated with ripples in the signal spectrum without reducing the power of the transmitted signal excessively. These are known as Fresnel ripples as they are associated with the two Fresnel integrals that appear in the Fourier transform of an LFM signal. The magnitude of these ripples varies in inverse proportion the time-bandwidth product of the signal. The method used to generate the linear FM signals and weighted matched filters used in simulation follows that described in [64]. The LFM pulse used in simulation may be seen in Figure 4.4 (c). It was obtained by weighting a constant amplitude

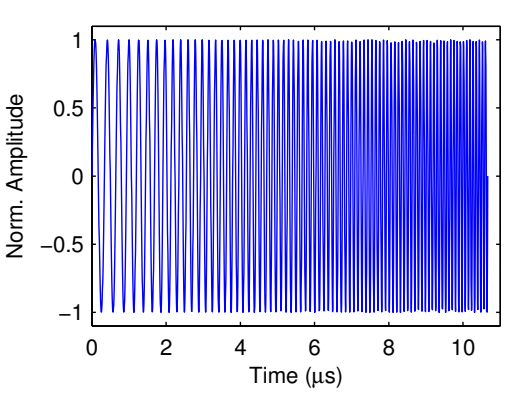

(a) LFM signal

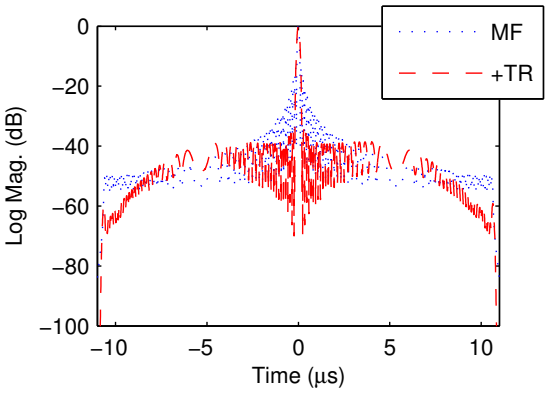

(b) LFM matched filter response

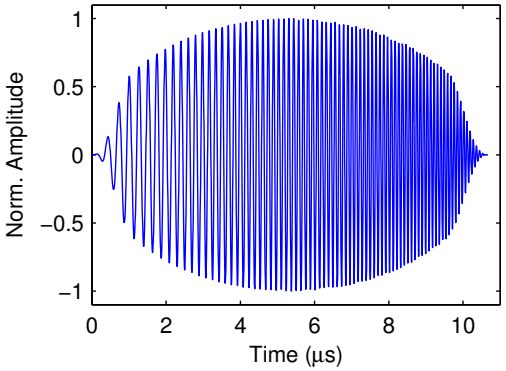

(c) Tapered LFM signal

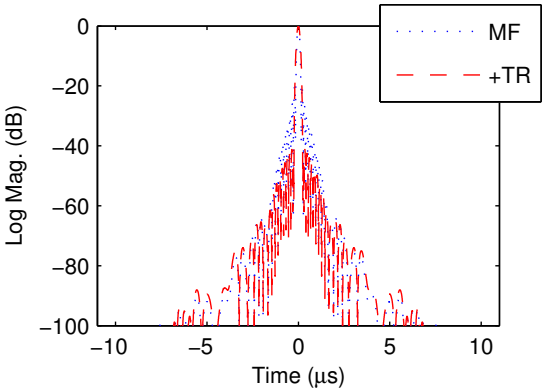

(d) Tapered LFM matched filter response

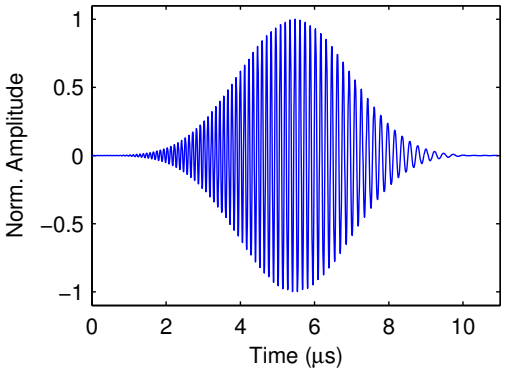

(e) Tapered LFM mismatched filter

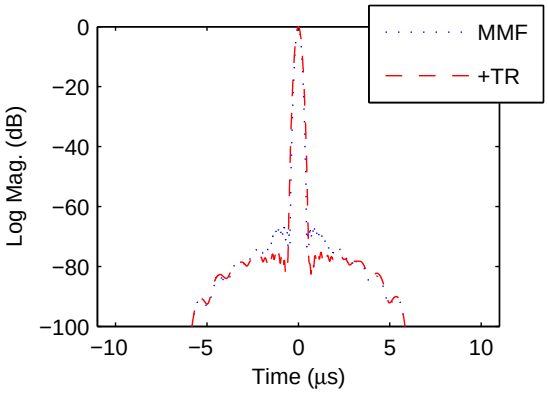

(f) Tapered LFM mismatched filter response

Figure 4.4: Constant-amplitude and amplitude-tapered LFM signals and matched filter (MF) response envelopes, and Dolph-Chebyshev weighted mismatched filter (MMF) and filter response envelopes, without and with (+TR) the effects of the transducer

LFM pulse with the modified Elliptical-Tukey window of Equation (4.1).

$$W_{\text{ET}}(n) = \ldots$$
$$\begin{cases} \frac{\sqrt{1-x^2}}{2}\left[1+\cos\left(4\pi\left(\frac{nN}{N-1}-\frac{1}{4}\right)\right)\right] & 0 \leq n \leq a \\ \sqrt{1-x^2} & a < n < b \\ \frac{\sqrt{1-x^2}}{2}\left[1+\cos\left(4\pi\left(\frac{nN}{N-1}-\frac{3}{4}\right)\right)\right] & b \leq n < N \end{cases} \tag{4.1}$$

Where

$$a = \lfloor (N-1)R \rfloor + 1 \tag{4.2}$$
$$b = N - a + 1 \tag{4.3}$$
$$x = -1 + \frac{2n}{N-1} \tag{4.4}$$

and the "$\lfloor\rfloor$" brackets represent rounding down to the nearest integer, i.e. the `floor()` function. The Elliptical-Tukey window was originally proposed in [75] and reduces side-lobe levels further than the Tukey window proposed in [64] at the expense of a less than 10% increase in main-lobe width. A window factor (denoted by R in Equation (4.2)) of 0.2 was used. The matched filter response for the signal may be seen in Figure 4.4 (d). Comparing Figure 4.4 (d) with Figure 4.4 (b), it is evident that amplitude tapering has reduced distant side-lobe levels considerably, although near side-lobe levels remain unacceptably high for imaging purposes. Neglecting transducer effects, the matched filter envelope has a -6dB resolution of 1.1 λ_t and peak side-lobes at -20dB. Convolution with the bidirectional transducer response reduces the peak matched filter side-lobes to -41dB and while increasing their main-lobe widths to 1.4 λ_t.

A filter matched to the propagated signal was obtained by time-reversal of the convolution of the LFM pulse and the transducer response. The mismatched filter shown in Figures 4.4 (e) was obtained by weighting the resulting sequence with the Dolph-Chebyshev window [26, 60] given by equation (4.5) in order to reduce distant range side-lobes.

$$W_{\text{Ch}}(n) = \frac{1}{N}\left[1 + 2S\sum_{m=1}^{M} P_{\text{Ch}}^{2M}(x_0 \cos\tfrac{m\pi}{N}) \cos\tfrac{2mn\pi}{N}\right] \tag{4.5}$$

where $N = 2M+1$; $-M \leq n \leq M$; S is a side-lobe suppression term (a value of $20\log_{10}(-90)$ was used during this work) and $P_{\text{Ch}}^{2M}(\ldots)$ is the $2M^{\text{th}}$ term of the Chebyshev polynomial defined by the equations

$$P_{\text{Ch}}^{a}(x) = \begin{cases} \cos(a\cos^{-1}x) & |x| \leq 1 \\ \cosh(a\cosh^{-1}x) & |x| > 1 \end{cases} \tag{4.6}$$

Note that Equation (4.5) is valid only for odd values of N.

Figure 4.4 (f) shows the amplitude envelope of the mismatched filter response to the signal, both with and without the effects of the bi-directional transducer impulse response. Neglecting transducer effects, the mismatched filter envelope has a -6db resolution of 1.9 λ_t and a peak side-lobe level of -67 dB. Convolution with the bidirectional transducer response reduces the peak side-lobes to -76 dB while increasing the main-lobe width 2.2 λ_t.

4.4.2 Non-linear FM

The non-linear FM signal was generated using the frequency-domain sampling method and polynomial coefficients described in [39], scaled to match the centre-frequency and bandwidth of the simulated transducer. Defining the spectrum of the desired signal as:

$$D_{\text{nl}}(f) = A_{\text{nl}}(f)e^{j\phi_{\text{nl}}(f)} \tag{4.7}$$

The desired magnitude spectrum, $A_{\text{nl}}(f)$, and phase spectrum, $\phi_{\text{nl}}(f)$, are constructed in the frequency domain and the time-domain signal is obtained by least-squares optimisation [77]. The desired magnitude spectrum, $A_{\text{nl}}(f)$ is defined as:

$$A_{\text{nl}}(f) = K(f + f_c) + K(f - f_c), \tag{4.8}$$

or, using the analytic representation,

$$\dot{A}_{\text{nl}}(f) = K(f - f_c), \tag{4.9}$$

where $K(f)$ is the Kaiser window function:

$$K(f) = \frac{I_0\left(\beta_k\sqrt{1 - [\frac{f-\frac{B}{2}}{\frac{B}{2}}]}\right)}{I_0(\beta_k)}, \tag{4.10}$$

the inverse Fourier transform of which has low side-lobes.

Here, I_0 represents the zeroth-order-modified Bessel function, B the desired signal bandwidth and β_k is a parameter that controls the main lobe width and side-lobe levels. For a desired maximum side-lobe level, α_k, β_k may be calculated as [74]:

$$\beta_k = \begin{cases} 0.1102(\alpha_k - 8.7) & \alpha_k > 50 \\ 0.5842(\alpha_k - 21)^{0.4} + 0.07886(\alpha_k - 21) & 50 \geq \alpha_k \geq 21 \\ 0 & \alpha_k < 21 \end{cases} \tag{4.11}$$

The signal energy as a function of time is:

$$E(t) = 2\int_{f_i(0)}^{f_i(t)} |A_{\text{nl}}(f)|^2 df, \tag{4.12}$$

where $f_i(t)$ is the instantaneous frequency of the signal, and the total signal energy is then:

$$E_A = 2\int_{f_i(0)}^{f_i(T)} |A_{\text{nl}}(f)|^2 df, \tag{4.13}$$

In order to use the available bandwidth efficiently, the transmitted amplitude should remain constant and the energy transmitted per unit time should be:

$$\tfrac{d}{dt}E(t) = C \tag{4.14}$$

Given that $E(0) = 0$ and $E(T) = E_A$, integrating 4.14 allows $E(t)$ to be written as:

$$E(t) = Ct + D \tag{4.15}$$

$$= \frac{E_A}{T}t, \tag{4.16}$$

where C and D are constants.

Combining (4.12) and (4.15) yields the following relationship between the desired instantaneous frequency $f_i(t)$ and the magnitude spectrum:

$$\int_{f_i(0)}^{f_i(t)} |A_{\text{nl}}(f)|^2 df = t\frac{E_A}{2T}, \tag{4.17}$$

The desired phase spectrum is defined as:

$$\phi_{\text{nl}}(f) = \arg(\mathcal{F}\{w(t)sin(2\pi\theta_i(t))\}), \qquad 0 \leq t \leq T \tag{4.18}$$

where $\mathcal{F}\{\ldots\}$ denotes the Fourier transform, $w(t)$ is a temporal weighting function and $\theta_i(t)$ is the instantaneous phase in radians, obtained by integrating the instantaneous frequency, $f_i(t)$

$$\theta_i(t) = \int_0^t f_i(\tau)d\tau, \qquad 0 \leq t \leq T \tag{4.19}$$

For a given sampling frequency, f_s, with corresponding sampling period $T_s = \frac{1}{f_s}$, the sampled version of the desired signal may be written as:

$$g_{\text{nl}}[n] = g_{\text{nl}}\left((n-1)T_s\right), \qquad 1 \leq n \leq N, \tag{4.20}$$

where $N = f_sT + 1$. The discrete version of (4.7), defined at M frequencies evenly distributed over the interval $[0, fs]$, $M \geq N$, is:

$$D_{\text{nl}}[m] = D_{\text{nl}}(f_d[m]), \qquad 1 \leq m \leq M, \tag{4.21}$$

where $f_d[m] = (m-1)\frac{f_s}{M}$.

Similarly

$$A_{\text{nl}}[m] = A_{\text{nl}}(f_d[m]) \tag{4.22}$$

$$\phi_{\text{nl}}[m] = \phi_{\text{nl}}(f_d[m]) \tag{4.23}$$

It is notationally convenient to define f_l and f_h as the upper and lower limits of the frequency range swept by the pulse such that:

$$f_l = f_c - \tfrac{B}{2} = f_i(0) \geq f_d[m_l] \tag{4.24}$$

$$f_h = f_c + \tfrac{B}{2} = f_i(T) \leq f_d[m_h] \tag{4.25}$$

where $m_l = \lfloor f_lT_sM \rfloor + 1$ and $m_h = \lceil f_hT_sM \rceil + 1$, with $\lfloor\ldots\rfloor$ and $\lceil\ldots\rceil$, respectively, representing the operations of rounding down and rounding up to the nearest integer.

Re-arranging 4.17 and combining it with (4.22) and (4.24), the time $\hat{\tau}[l]$ at which the instantaneous frequency of the pulse reaches the discrete value $f_d[m]$ is:

$$\hat{\tau}[l] = \frac{2T}{E_A} \int_{m_l}^{l+m_l-1} |A_{\text{nl}}[l + m_l - 1]|^2 df, \qquad 1 \leq l \leq L, \tag{4.26}$$

where $L = m_h - m_l + 1$.

The sequence $\hat{\tau}[l]$ may be calculated by numerical integration of 4.8. $\hat{f}_i[n]$, an estimate of the discrete version of $f_i(t)$, may then be obtained by interpolation. This was implemented using MATLAB's `interp1()` function, using the '`spline`' method. The discrete estimates of (4.19) and (4.18) are then:

$$\hat{\theta}[n] = \sum_{k=1}^{n} \hat{f}_i[k], \qquad 1 \leq n \leq N \tag{4.27}$$

$$\hat{\phi}_{\text{nl}}[m] = \arg(\mathcal{F}_M\{w[n] sin(2\pi\hat{\theta}[n])\}), \qquad 1 \leq m \leq M \tag{4.28}$$

$$\tag{4.29}$$

where $\mathcal{F}_M\{\ldots\}$ denotes the M-point discrete Fourier transform and $\arg(\mathcal{F}_M\{\ldots\})$ represents its phase component.

The desired spectrum is then:

$$\hat{D}_{\text{nl}}[m] = A_{\text{nl}}[m] e^{j\hat{\phi}_{\text{nl}}[m]} \tag{4.30}$$

The desired signal, $\hat{g}[n]$, may then be obtained using the following least-squares optimisation method. Provided $M \geq N$, $\hat{g}[n]$ is given by

$$\hat{g}[n] = \frac{1}{N} W[n, m]^H D_{\text{nl}}[m] \tag{4.31}$$

where $\hat{g}$ and D_{nl} are column matrices and W^H is the Hermitian (or conjugate) transpose of the $M \times N$ Fourier matrix with components $W_{mn} = e^{-j2\pi \frac{mn}{M}}$. Equation (4.31) is equivalent to the first N samples of:

$$\hat{g}[m] = \mathcal{F}_M^{-1}\{A_{\text{nl}}[m] e^{j\hat{\phi}_{\text{nl}}[m]}\} \tag{4.32}$$

where $\mathcal{F}_M^{-1}$ represents the M-point inverse DFT. If using MATLAB's `ifft()` function, it is important to pass it the '`symmetric`' argument. Otherwise, mild asymmetry in the sampled spectrum introduced by MATLAB's finite representational accuracy can result in severe distortions under the inverse Fourier transform, causing the function to generate a complex-valued sequence.

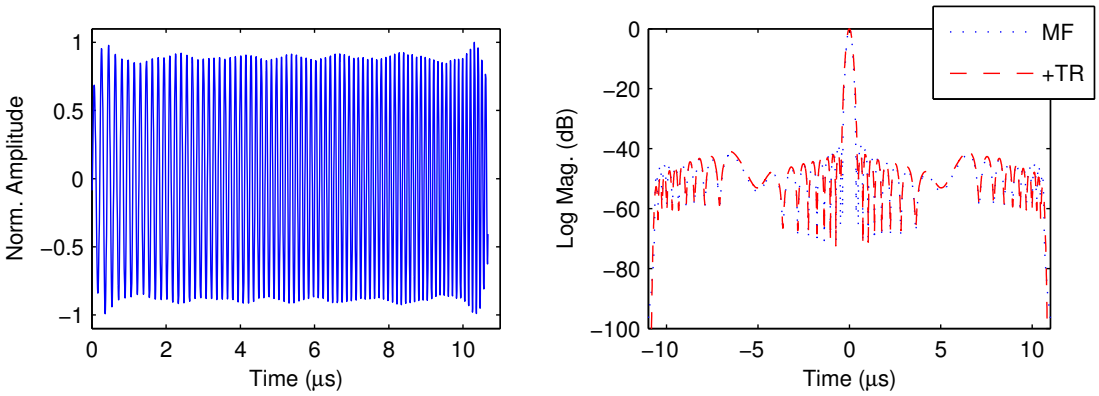

(a) Signal (b) Matched filter response

Figure 4.5: NLFM signal and filter response, with (+TR.) and without (MF) transducer response. Sampled phase spectrum - rectangular window.

Using a constant rectangular window function in (4.28) produces a signal with relatively high axial side-lobes at approximately -40dB, shown in Figure 4.5. These are due to ripple in the signal spectrum; the process of least squares optimisation minimises the error but contains no provision to minimise ripple in the amplitude spectrum of the resulting waveform.

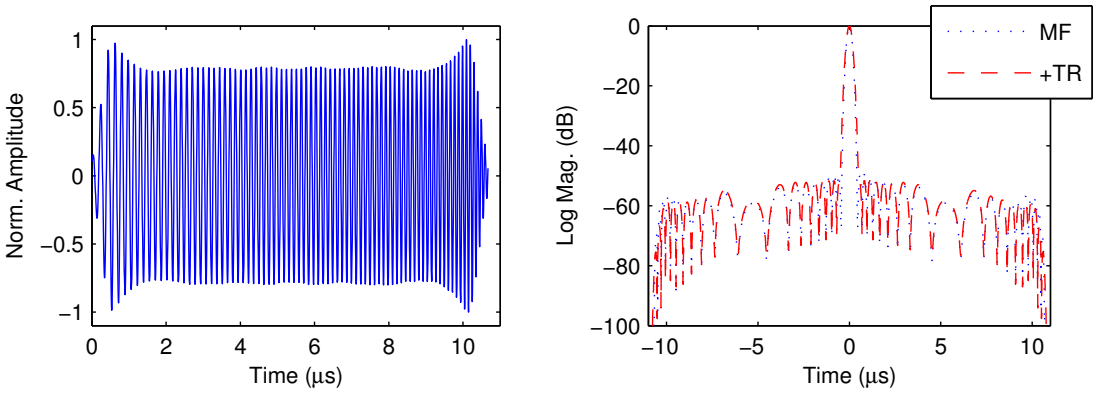

(a) Signal (b) Matched filter response

Figure 4.6: NLFM signal and filter response, with (+TR.) and without (MF) transducer response. Sampled phase spectrum - Elliptical-Tukey window

Replacing the constant rectangular window with the Elliptical-Tukey window of (4.1) reduces side-lobe levels by approximately 10dB, as shown in Figure 4.6.

Using this frequency-sampling method, the ratio of M to N has an impact on the accuracy of the numerical integration required to evaluate (4.26). At the sampling and centre frequencies used in simulation, increasing this ratio from 1 to 5, the value used to produce Figures 4.5 and 4.6, reduced peak side-lobe levels by approximately 2dB and the side-lobe levels towards the edges of the response envelope by approximately 10dB. A further increase to $M = 10N$ resulted in a negligible further improvement, of the order of 0.2 dB.

Side-lobe levels may be improved significantly by using a polynomial approximation to the sampled phase response. In [39], the third degree polynomial of (4.33) was used to generate a 20μs pulse sweeping a 5MHz bandwidth centred at 6MHz.

$$\tilde{f}_i(t) = 0.0013t^3 - 0.0391t^2 + 0.5104t + 3.5 \tag{4.33}$$

The instantaneous phase in radians is:

$$\tilde{\theta}_i(t) = \int_0^t \tilde{f}_i(t)dt \tag{4.34}$$

$$= \tfrac{1}{4}0.0013t^4 - \tfrac{1}{3}0.0391t^3 + \tfrac{1}{2}0.5104t^2 + 3.5t \tag{4.35}$$

For the current work, generalised discrete forms of (4.33) and (4.34) were derived in order to evaluate the method with a range of signal parameters:

$$\tilde{f}_i[n] = 0.00026BK_t[n]^3 - 0.00782BK_t[n]^2 + 0.10208BK_t[n] + f_l \tag{4.36}$$

$$\tilde{\theta}_i[n] = \tfrac{4}{f_c}\big(0.00026\tfrac{B}{4}K_t[n]^4 - 0.00782\tfrac{B}{3}K_t[n]^3 + 0.10208\tfrac{B}{2}K_t[n]^2 + f_lK_t[n]\big) \tag{4.37}$$

$$\tilde{\phi}_{\text{nl}}[m] = \arg(\mathcal{F}_M\{w[n]sin(2\pi\tilde{\theta}[n])\}) \tag{4.38}$$

The factor $K_t[n] = 20.025\frac{n-1}{N-1}$ is a time normalisation factor used to re-scale (4.33), which is a polynomial fit to a signal of duration 20.025 μs, to a signal of arbitrary duration measured in samples. Equation (4.37) allows the instantaneous phase to be evaluated directly, eliminating the need for frequency-domain oversampling. The signal and matched-filter response in Figure 4.7 were obtained using (4.22) and (4.37) in (4.32), using a Tukey window with a window factor of 0.1 for $w[n]$. Neglecting transducer effects, the matched filter envelope has a -6dB resolution of 2 λ_t and peak side-lobes at -79dB. Convolution with the bidirectional transducer response

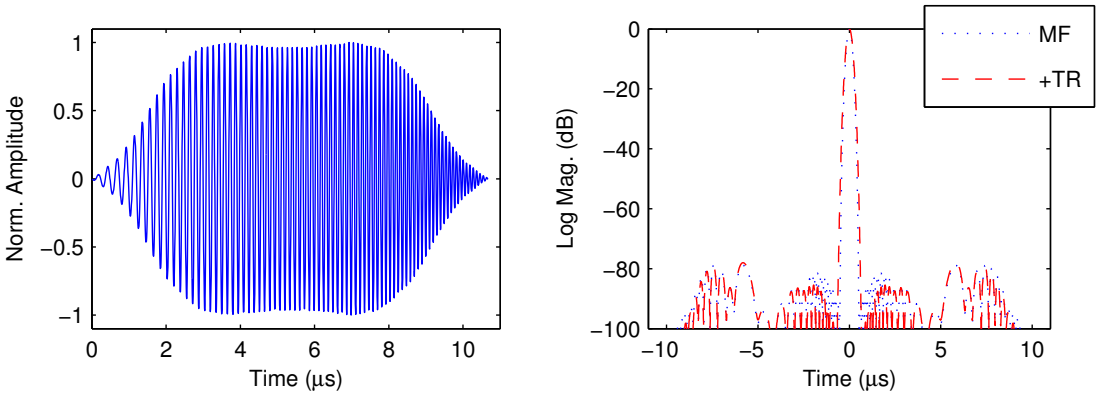

(a) Signal (b) Matched filter response

Figure 4.7: NLFM signal and filter response, with (+TR.) and without (MF) transducer response. Polynomial approximation to phase spectrum - Tukey window.

increases the peak side-lobe level to -78dB while increasing the main-lobe width to 2.2 λ_t.

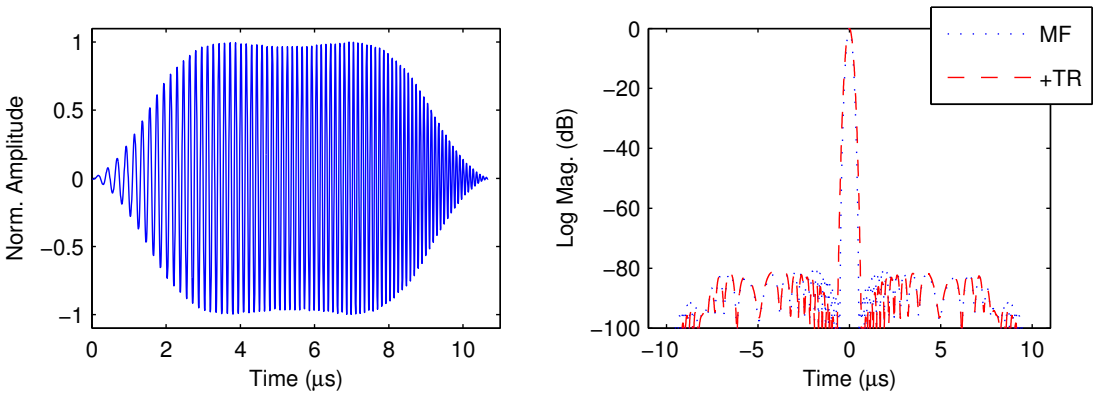

(a) Signal (b) Matched filter response

Figure 4.8: NLFM signal and filter response, with (+TR.) and without (MF) transducer response. Polynomial approximation to phase spectrum - Elliptical-Tukey window

For the signal and filter response displayed in Figure 4.8, the Tukey window used in [39] was replaced with the Elliptical-Tukey window described by (4.1). This results in a more regular distribution of side-lobe energy, as is evident from a comparison of Figures 4.7(b) and 4.8(b). This was the NLFM signal used in simulations. Neglecting transducer effects, the matched filter envelope has a -6dB resolution of 2 λ_t and peak side-lobes at -80dB. Convolution with the bidirectional transducer response reduces the peak side-lobe level to -81dB while increasing the main-lobe width to 2.2 λ_t.

4.4.3 Discrete-Phase Coded and Uncoded signals

The complementary-coded signal pairs used in simulations were generated by using the 40- and 80-bit Golay code pairs of Table 4.1in Equation (3.37).

Length	Code Pair
16	C950
	C65F
40	6B 9AE7 E606
	94 5AE8 1A06
80	6B9A E6BA 517E 5F98 19F9
	6BA5 16B9 AE7E 6068 1A06

Table 4.1: Golay code pairs used in simulation

The "chip" or basis function used was of the form of (4.39) to ensure the spectrum of the transmitted signal was largely dictated by the frequency response of the transducer. The duration of the chip was $T_b = \frac{1}{f_c}$, where f_c is the transducer centre frequency. At a centre frequency of 7.5 MHz, the 40-bit and 80-bit code pairs produced coded signals of duration 5.3 μs and 10.7 μs respectively. A single instance of the chip was also used as the uncoded pulse in simulations.

$$b_{\text{imp}}(t) = \delta(t) - \delta(t - \tfrac{1}{2}T_b) \tag{4.39}$$

or, in discrete form:

$$b_{\text{imp}}[n] = \delta[n] - \delta[n - \tfrac{1}{2}T_b f_s], \tag{4.40}$$

provided that f_s is chosen as an even multiple of f_c.

A single instance of the chip is shown in Figure 4.9(a), both with and without the effects of the transducer. Convolution with the transducer response does not affect complementary side-lobe cancellation, as illustrated in Figure 4.10. The 80-bit Golay pulse pair was used for the filter envelope results reported in this Chapter in order to prevent differences in signal length from biasing the comparison of FM and Golay performance in the presence of attenuation. The 40-bit pulse pair was used for the motion-compensated simulations reported in Chapter 5, as longer signals can reduce the efficacy of motion compensation in the presence of the inhomogeneous motion described in Section 5.4 and a complementary-coded signal pair provides the coding gain of single-transmit signal of the same bandwidth and twice the length. The simulated complementary-coded B-mode images in this Chapter and in Chapter 5 were all generated using the 40-bit pulse pair.

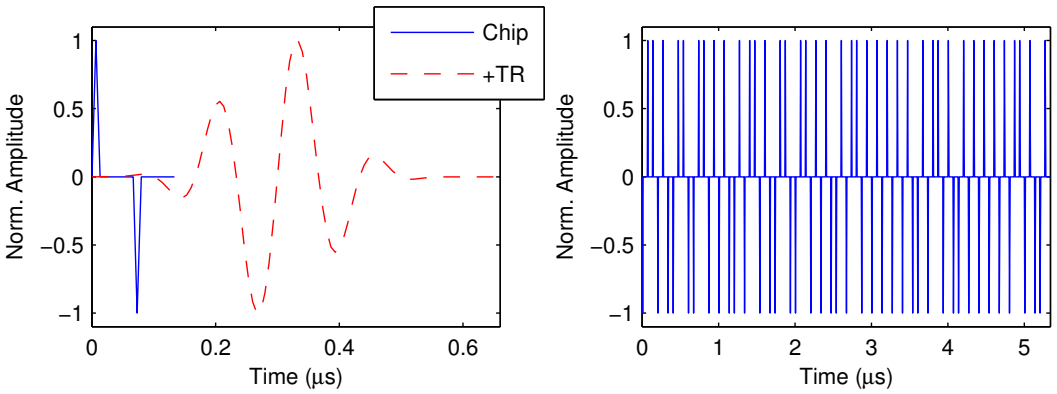

(a) Chip (b) 40-bit Golay coded pulse

Figure 4.9: Chip and Golay-coded pulse. The chip is shown with and without the effects of low-pass filtering (LPF) and the transducer (TR)

The Golay code pairs of lengths 16 and 40 were used to generate signals for use in experiments. At a centre frequency of 5 MHz, these produced coded signals of 3.2μs and 8μs duration for use in the experiments conducted at the Department of Medical Physics. The uncoded pulse was of length 0.2μs, neglecting any increase due to the length of the transducer impulse response.

Filtering for the binary-phase coded pulses was divided into two stages, as described in Chapter 3. In the first, signals were passed through a *compression filter* matched to the modulation sequence as described in Sections 4.2.1 and 3.2.2. Complementary filter outputs were added together and their sum passed through a *basis filter* – a band-pass filter matched to the basis sequence and transducer. The results presented throughout this chapter used a basis filter obtained by convolving a single instance of the chip of (4.40) with a filter matched to the pass-band of the transducer. The same filter was used to process the uncoded sinusoidal pulse.

4.4.4 Signal Spectra

The magnitude spectra of the linear and non-linear FM pulses used in simulations may be seen in Figure 4.11, while those of a single Golay-coded pulse and the sum of compression-filtered Golay pulses may be seen in Figure 4.12. These have been shown with and without the effects of the bi-directional transducer response.

The spectra of the FM signals are band-limited and thus unaffected by the Field II aliasing issue mentioned in Section 2.6, whereas those of the discrete-phase coded signals contain significant amounts of energy at high-frequencies.

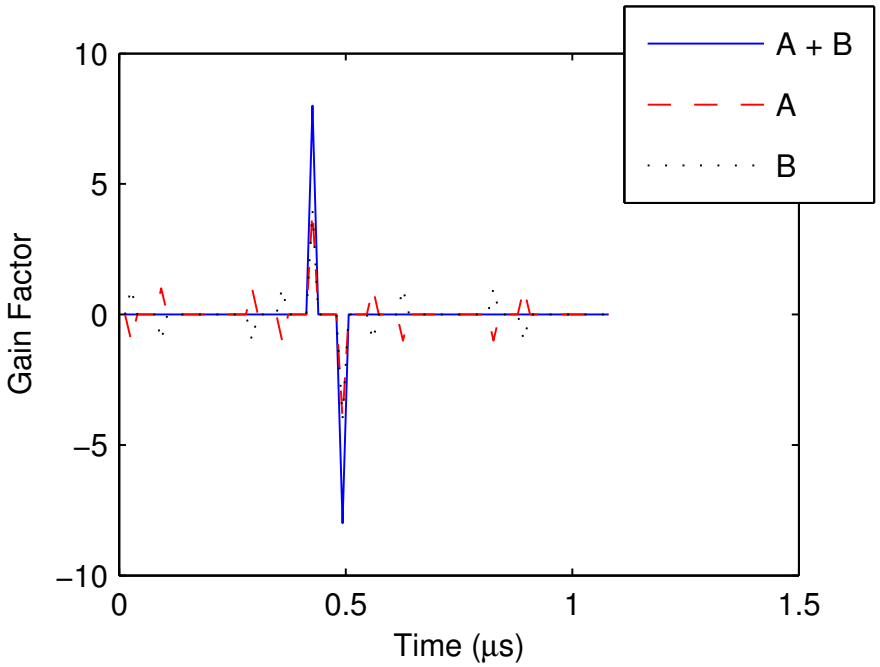

(a) No transducer effects

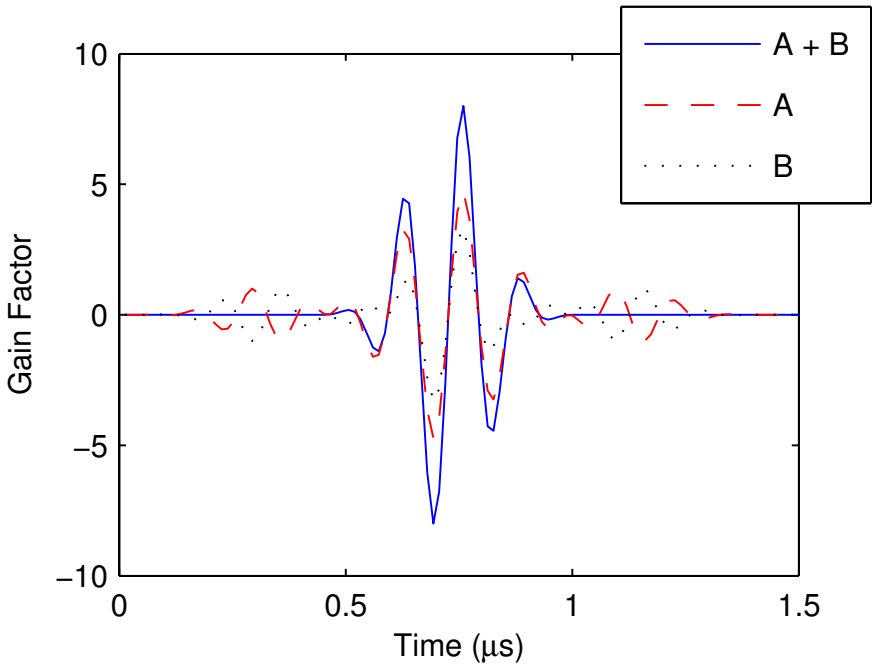

(b) Including bi-directional transducer response

Figure 4.10: Effect of the transducer on summed compression filter outputs for a complementary pulse pair generated using a 4-bit binary code and impulsive chip.

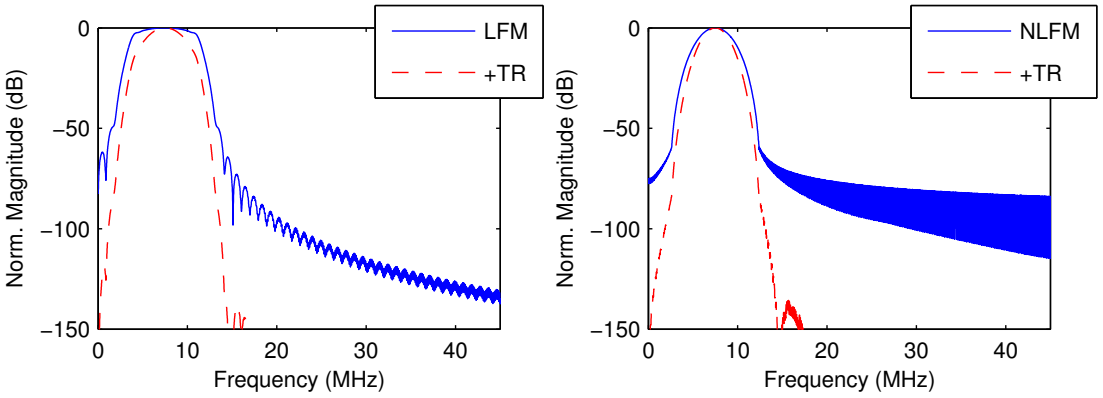

(a) Linear FM (b) Non-linear FM

Figure 4.11: Magnitude spectra of FM signals used in simulation, both with and without the effects of the transducer (TR)

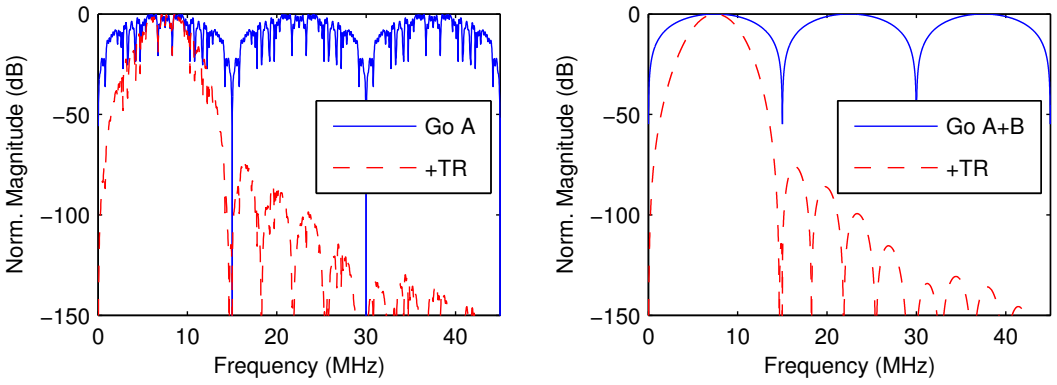

(a) Un-compressed Golay pulse (b) Sum of compressed Golay pulses

Figure 4.12: Magnitude spectra of binary-phase coded signals before and after compression, both with and without the effects of the transducer (TR)

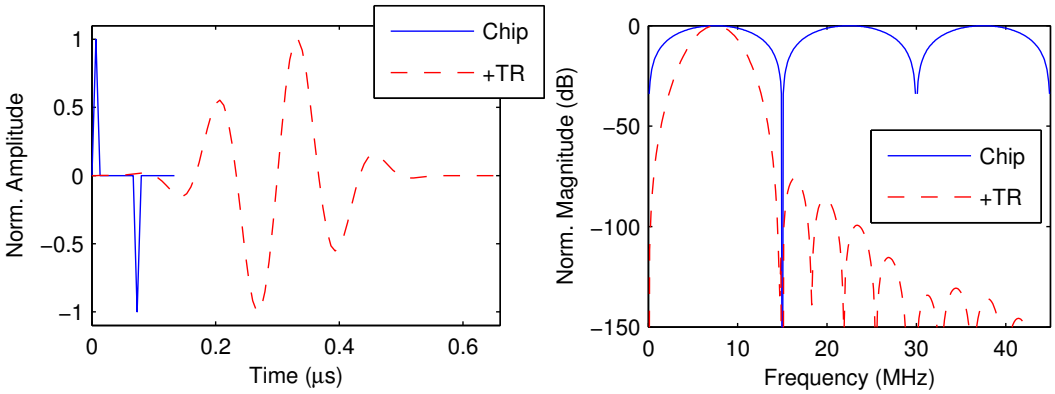

(a) Impulsive - chip

(b) Impulsive - spectrum

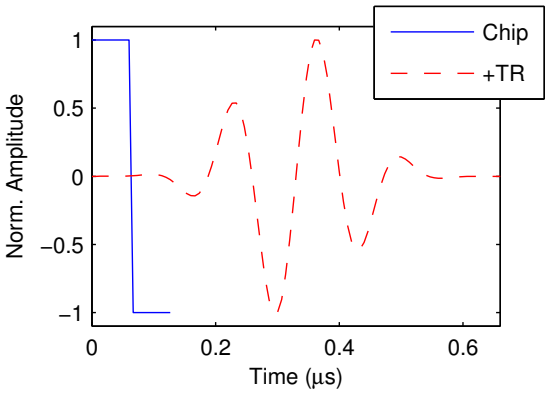

(c) Square wave - chip

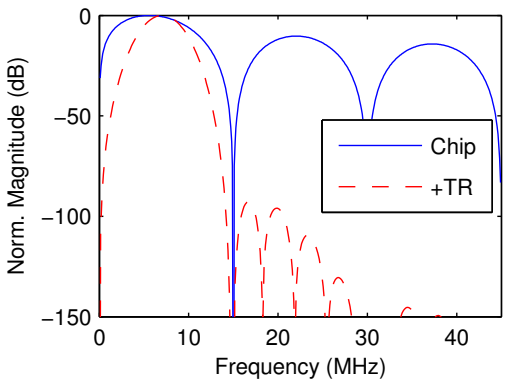

(d) Square wave - spectrum

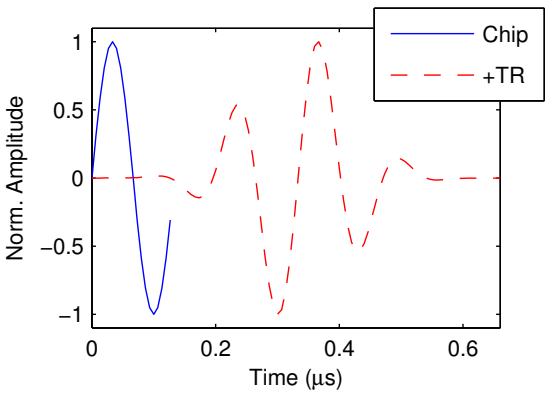

(e) Sinusoidal - chip

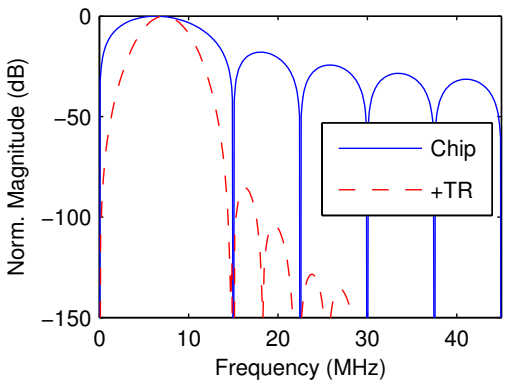

(f) Sinusoidal - spectrum

Figure 4.13: Impulsive, square-wave and sinusoidal chips and their magnitude spectra, both with and without the effects of the transducer (TR)

Figure 4.13 shows normalised time- and frequency-domain representations of the impulsive chip used in simulations and of square-wave and sinusoidal chips, with and without the effects of the bi-directional transducer response. Comparing Figure 4.13(b) with Figure 4.12, it is evident that, prior to propagation, the magnitude spectra of the raw Golay-coded sequences are largely determined by that of the chip used to generate them. After convolution with the transducer response, all three chips are very similar in both the time and the frequency domains. For discrete-phase coded sequences, the choice of chip plays a comparatively minor role in determining the shape of the transmitted pulse, provided it has a strong frequency component at f_c. The spectrum of the transmitted signal is largely determined by the transducer impulse response and its time-response by the phase code sequence used to generate it.

4.5 Simulation Results

4.5.1 No Attenuation

Figures 4.14 (a) and 4.14 (b) show filtered pulse reflections from simulated point scatterers located 5mm and 95mm from the transducer. It is evident from a comparison of the two figures that, in the absence of attenuation, neither Golay, LFM nor NLFM filter envelope characteristics are adversely affected by increasing depth, although variations in scatterer position in relation to the transmit focus and in apodisation settings between focal zones result in a slight depth-dependent variation in peak signal levels for all three types of excitation pulse. Complementary side-lobes have cancelled completely in the combined envelope of the Golay-coded signal pair, and both it and the uncoded single-cycle pulse have a mean -6dB main-lobe width of $1.4\lambda_t$. The LFM filter output exhibits a mean maximum side-lobe level of -75dB, while the mean maximum side-lobe level of the NLFM pulse is -79dB. Both LFM and NLFM pulses exhibit a -6dB main-lobe width of 2.2 λ_t. Images of the simulated cyst phantom obtained using the 5.3μs Golay pulse pair and the 10.7μs linear FM and non-linear FM imaging pulses can be seen in Figure 4.15, along with a reference image obtained using a single-cycle sinusoidal pulse. In the absence of attenuation and noise, the results obtained using the Golay-encoded pulse pair are indistinguishable from the sinusoidal results. The images obtained using linear and non-linear FM pulses are also very similar to one another. The reduced axial resolution of the FM pulses is discernible from the point targets along the central image lines.

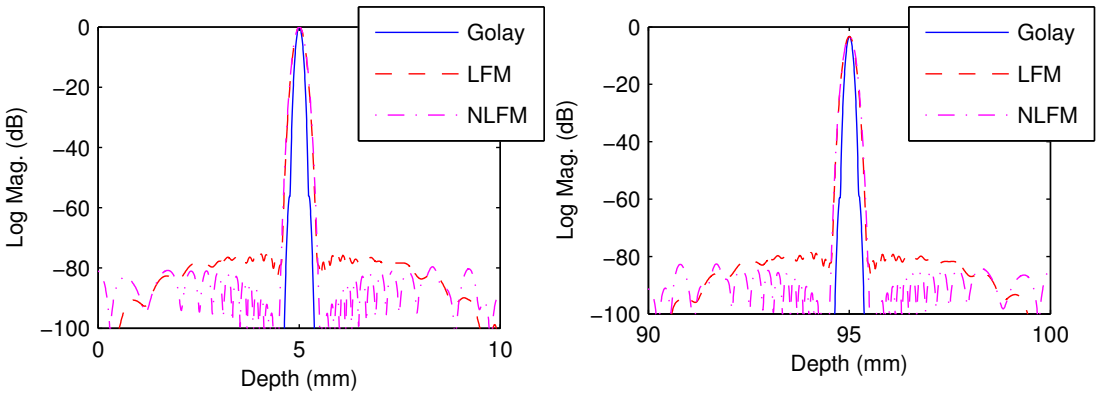

(a) Filter envelopes - 5mm

(b) Filter envelopes - 95mm

Figure 4.14: LFM, NLFM and Golay pulses reflected from 5mm and 95mm and corresponding filter response envelopes. No attenuation

4.5.2 Effects of Attenuation

The introduction of simulated frequency-dependent attenuation causes a reduction in the peak levels of the filtered signal envelopes. This has been plotted against depth in Figure 4.16 for two different levels of simulated attenuation. For the uncoded pulse and the Golay-coded pulses, which are affected identically, this reduction is entirely due to the reduction in received signal levels caused by attenuation. The effect is more severe for the FM pulses. Two principal causes can be put forward to explain this disparity. For both of the FM pulses, the spectral magnitudes of the lower frequency components least affected by attenuation have already been reduced prior to propagation by measures designed to reduce range side-lobes: by amplitude weighting of the LFM pulse and in the design of the phase spectrum of the NLFM pulse. This is illustrated by comparing Figures 4.17 (a) and 4.17 (b), which show the unfiltered reflected signal envelopes from point scatterers at depths of 5mm and 95mm under 0.5dB/MHz/cm frequency-dependent attenuation. The peak level of the reflected LFM envelope from 95mm is 2dB below that of the Golay-coded and uncoded pulses, while that of the NLFM envelope is 7dB lower. Comparing the filtered versions of these envelopes in Figures 4.17 (c) and (d)), the LFM and NLFM peaks are 12dB lower than that of the combined Golay envelope (and that of the uncoded pulse, which has been omitted for clarity). The reason for this additional reduction is that higher weight is given to the central frequency components of the FM pulses during compression. The matched and mismatched filters used to process the FM and NLFM signals pass a limited frequency band and attach most weight to the frequencies at the centre of the pulse spectrum. Using an unweighted linear FM chirp and matched filter under identical conditions, the mismatch loss

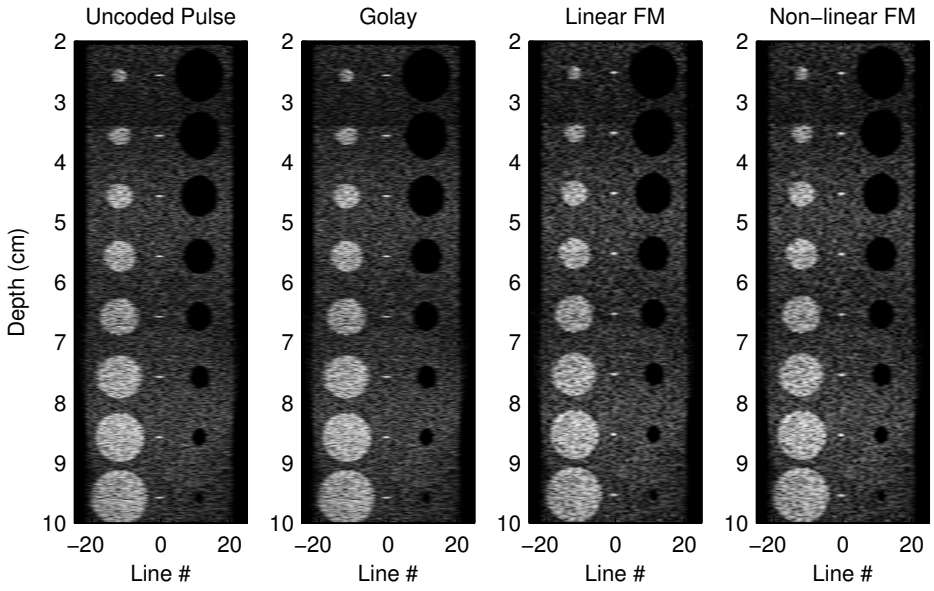

Figure 4.15: Simulated images of a cyst phantom using a range of excitation signals. No attenuation or additive noise

is of the order of 2 dB as equal weight is given to the entire range of frequencies – the high side-lobe levels (of the order of 13dB) render this signal and filter combination unsuitable for imaging purposes.

Spectrograms of reflections of Golay, LFM and NLFM pulses from simulated scatterers at depths of 5mm and 95mm may be seen in Figure 4.18. In these figures, the horizontal axis represents time, the vertical axis represents frequency and the colour represents the normalised magnitude of a particular frequency component at a point in time. An alternative explanation for the superior performance of binary-phase coded pulses under attenuation may be advanced based on their time-frequency structure and related differences in the compression process for BPC and FM pulses.

The magnitude spectrum of an FM pulse varies continuously as a function of time. As a result, so does the severity of the effects of attenuation, which distort the time-frequency nature of the pulse as is evident from the spectrograms of FM pulse reflections in Figure 4.18. FM pulse compression is accomplished by matching the filter to the instantaneous frequency, phase and magnitude of the pulse, the mismatch between signal and filter also change as a function of time, which has implications for compression performance as well as the side-lobe and resolution characteristics of the filter output.

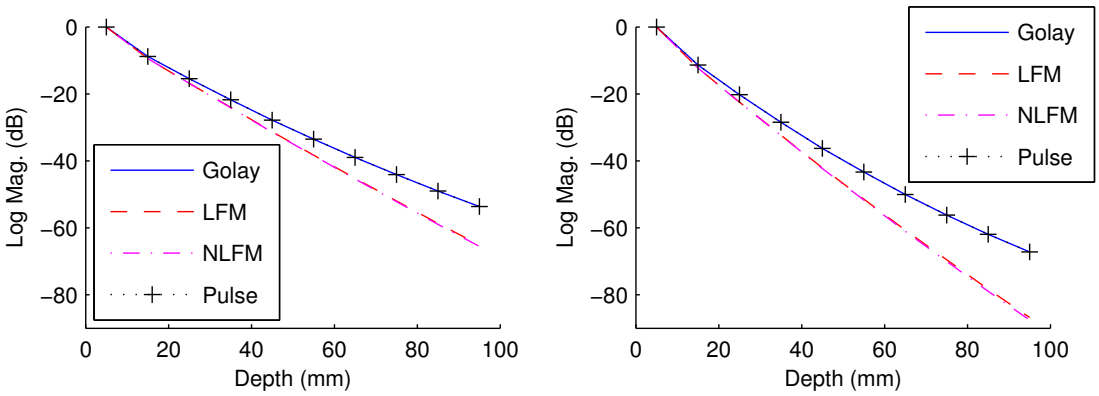

(a) 0.5 dB/MHz/cm (b) 0.7 dB/MHz/cm

Figure 4.16: Depth-dependent reduction in peak envelope levels due to attenuation

The spectrograms of reflections of an 80-bit Golay coded pulse from depths of 5mm and 95mm may be seen in Figures 4.18 (e) and 4.18 (f). The effects of attenuation result in a significant downward shift in the spectral centroid of the pulse, however this downward shift affects each symbol (or bit) of the coded sequence in an identical manner. Using discrete-phase coded signals, compression filtering requires that the phases of signal sections T_b seconds apart match the phase sequence used to generate the pulse. This process can be viewed as the addition of samples from adjacent bit-periods, phase-shifted based on the chosen code sequence. If a bi-phase code is employed, this phase-shift becomes a simple sign inversion and the two code symbols have identical magnitude spectra, so any attenuation affects both symbols in a similar manner. The phase relationships within a chip may be allowed to change arbitrarily, provided that these changes are consistent from one bit period to the next. This "transparency" appears to be a property unique to discrete bi-phase codes. If a code consisting of more than two phase symbols is adopted, the individual symbols are likely to have differences in their magnitude spectra. In the presence of frequency-dependent attenuation, each symbol will be affected differently and robustness may be compromised. The overall peak reduction due to attenuation, focusing variation and filter mismatch was estimated by comparing the peak envelope values of filtered reflections from scatterers at 15mm up to 95mm to that at 5mm for each pulse type. The results obtained using the uncoded pulse were used as an estimate of the loss due to attenuation and focusing variation and subtracted from the estimates for the coded pulse types to obtain an estimate of *mismatch loss*. The estimated FM mismatch loss has been plotted against depth in Figure 4.19 for simulated frequency-dependent attenuation of 0.5 dB/MHz/cm and 0.7 dB/MHz/cm. The Golay results coincide with the base-line sinusoidal values to within ± 0.01

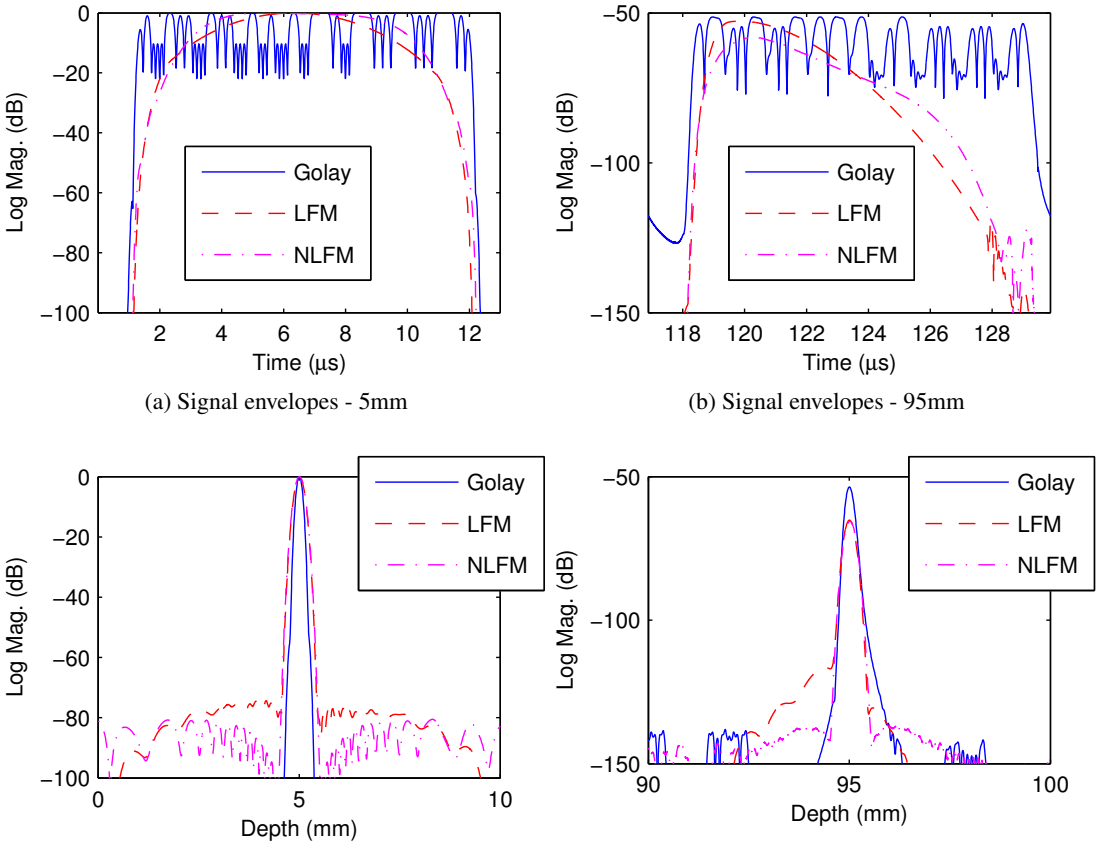

(a) Signal envelopes - 5mm

(b) Signal envelopes - 95mm

(c) Filter envelopes - 5mm

(d) Filter envelopes - 95mm

Figure 4.17: Effects of simulated attenuation on LFM, NLFM and Golay pulses reflected from 5mm and 95mm and corresponding filter response envelopes

dB and have thus been omitted for clarity.

Attenuation also has an impact on the side-lobe characteristics of the filter envelopes, as illustrated in Figure 4.20. These are negligible at a depth of 5mm, as may be seen in Figure 4.17 (c). The LFM filter envelope exhibits peak side-lobes at -74dB, while those of the NLFM filter envelope are at -80dB. At a depth of 95mm, the effects of attenuation are evident. The LFM side-lobes have increased to -51dB, whereas the NLFM side-lobes have risen to -71dB. One possible explanation for the more rapid increase of LFM side-lobe levels is that their minimisation is accomplished entirely by amplitude weighting of the signal and filter and is thus more severely affected by the amplitude distortion of the reflected pulse envelope caused by the effects of attenuation. The side-lobe structure of the NLFM pulse matched-filter response is primarily a function of the designed phase spectrum, as described in Section 4.4, and thus more resilient to the effects of attenuation.

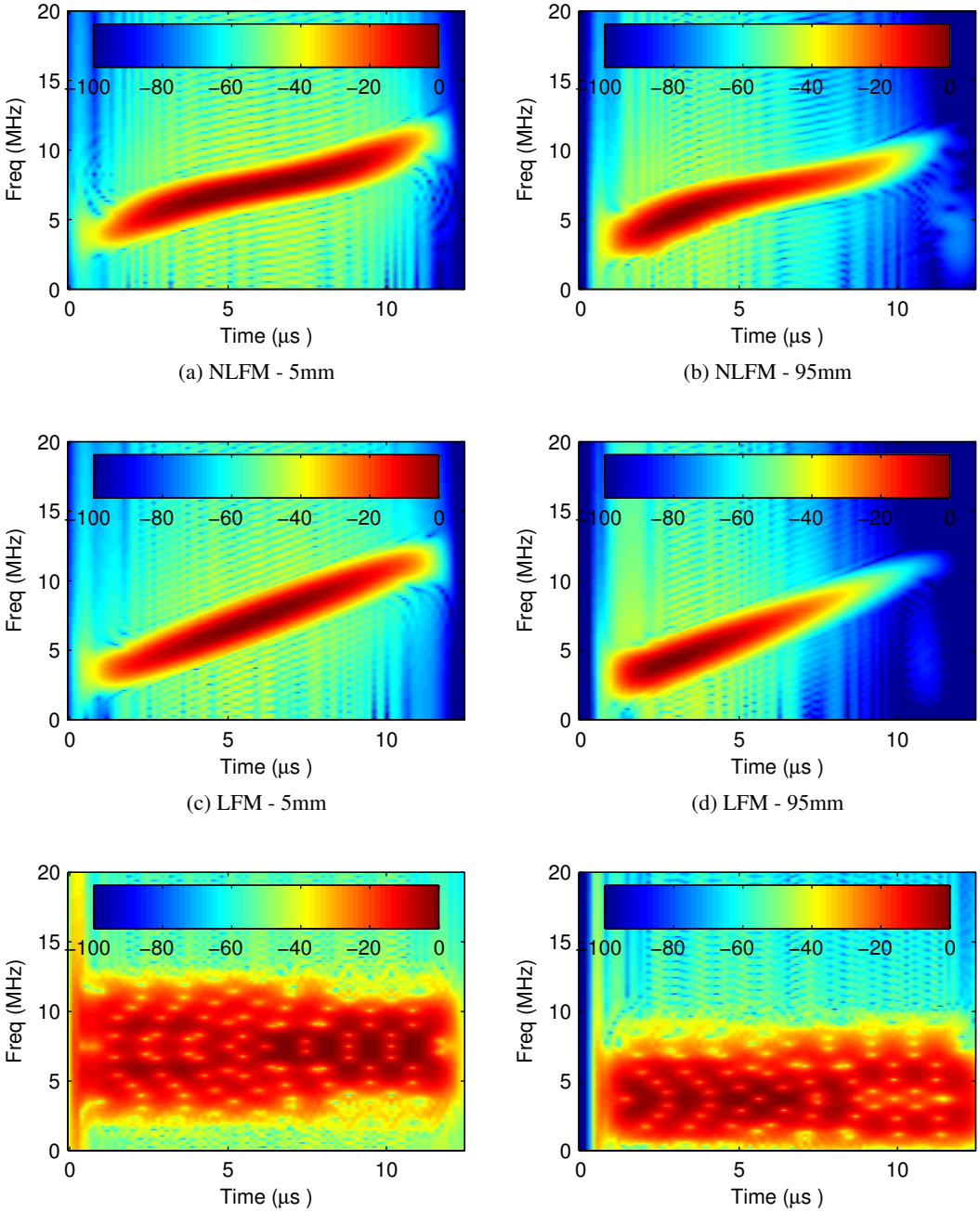

(a) NLFM - 5mm

(b) NLFM - 95mm

(c) LFM - 5mm

(d) LFM - 95mm

(e) Golay - 5mm

(f) Golay - 95mm

Figure 4.18: Time-frequency representations of LFM, NLFM and BPC pulse reflections from scatterers at 5mm and 95mm. Colour represents magnitude in dB.

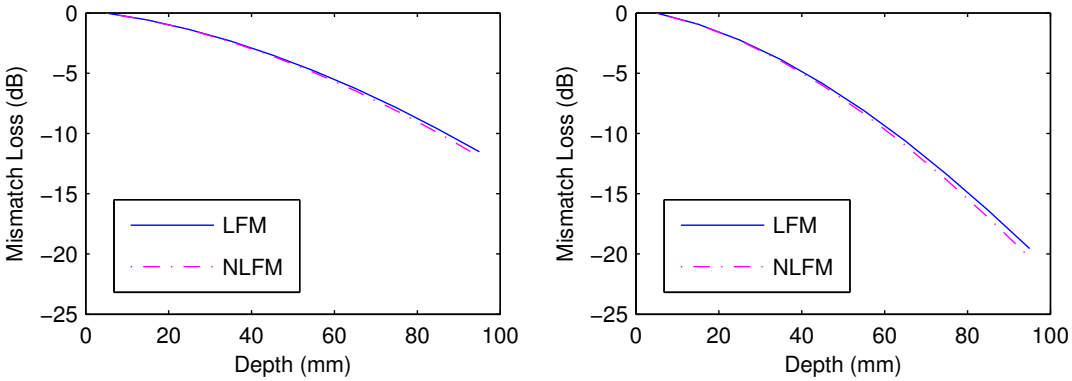

(a) 0.5 dB/MHz/cm (b) 0.7 dB/MHz/cm

Figure 4.19: Filter mismatch loss due to attenuation

Note that the side-lobes visible in the lower part of the Golay envelope in Figure 4.17(d) are the aliasing artefacts mentioned in Section 2.6, which have been reduced significantly (now occurring -140 to -150 dB below the peak filter output) but not altogether eliminated by low-pass filtering the signals prior to simulation.

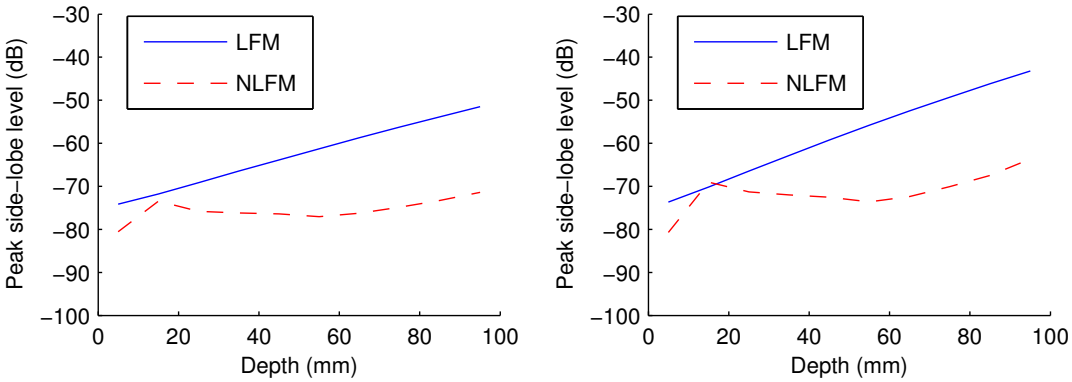

(a) 0.5 dB/MHz/cm (b) 0.7 dB/MHz/cm

Figure 4.20: Effects of attenuation and imaging depth on peak side-lobe levels

Figure 4.21 contains plots of main-lobe resolution against depth for all three coded pulse types. Under simulated attenuation of 0.5dB/MHz/cm, the -6dB widths of the main-lobes at a depth of 5mm are unchanged from the values obtained without simulated attenuation. At 95mm, the main-lobe widths of the Golay and uncoded pulse envelopes have increased by 29% to $1.8\lambda_t$; that of the LFM envelope has increased by 5% to $2.3\lambda_t$, while that of the NLFM envelope has increased by 9% to $2.4\lambda_t$. As the binary-phase Golay code filters are all-pass in nature, their

resolution characteristics are dictated by the chip and basis filter. The corresponding plots for the uncoded pulse coincide with those reproduced here for the Golay pulse pair and have again been omitted for clarity.

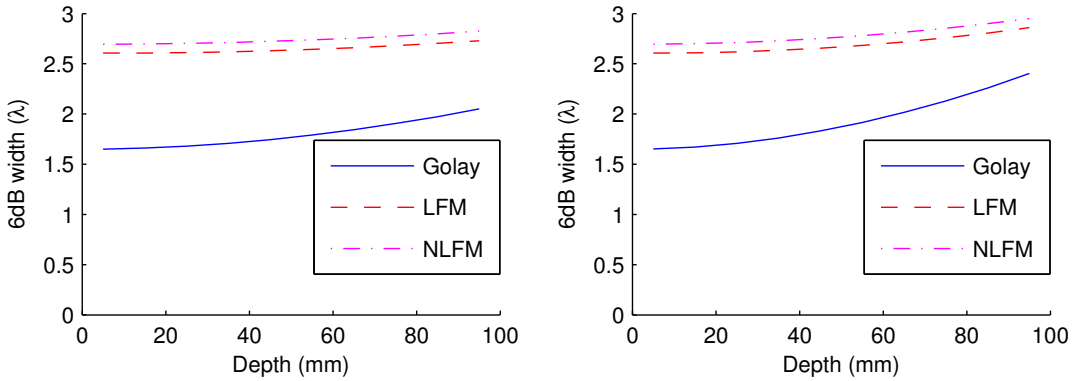

(a) 0.5 dB/MHz/cm (b) 0.7 dB/MHz/cm

Figure 4.21: Effects of attenuation and imaging depth on axial resolution

The images in Figure 4.22 offer a subjective demonstration of the benefits of coded excitation for deep imaging in an attenuating medium. In the absence of additive noise (Figure 4.22(a)), the images obtained using the uncoded pulse and the Golay pulse pair are very similar, as are those obtained using the two FM pulses. In Figure 4.22(b), the increase in SNR provided by signal coding is evident for all three images obtained using coded signals. The LFM and NLFM images are very similar, while the robustness to attenuation of the Golay coded excitation pulses translates to a clear image at greater depth.

4.6 Experimental Results

Some results obtained using the BGS experimental rig are presented in Figures 4.23 and 4.24. Figure 4.23 shows filtered data corresponding to the direct transmission path between the two transducers described in Section 4.3 for coded LFM and Golay signals of two different durations. In this experiment, the simulated LFM signals exhibited filter side-lobes at about -30dB and -49dB, respectively. The non-ideal nature of the transducers has had no adverse affect on Golay side-lobe cancellation and the envelopes of the Golay code pairs conform very closely to those of the uncoded pulses. The -6dB widths of the Golay filter envelopes are $2\lambda_t$ and $2.1\lambda_t$ and those of the LFM filter envelopes are $2.2\lambda_t$ and $2.6\lambda_t$ for the signals of duration 160 and

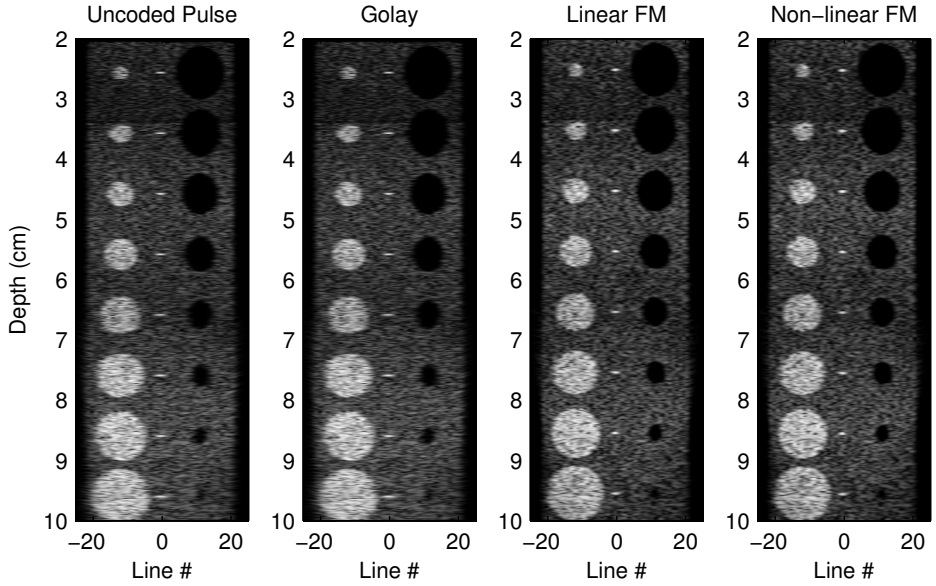

(a) 0.5 dB/MHz/cm attenuation, no noise

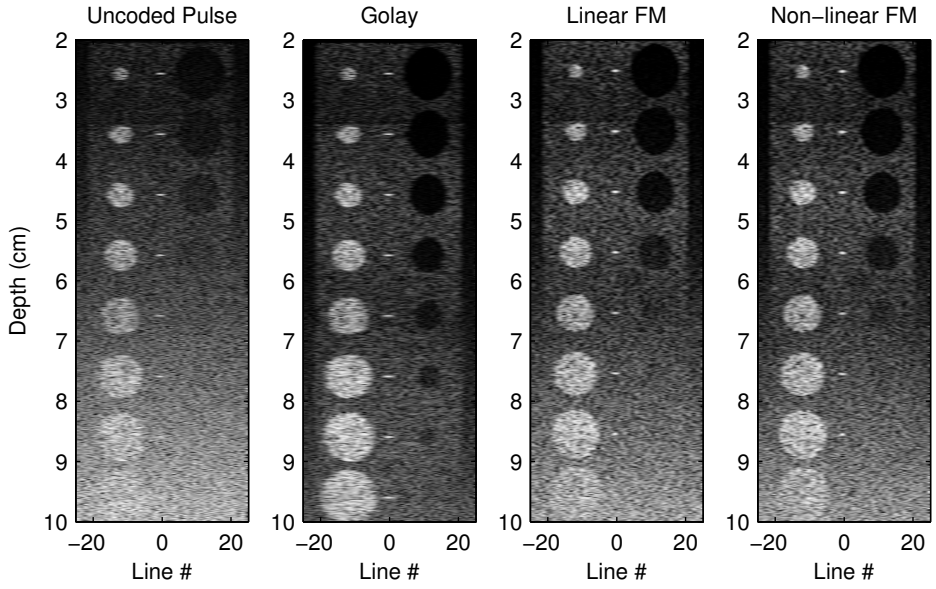

(b) 0.5 dB/MHz/cm attenuation, additive noise at -40dB

Figure 4.22: Effects of simulated frequency dependent attenuation of 0.5 dB/MHz/cm on simulated images of a cyst phantom using a range of excitation signals

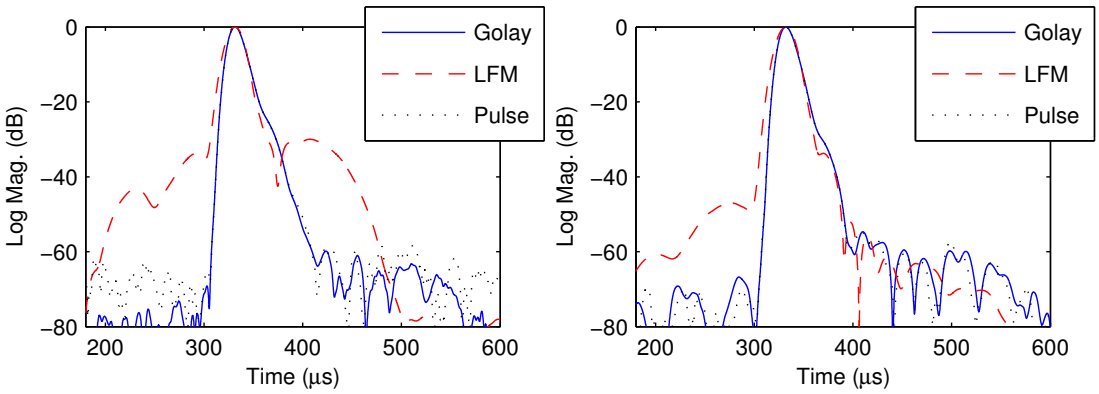

(a) 160μs pulse (b) 400μs pulse

Figure 4.23: Filter envelopes from BGS experiments using LFM and Golay coded signals

400 μs, respectively.

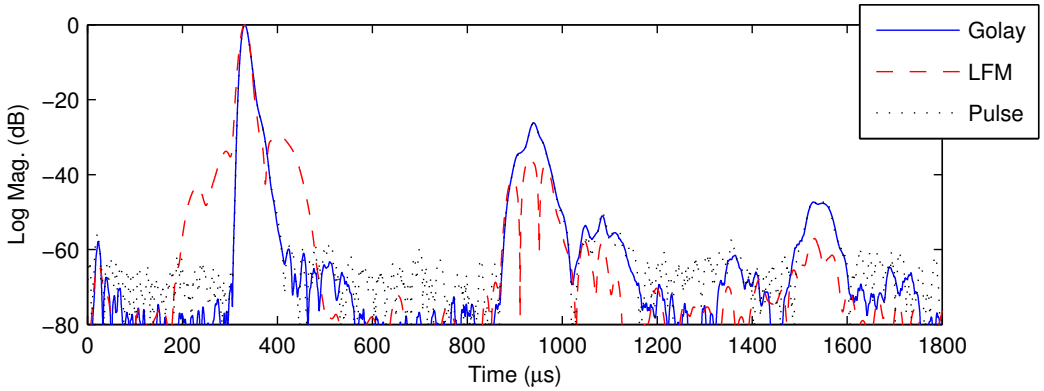

Figure 4.24: Filtered envelopes from BGS experiments including distorted primary and secondary reflections.

Figure 4.24 shows a longer section of the relevant filter outputs corresponding to an uncoded pulse, the Golay pair of length 16 and a chirp with a time-bandwidth product of 16. It is evident that Golay envelopes correspond very closely to that of the uncoded sequence, apart from the difference in their noise floors. The first prominent peak is that illustrated in Figure 4.23(a), whereas the two subsequent peaks are due to primary and secondary reflections between the faces of the two transducers. These are distorted due to the physical extent and irregular surfaces of the faces of the transducers, which were designed for materials characterisation rather than imaging purposes. It is evident from Figure 4.24 that the bi-phase Golay filters are more resilient to this distortion than the matched-filter used for the chirp signals.

4.7 Conclusions

The results presented in this chapter demonstrate some of the potential advantages conferred by complementary binary-phase codes in ultrasonic imaging. The advantages of complementary codes in terms of side-lobe performance and coding gain are well documented. In the current work, their performance has been compared to linear and non-linear FM signals under a range of conditions and novel simulation results presented demonstrating their significant advantages in attenuating media at high imaging frequencies. A hypothesis has also been presented explaining the robustness to attenuation of the larger family of binary-phase codes in terms of the time-frequency characteristics of the different pulse types and compression methods.

These conclusions differ from findings reported in [63], in which it was argued that the LFM pulse was more robust to attenuation than a Golay-coded pulse pair. This argument is based on a comparison of the ambiguity functions (in which the two axes represent time-shift and frequency-shift) of the two signal types. An assumption implicit in this analysis is that the frequency shift is due to the Doppler effect, which would stretch the bit period of the BPC pulses and cause the breakdown in compression predicted by the authors. In medical ultrasonic imaging, the Doppler shift is very low in comparison to the pulse centre frequency. The net effective shift in the pulse centre frequency is caused by frequency-dependent attenuation and does not affect the duration of the bit period, calling this analysis into question. This argument was supported with simulated filter envelopes showing high side-lobe type artefacts that the authors attributed to the effects of attenuation on complementary side-lobe cancellation. Our investigations suggest that these are in fact due to an aliasing issue within the Field II simulator's implementation of frequency-dependent attenuation. The FM pulses are inherently band-limited and unaffected by this issue. In the course of this thesis research, these aliasing artefacts were successfully reduced to -150 dB levels by low-pass filtering and an appropriate choice of chip. A final relevant point is that the imaging frequencies used are almost double those used during the earlier reported investigations, in which a pulse centre frequency of 4 MHz was used. At the higher frequency of 7.5MHz used in the current work, the higher resistance of BPC signals to attenuation becomes more apparent.

Offset against the benefits of complementary-coding are a potential reduction in image acquisition rate and complications introduced by motion when combining reflections from discrete pulse acquisition intervals. These issues are discussed in Chapter 5, along with some methods for dealing with them.

Chapter 5
Motion-Compensated Imaging

5.1 Introduction

One of the many challenges in ultrasonic B-mode image acquisition is to improve image "quality" while maintaining an acceptable rate of image acquisition. The key factors determining frame-rate are the acquisition period, T_r, and the number of acquisitions required to form a B-mode image, N_{Acq}. In Chapter 4, complementary BPC signals were shown to offer a number of advantages over FM signals, particularly at higher imaging frequencies and depths. These advantages come at the cost of an increase in N_{Acq} and a corresponding reduction in frame-rate. Motion between coded acquisitions can also introduce some de-correlation between the complementary filter outputs. A change in position of a scattering element between complementary acquisitions will induce a relative change in time of arrival of subsequent reflections from that element, causing misalignment between the filtered reflections corresponding to individual signals of the set, potentially reducing the GSNR of the sum of complementary filter outputs and introducing visible misalignment artefacts.

A novel approach to B-mode imaging using complementary codes, designed to address both of these issues, is presented in the current chapter. Established methods of ultrasonic velocity estimation are used to compensate for tissue motion between complementary data acquisitions. Ultrasonic back-scatter from blood is relatively low in amplitude and blood flow estimation usually requires rapid transmission of a number of pulses in the same focal direction and averaging of multiple estimates to reduce error. The relatively long period between complementary emissions would render blood-flow estimation impractical, but back-scatter from tissue is much higher in magnitude and the range of velocities present tends to be significantly lower than in blood. Motion compensation allows the acquired data to be used recursively, effectively eliminating the frame-rate reduction associated with complementary-coded imaging. The recursive motion-compensated imaging algorithm described is compatible with the orthogonal Golay-coded imaging alluded to in Chapter 3 and the two methods could be combined to increase frame-rate beyond the levels achievable using uncoded imaging pulses.

The signal-flow for the proposed system is outlined in Section 5.2. Section 5.3 describes the effects of homogeneous motion (where all scatterers within the beam are moving coherently) on complementary-coded imaging and introduces a method of motion compensation, while Section 5.4 describes the effects of more complex motion profiles (where scatterer velocities vary within the beam) and a modified approach to motion compensation designed to minimise them. Some conclusions and suggestions for future research are presented in Section 5.5.

5.2 System Outline

Consider a B-mode image consisting of N_l image lines and using N_f transmit focal depths per line. Using an uncoded pulse or single-transmit code, N_f acquisitions are required to form each image line and $N_f N_l$ acquisitions to form the full image. Using a set of N_c complementary codes, the number of acquisitions required to form a single image becomes $N_c N_f N_l$. Conventionally, every code of the set is transmitted in each focal direction in turn, i.e. N_c time-adjacent acquisitions are required to gather echo data for a single transmission focus, while $N_c N_f$ time-adjacent acquisitions are used to form each full image line. This ensures that the complementary ultrasonic reflections that are combined to form the B-mode image for a given focal depth and image line are acquired T_r seconds apart, where T_r is the pulse repetition period, thus minimising the effects of motion on complementary side-lobe cancellation.

The approach proposed in this chapter is to acquire data for an entire image using each code of the set in turn. As complementary acquisitions for each transmission focus are $N_f N_l T_r$ seconds apart, tissue motion can introduce significant visual artefacts due to partial side-lobe cancellation. This may, however, be counteracted by re-aligning the received data using estimates of the motion so that the side-lobes cancel appropriately. Using this approach, $N_c N_f N_l$ acquisitions are required to form the first B-mode image but a new image is formed after each subsequent $N_f N_l$ acquisitions as the acquired data may be used recursively, allowing complementary coded imaging to be employed without incurring a frame-rate penalty. A similar method was proposed by Nikolov [68] for a different problem: that of high frame-rate synthetic aperture imaging using single-transmit linear-FM coded excitation signals.

In the interests of clarity, all block diagrams and mathematical descriptions throughout this chapter refer to the signal flow for a single line (or transmission focus) of a B-mode image using a fixed receive focus. Scaling for multiple lines is a straightforward extension. As in

Chapter 3, the simulated results presented here were all generated using post-compression, although the method is equally applicable to a system using pre-compression.

5.2.1 Transmit Coding

As in Chapter 3, the two codes of a Golay pair are used to modulate a basis sequence consisting of a single-cycle chip at the transducer centre frequency, f_c, allowing the spectrum of the transmitted waveform to be dictated by the transducer frequency response. The resulting signals are transmitted during alternate acquisition cycles in a repeating series such that the signal transmitted at the start of the ith acquisition cycle $g(i,t) = g(i-N,t)$. This may be written in terms of $g_{\text{cpc}}(i,t)$, the complementary signal set defined in (3.37), as:

$$g(i,t) = g_{\text{cpc}}(i\%N, t) \tag{5.1}$$

where $i\%N$ represents the modulo operation. Defining a corresponding set of modulation sequences, $c(i,t)$, in a similar fashion:

$$c(i,t) = c_c(i\%N, t) \tag{5.2}$$

and, from (3.31)

$$g(i,t) = c(i,t) * b(t) \tag{5.3}$$

5.2.2 Receive Processing

The signal flow for the receiver system is illustrated in Figure 5.1. Delay-sum beam-forming is applied to the received signals prior to filtering.

After beam-formation, the received reflection from the ith transmitted pulse may be written:

$$\begin{aligned} r(i,t) &= g(i,t) * a_t(t) * s_{bf}(i,t) * a_r(t) + n_r(i,t) \\ &= g(i,t) * a_{tr}(t) * s_{bf}(i,t) + n_r(i,t) \end{aligned} \tag{5.4}$$

where $a_t(t)$ and $a_r(t)$ represent the impulse responses of the transmit and receive apertures, $a_{tr}(t)$ their combined response, $n_r(i,t)$ represents the lumped noise and $s_{bf}(i,t)$ is the reflectivity function of the region insonated by the beam during the ith acquisition expressed as a

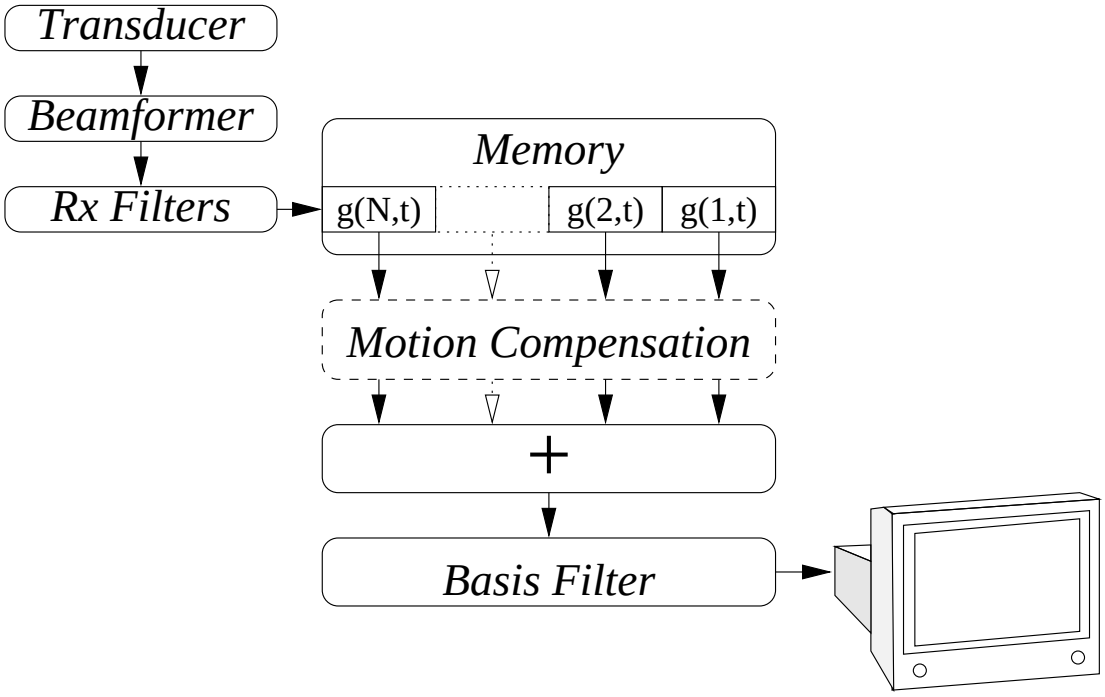

Figure 5.1: Receive signal flow for a motion-compensated complementary-coded imaging system. A/D conversion and time-gain control omitted for clarity.

function of time. Combining (5.3) and (5.4) gives us

$$\begin{aligned} r(i,t) &= c(i,t) * b(t) * a_{tr}(t) * s_{bf}(i,t) + n_r(i,t) \\ &= c(i,t) * b_{tr}(t) * s_{bf}(i,t) + n_r(i,t) \end{aligned} \tag{5.5}$$

where $b_{tr}(t)$ represents the convolution of the basis sequence with the combined transmit and receive aperture response. When using dynamic receive focusing and apodisation, $a_r(t)$ varies as a function of imaging depth and becomes $a_r(z,t)$. In these circumstances, the convolution in (5.5) is no longer time-invariant. This is one of the reasons that pre-compression should be used as discussed in Section 3.3. In practice, the error introduced by post-compression has proven to be minor for the small tissue displacements encountered in the types of imaging scenario envisioned, and the approximation is mathematically convenient for the explanations that follow.

As in Chapter 4, filtering of the received ultrasonic reflections is split into two stages. In the first, received signals are passed through a compression filter matched to the modulation sequence. In the second, which takes place after motion compensation, the sum of complementary-code filter outputs is passed through a basis filter matched to $b_{tr}(t)$.

The output of the compression filtering stage may be written as

$$\begin{aligned} r_f(i,t) &= c(i,T-t) * r(i,t) \\ &= c_{xx}(i,t) * b_{tr}(t) * s_{bf}(i,t) + n_g(i,t) \end{aligned} \tag{5.6}$$

where $n_g(i,t) = c(i,T-t) * n_r(i,t)$.

The sum of N adjacent complementary filter outputs is

$$\begin{aligned} m_u(i,t) &= \sum_{n=1}^{N} r_f(i-N+n,t) \\ &= \sum_{n=1}^{N} c_{xx}(i-N+n,t) * b_{tr}(t) * s_{bf}(i-N+n,t) + n_c(i,t) \\ &= b_{tr}(t) * \sum_{n=1}^{N} c_{xx}(i-N+n,t) * s_{bf}(i-N+n,t) + n_c(i,t) \end{aligned} \tag{5.7}$$

where $n_c(i,t) = \sum_{n=1}^{N} n_g(i-N+n,t)$.

If the region within the beam is stationary between acquisition cycles we can simplify $s_{bf}(i,t)$ to $s_{bf}(t)$ and Equation (5.7) becomes:

$$\begin{aligned} m_u(i,t) &= b_{tr}(t) * s_{bf}(t) * \sum_{n=1}^{N} c_{xx}(i-N+n,t) + n_c(i,t) \\ &= NL\delta(t-T) * b_{tr}(t) * s_{bf}(t) + n_c(i,t) \end{aligned} \tag{5.8}$$

As the components of n_g are uncorrelated, $n_c(i,t)$ and $n_g(i,t)$ are of equal power and the coding gain is $20\log_{10}(NL)$ dB.

Let $r_c(i,n,t), \quad 1 \le n \le N$ represent the outputs of the motion compensation block at the ith emission, with $r_c(i,N,t) = r_f(i,t)$. The role of the motion compensation block is to ensure that the sum of compensated outputs $m_c(i,t)$ approaches

$$
\begin{aligned}
m_c(i,t) &= \sum_{n=1}^{N} r_c(i,n,t) \\
&\cong b_{tr}(t) * s_{bf}(i,t) * \sum_{n=1}^{N} c_{xx}(i-N+n,t) + n_c(i,t) \\
&= NL\delta(t-T) * b_{tr}(t) * s_{bf}(i,t) + n_c(i,t)
\end{aligned}
\tag{5.9}
$$

Section 5.3 describes some ways in which this may be accomplished.

5.3 Homogeneous Motion and Compensation

5.3.1 Motion Model

Consider a moving scattering element, p, that occupies positions $\vec{p}_a$ and $\vec{p}_b$ during two discrete acquisition intervals using the same transmission focus, as illustrated in Figure 5.2. If the same

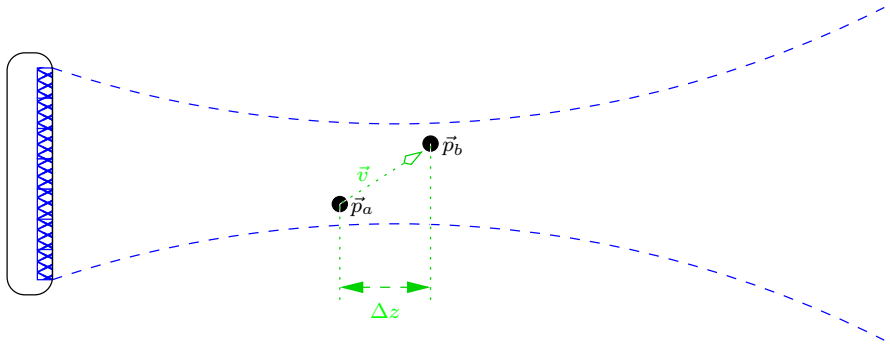

Figure 5.2: Motion of a scattering element between acquisitions

imaging pulse is transmitted during both acquisition intervals, the relationship between the received echoes, $s(a,t)$ and $s(b,t)$, is approximately

$$
s(b,t) \cong \alpha_a^b s(a, t-\tau_a^b) \tag{5.10}
$$

where $\tau_a^b \cong \frac{2\Delta z}{c}$ is the round-trip delay corresponding to the change in position of the scatterers between the ath and bth acquisitions and $\alpha_a^b = \frac{1}{\alpha_b^a}$ is a lumped gain term accounting for the altered position of the scattering element within the acoustic field. The $\cong$ in Equation (5.10) is due to the small variation in the transmit-receive response of the aperture due to the change in scatterer position. This may usually be disregarded for the minor displacements caused by

tissue motion between acquisition cycles.

Assuming the motion of all scatterers in the region insonated by the beam is homogeneous, it is possible to relate the reflectivity functions of the region insonated by the beam during discrete acquisition intervals using the same model:

$$s_{bf}(b,t) \cong \alpha_a^b s_{bf}(a, t - \tau_a^b) \tag{5.11}$$

Let $r_s(i,n,t)$ represent reference complementary filter outputs defined on the interval $1 \leq n \leq N$ such that:

$$r_s(i,n,t) = c_{xx}(i+n,t) * b_{tr}(t) * s_{bf}(i,t) + n_r(i,t) \tag{5.12}$$

Their sum, $m_s(i,t)$, is:

$$\begin{aligned} m_s(i,t) &= \sum_{n=1}^{N} r_s(i,n,t) \\ &= NL\delta(t-T) * b_{tr}(t) * s_{bf}(i,t) + n_c(i,t) \end{aligned} \tag{5.13}$$

Note that Equations (5.1) and (5.2) have been used to simplify the indices somewhat. Combining Equation (5.7) with Equations (5.11) and (5.12) allows us to write the sum of uncompensated filter outputs as:

$$\begin{aligned} m_u(i,t) &= \sum_{n=1}^{N} r_s(i,n,t - \tau_i^{i-N+n}) \\ &= b_{tr}(t) * \sum_{n=1}^{N} c_{xx}(i-N+n,t) * \alpha_{i-N+n}^{i} s_{bf}(i, t - \tau_i^{i-N+n}) + n_c(i,t) \end{aligned} \tag{5.14}$$

The degree of misalignment, represented in Equation (5.14) by the τ_i^{i-N+n} term, is a function of scatterer velocity and the time between acquisitions. This depends on the pulse repetition frequency (PRF), which is determined by the maximum depth of interest and the length of the transmitted pulse. The time between acquisitions of lines along the same focal direction is a function of the PRF, the number of focal regions used on transmit and the number of lines used to form the B-mode image.

5.3.2 Motion Compensation

Making the simplifying assumption that $\alpha \cong 1$ for small displacements, Equation (5.14) becomes:

$$m_u(i,t) = b_{tr}(t) * \sum_{n=1}^{N} c_{xx}(i-N+n,t) * s_{bf}(i,t-\tau_i^{i-N+n}) + n_c(i,t) \tag{5.15}$$

Using this simplified model, it is possible compensate for the effects of motion based on estimates of the change in round-trip time, τ, as illustrated in Figure 5.3. A wide range of methods for ultrasonic velocity/motion estimation have been reported in the literature, a number of which were described in Chapter 2. In the current system, an interpolated estimate of the normalised cross-correlation maximum [34] is used to re-align the complementary filter outputs before summation, although another wide band tissue-motion estimation algorithm could be used in its place [55, 90]. The reflections being cross-correlated are from different codes of the complementary set, which have different (complementary) side-lobe structures. These complementary side-lobes give rise to a more defined (if slightly diminished) correlation peak. Log-linear gain correction was applied to the filtered data prior to motion estimation in order to prevent strong reflections from scattering centres close to the transducer from masking more attenuated reflections from deeper regions and dominating the motion estimate. This step is unnecessary for the homogeneous motion described in the current section but beneficial when the motion is not homogeneous in nature, a topic discussed in detail in Section 5.4.

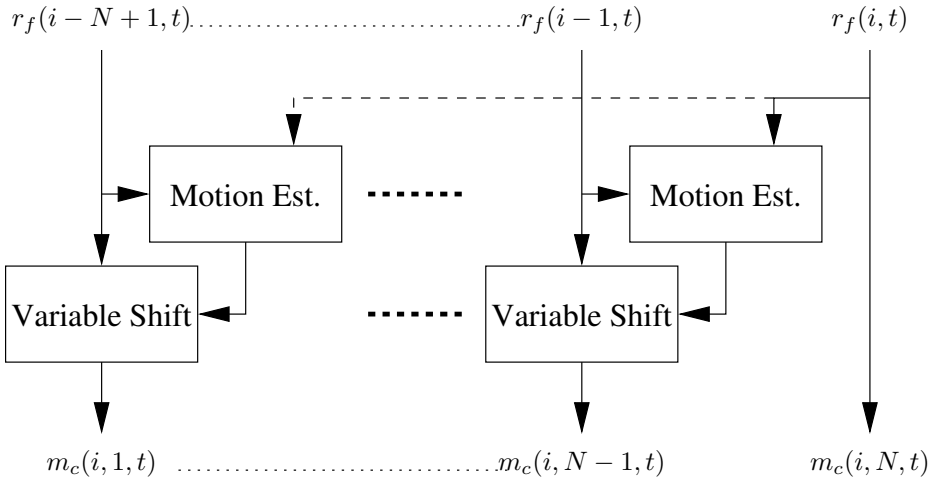

Figure 5.3: Motion compensation block diagram.

If $\tilde{\tau}_a^b$ represents the estimated change in round-trip time due to motion between the a^{th} and b^{th}

acquisitions and ϵ_a^b the estimate error, $\epsilon_a^b = \tau_a^b - \tilde{\tau}_a^b$,

$$\begin{aligned} r_c(i,n,t) &= r_f(i-N+n, t-\tilde{\tau}_i^{i-N+n}) \\ &= r_s(i,n,t+\epsilon_i^{i-N+n}) \end{aligned} \tag{5.16}$$

The sum of compensated outputs is then,

$$\begin{aligned} m_c(i,t) &= \sum_{n=1}^{N} r_c(i,n,t) \\ &= b_{tr}(t) * \sum_{n=1}^{N} c_{xx}(i-N+n,t) * s_{bf}(i,t+\epsilon_i^a) + n_c(i,t) \end{aligned} \tag{5.17}$$

which approaches Equation (5.13) as the error term ϵ approaches zero. Complete compensation is unlikely in a typical imaging scenario but partial compensation has proved to be effective in reducing side-lobes to levels that compare favourably with other coding schemes proposed in the literature, as will be demonstrated in the remainder of this chapter.

5.3.3 Simulation Results

The effects of homogeneous motion were simulated in Matlab by updating the positions of individual scatterers between line acquisitions. The applied motion was sinusoidal in nature to approximate human respiration. A peak scatterer velocity of 6.2 mm/second and angular velocity of $\frac{\pi}{3}$ radians/second were used based on figures published by Schlaijker et al. [81]. An initial phase of $\frac{\pi}{2}$ radians was chosen to ensure the velocities simulated during the scan were around the peak value. For simulations involving motion, two alterations to the signal and simulation parameters described in Chapter 4 were required. The sampling frequency of the Field II simulator was increased by a factor of 10 to 1.5 GHz, as the positional accuracy of simulations is a function of the simulator sampling frequency. The number of scatterers making up the simulated cyst phantom was reduced from 300000 to 50000 in order to offset the increase in simulation time due to the higher simulator sampling frequency. The introduction of simulated axial motion caused side-lobe cancellation to break down. This reduces coding gain and axial resolution and introduces the severe misalignment side-lobes visible in the uncompensated filter envelopes in Figures 5.4 (a) and 5.4 (b), while motion compensation reduces the misalignment side-lobes to -51dB and -60dB, respectively, for the scatterers at 5mm and 95mm.

Side-lobe level has been plotted against depth in Figure 5.4 (c), in which the uncompensated

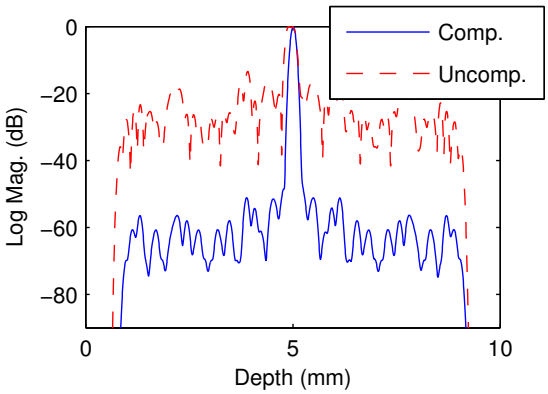

(a) Point scatterer at 5mm

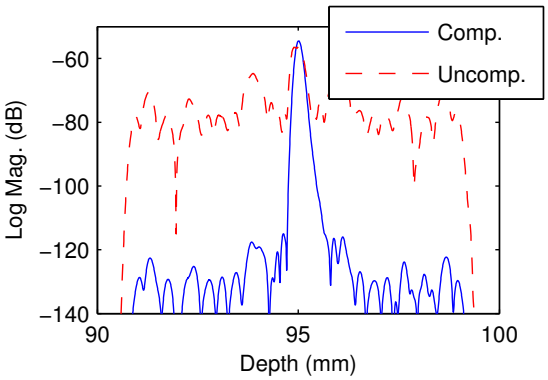

(b) Point scatterer at 95mm

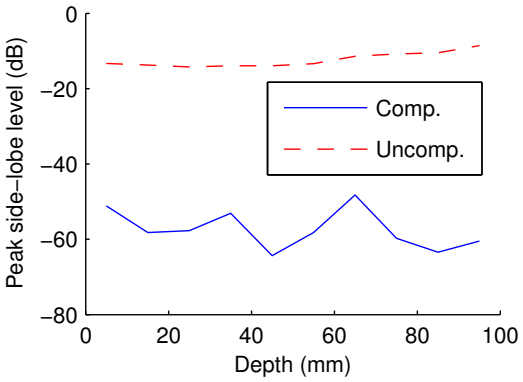

(c) Side-lobe level vs. depth

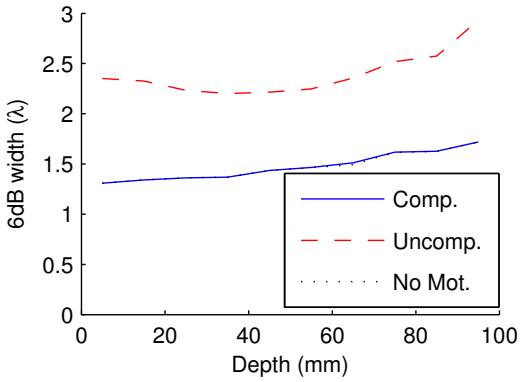

(d) Resolution vs. depth

Figure 5.4: Effects of homogeneous motion and compensation on simulated filter response envelopes using a Golay coded pulse pair and point phantom.

envelopes (labelled *Uncomp.* in the Figure) exhibit a mean peak side-lobe level of about -12dB while compensation reduces this value to -57dB. The local minima of the line representing the motion-compensated results occur at the three focal depths used on transmit. Figure 5.4 (d) is a plot of main-lobe resolution vs. depth. In the presence of uncompensated motion, the mean -6dB width of the main-lobe is 1.6 times that of the reference result obtained without simulated motion (the line labelled *No Mot.*). After motion compensation, the mean -6dB width of the main-lobe matches that of the reference. Taken together, these figures suggest that the efficacy of compensation is not significantly affected by attenuation.

Figure 5.5 illustrates the implications of these results for B-mode imaging. The side-lobes introduced by motion are manifested as visual artefacts in the uncompensated B-mode image on the left of the figure. Compensation brings the motion artefacts below the visual threshold and the resulting images again demonstrate an increase in axial-resolution and noise-rejection compared to those obtained using FM pulses (in Chapter 4).

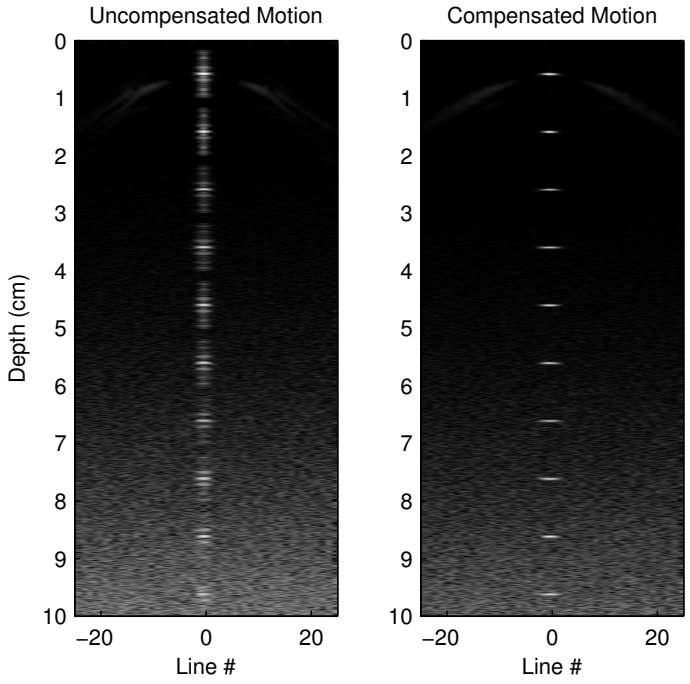

Figure 5.5: Effects of motion and compensation on B-mode imaging using a Golay-encoded signal pair at 50dB SNR.

5.3.4 Experimental Results

In the experiments conducted at BGS, motion was simulated by adjusting the separation of the transducers between code transmissions. Data was recorded for nine different separations, increasing in 1mm increments. The dashed lines in Figure 5.6(a) represent the uncompensated Golay response envelope using data from positions 2mm apart. Figure 5.6(b) shows similar results obtained during the experiments conducted at the University of Edinburgh. In these, data was captured using a single transducer and reflecting the signal from the wall of the tank, while motion was simulated by moving the transducer between transmissions (20 μm in this instance). In both cases, motion introduced side-lobes at about -23dB. The solid line in Figure

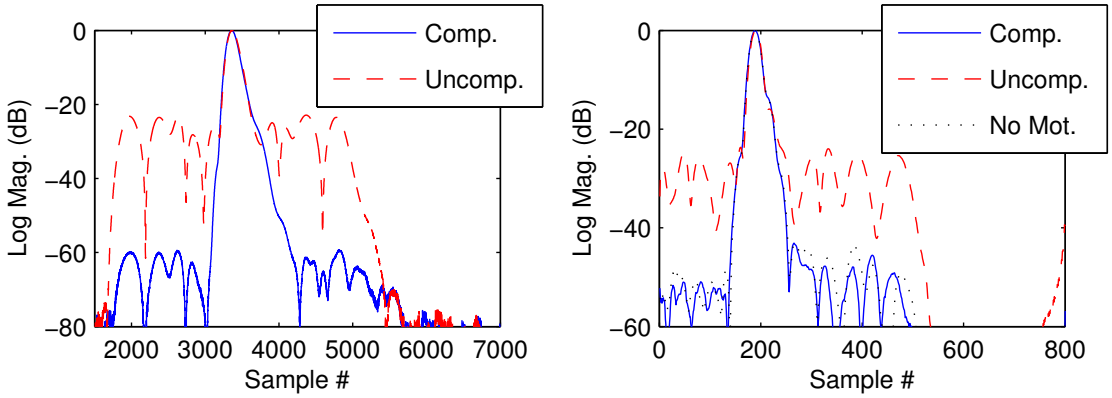

(a) BGS experiments

(b) University of Edinburgh experiments

Figure 5.6: Effects of motion and compensation on filter response envelopes from BGS and medical physics experiments

5.6(a) represents the motion compensated filter outputs for a transducer displacement of 2mm between acquisitions. In this case, compensation has reduced side-lobes to around -60dB.

The solid line in Figure 5.6(b) represents compensated data obtained using the University of Edinburgh facilities. Here the compensated filter envelope exhibits lower side-lobes than the reference envelope obtained by transmitting both coded signals from the same position. The side-lobes in the reference envelope are most likely due to random timing jitter between the multiple clock sources present in the experimental setup and should not be an issue in a clinical scanner using a single clock signal.

5.4 Inhomogeneous Motion

5.4.1 Mirroring and Segmented Compensation

When performing a scan of a living subject, different regions of the beam may contain scatterers moving at different rates. In this situation, a motion estimate obtained using a cross-correlation-based method is likely to approach the weighted mean of the velocities present in the region, where the weights are a function of the back-scatter coefficients of the various scattering centres within the beam. In this scenario, motion compensation using the method described in Section 5.3 will be less effective for those scattering centres whose velocities are at the edges of the range present in the medium.

Two refinements of the motion-compensation algorithm have been evaluated for use in scenarios of this type. The first of these is *segmented motion compensation*, whereby each image line is divided into multiple segments. Distinct motion estimates are formed for each segment and used to compensate that segment individually. This approach is based on the assumption that a smaller region of the beam is likely to contain a smaller spread of velocities than the beam in its entirety, lessening the degree of incomplete compensation. The extent of the impact of individual highly reflective scattering regions on compensation is also limited to a single compensation segment rather than the entire line.

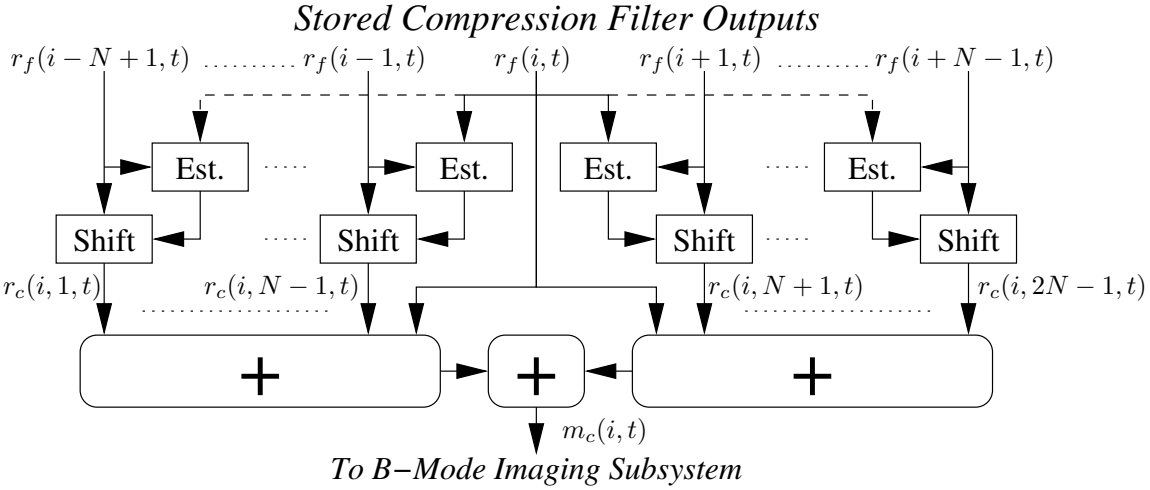

Figure 5.7: Mirrored motion compensation for a single image line

The second refinement to the algorithm was the development of a novel method for motion compensation depicted in Figure 5.7. This has been christened *mirrored motion compensation*

due to the axial symmetry evident in the block diagram. Using this method, $2N-1$ lines of received data are used to form each output. Two distinct compensated image lines are formed using the 1st to Nth and Nth to $(2N-1)$th lines of complementary-filtered data. The central (Nth) line of received data, common to both compensated lines, is used as the positional reference for both sets of motion estimates and the mirror-compensated output is formed by adding the individual compensated outputs. As each compensated line is based on a different set of motion estimates, any residual misalignment side-lobes tend not to coincide and often prove to interfere with one another destructively.

Using this mirrored structure, the individual motion compensated outputs remain as defined in Equation (5.16), while the mirrored sum of compensated outputs becomes:

$$\begin{aligned} m_m(i,t) &= \sum_{a=1}^{N} r_c(i,a,t) + \sum_{a=N}^{2N-1} r_c(i,a,t) \\ &\approx 2NL\delta(t-T) * b_{tr}(t) * s_{bf}(i,t) + \dots \\ &\dots \sum_{a=1}^{2N-1} n_g(i,t) + n_g(N,t) \end{aligned} \tag{5.18}$$

The coding gain for the mirrored output remains the same as for the individual compensated outputs due to the doubling of the $n_g(N,t)$ term in Equation (5.18). The filter peaks coincide due to the common compensation reference. The mirrored structure effectively spreads the effect of individual alignment errors is over two frames, reducing their visual impact in any one. The additional computational cost entailed is comparatively low and the improvement in compensation performance can be significant.

5.4.2 Simulation Results

Inhomogeneous motion was simulated in Matlab by scaling the motion applied to individual scatterers in proportion to their axial distance from the transducer, producing an effect similar to an elastic expansion of the simulated phantom. In this situation:

$$s_{bf}(i,t) \cong s_{bf}(i-1, t-\tau_{i-1}^{i}\frac{t}{t_{\text{max}}}) \tag{5.19}$$

where t_{max} is the round-trip propagation time corresponding to the maximum depth of interest. The B-mode images in Figure 5.8 were generated using simulated elastic motion with the

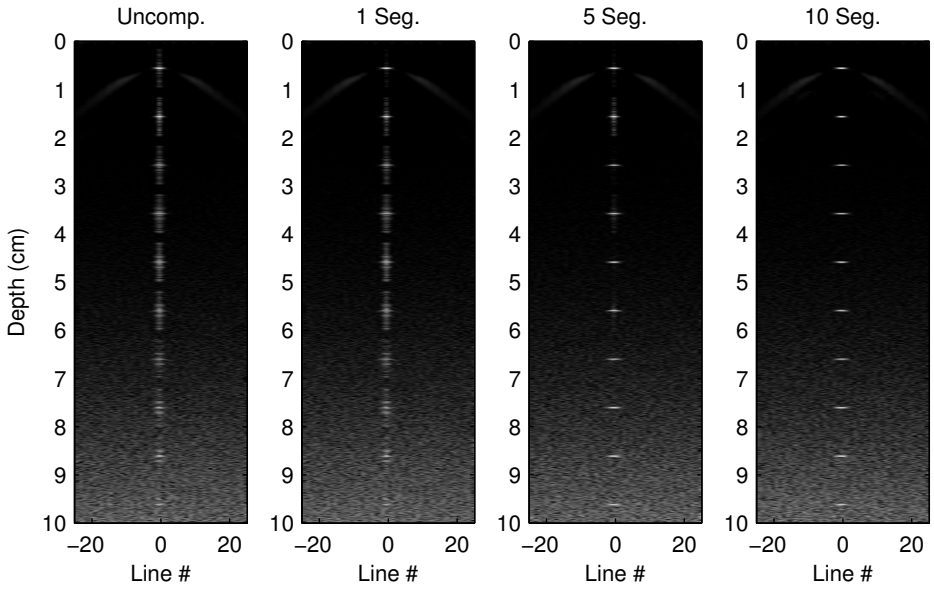

Figure 5.8: Uncompensated, single-, five- and ten-segment motion-compensated images of an elastic point phantom. 50dB SNR

same maximum velocity and initial phase as reported in Section 5.3. Without compensation, misalignment side-lobe artefacts increase steadily with increasing distance from the transducer. Application of the single-segment motion compensation algorithm described in Section 5.3.2 results in a slight but inadequate reduction in side-lobe artefacts. Increasing the number of compensation segments to five reduces these artefacts considerably, while ten-segment compensation brings them below the visible threshold. The introduction of mirrored compensation stages reduces the levels of misalignment side-lobes further, as illustrated in Figure 5.9. The

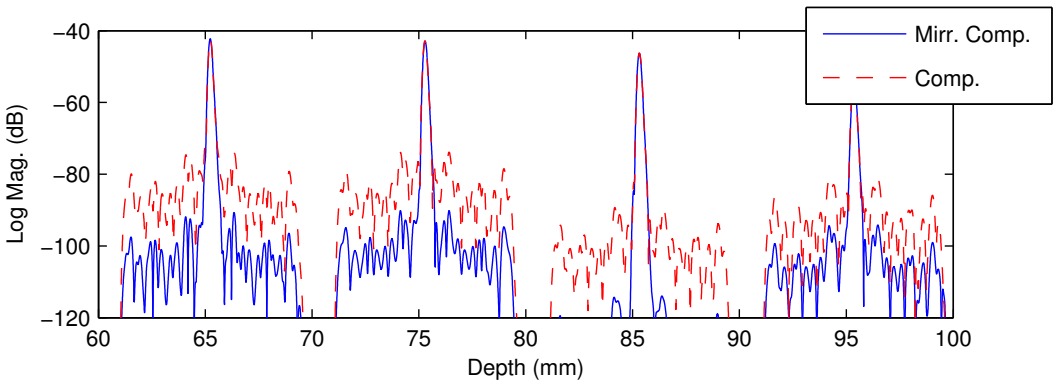

Figure 5.9: Effects of mirrored compensation on 5-segment compensated filter envelopes

effects of mirrored compensation on uncompensated and multi-segment compensated filter envelopes obtained using the simulated point phantom and inhomogeneous motion are illustrated

quantitatively in Figure 5.10. The numbers in the legend represent the number of compensation segments used and "M" indicates the use of mirrored motion compensation. The benefits are

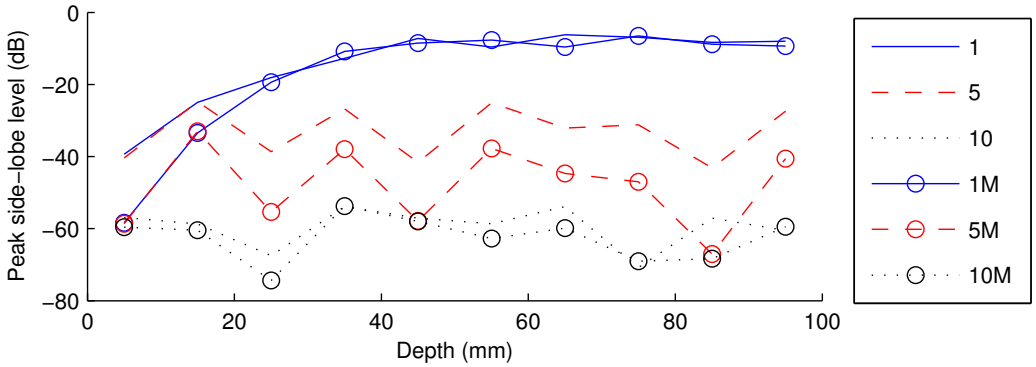

Figure 5.10: Effects of segmented compensation and mirroring on simulated filter envelopes of the point phantom

not always significant but come at very little additional computational cost and can in some cases reduce artefacts considerably. This is particularly evident from the five-segment mirror-compensated B-mode image in Figure 5.11, in which the residual misalignment side-lobes evident in Figure 5.8 have been all but eliminated by mirrored compensation. The B-mode images

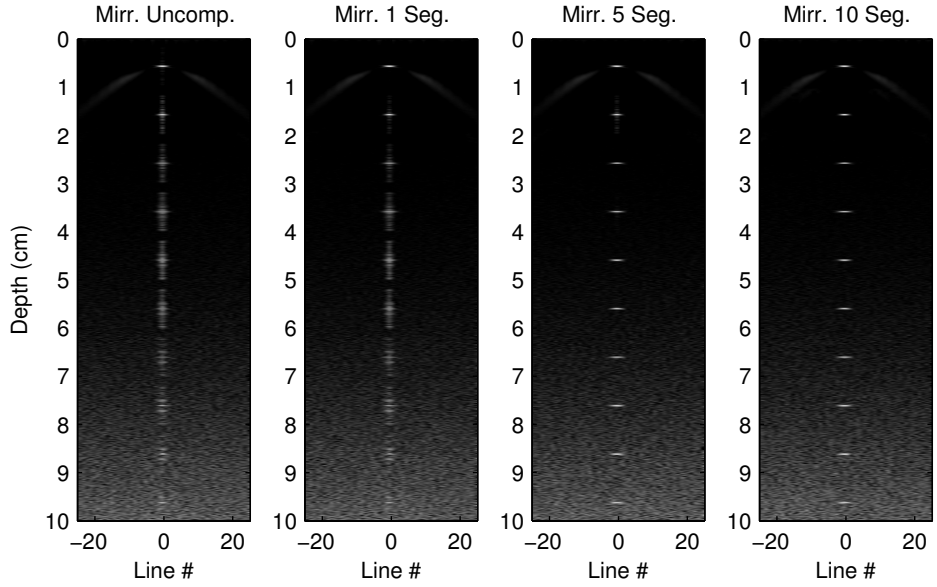

Figure 5.11: Uncompensated, single-, five- and ten-segment motion-compensated images of an elastic point phantom. Mirrored compensation stages. 50dB SNR

in Figures 5.12 and 5.13 were generated using the cyst phantom and simulated elastic motion. In Figure 5.12 (a), the severe motion artefacts apparent in the uncompensated image are reduced

but not eliminated by the application of single-segment motion compensation. 5-segment compensation reduces these artefacts significantly, though faint side-lobes are discernible in the images of highly-reflective points at depths of 35mm and 55mm, while 10-segment motion compensation eliminates them entirely. In Figure 5.12 (b), 5-segment mirrored motion compensation is sufficient to eliminate visible motion side-lobe artefacts. Noise at -40dB was added to the data used to generate Figures 5.13 (a) and 5.13 (b). These compare favourably to the FM images in 4.22, which were generated under similar conditions using signals of twice the duration.

5.4.3 Experimental Results

Figure 5.14 was generated using motion data from the BGS experiments. The three successive peaks correspond to direct transmission between the two transducers and the first and second reflections between the transducer faces. As the transducer was moved 2 mm between acquisitions, the first and second reflections are misaligned by 6mm and 10mm, respectively, resulting in a motion profile similar to that produced by the "elastic" motion used in simulations. Application of single segment compensation aligns the first peak, leaving the reflections with severe misalignment side-lobes. Segmented compensation, however, produces an envelope that conforms very closely to that obtained with no motion.

5.5 Conclusions

As demonstrated in the previous chapter, the proposed Golay-based scheme demonstrates promising performance under simulated conditions with an appreciable improvement in axial resolution compared to the linear FM-chirp, greater flexibility in choice of code-length than Barker-coded imaging and the increased resilience of the binary-filtered Golay codes to attenuation translates to a significant increase in coding gain at higher imaging depths. These advantages come at the expense of a potentially significant reduction in frame-rate and complications introduced by motion between complementary pulse emissions.

The motion-compensated imaging algorithm proposed in this chapter eliminates the loss in frame-rate often associated with complementary-coded imaging while maintaining side-lobe levels comparable to those of optimal FM signals. In addition, the technique is applicable to Golay complementary codes of any length, whereas time-bandwidth products of 50 or more are

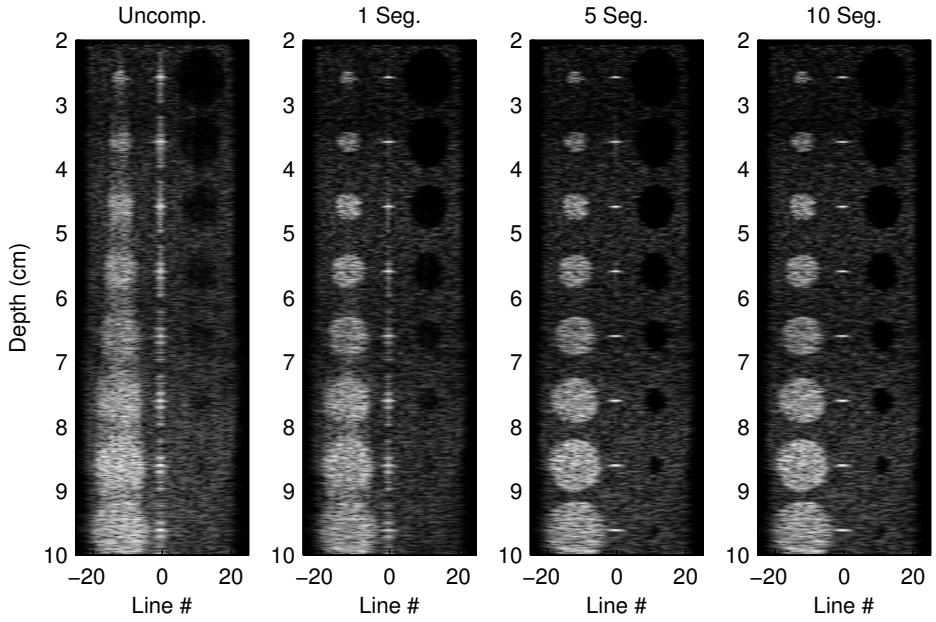

(a) Multi-segment compensation

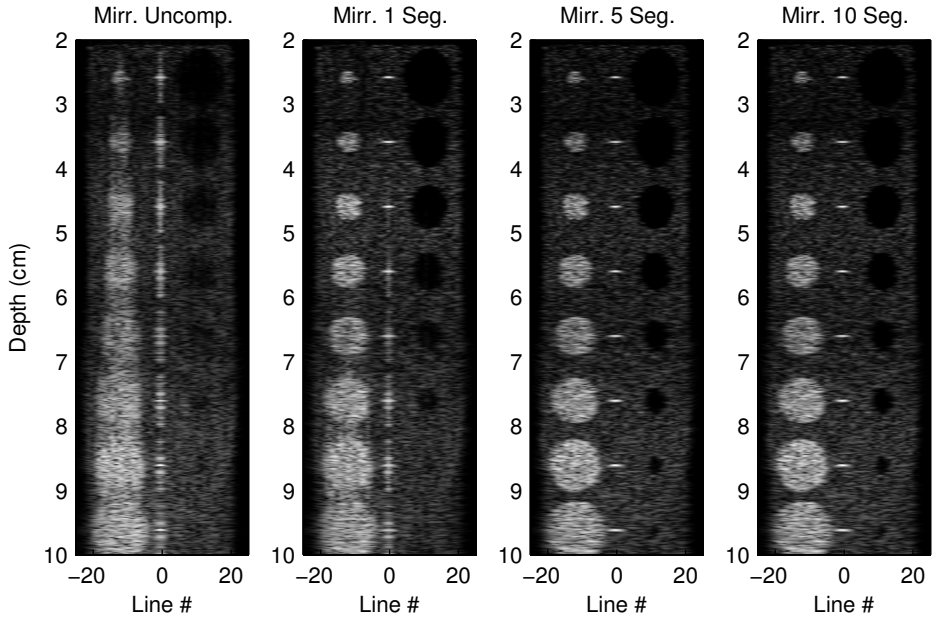

(b) Mirrored multi-segment Compensation

Figure 5.12: Motion-compensated images of a cyst phantom. No additive noise

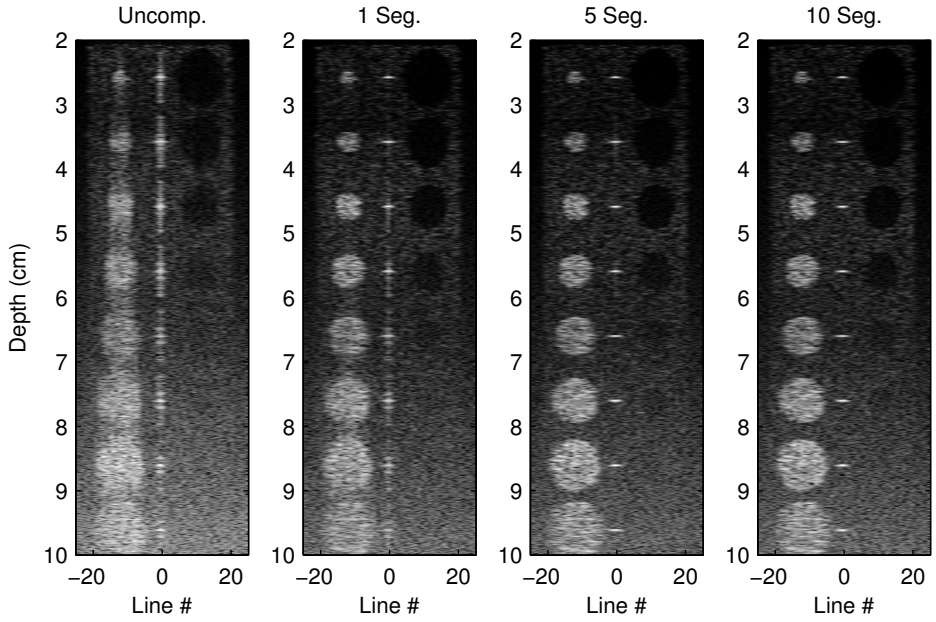

(a) Multi-segment compensation

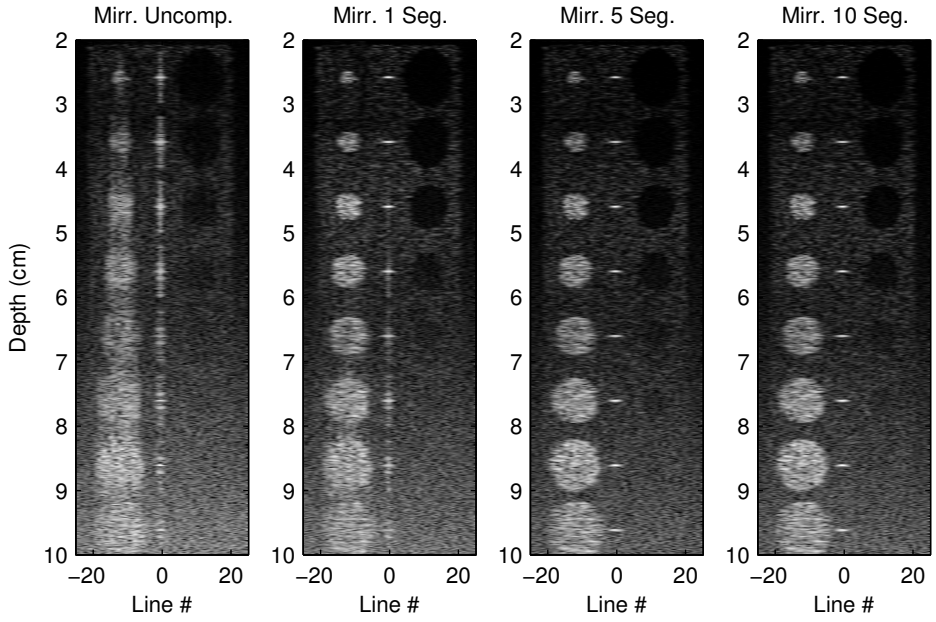

(b) Mirrored multi-segment Compensation

Figure 5.13: Motion-compensated images of a cyst phantom. 40dB SNR

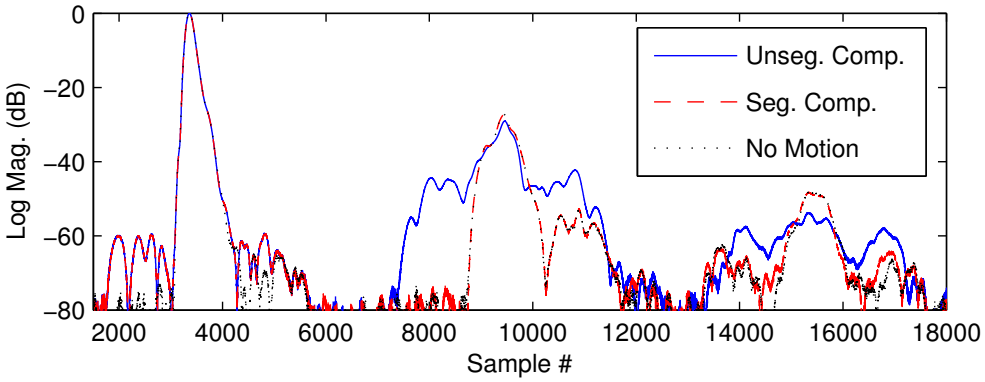

Figure 5.14: Segmented motion compensation applied to data from BGS experiments

required in order for side-lobes to be kept at acceptable levels for FM-coded signals. Motion-compensation performance with simulated time-varying homogeneous motion of a number of point targets and of a simulated cyst phantom has been demonstrated to be very satisfactory. Inhomogeneous motion reduces the efficacy of compensation, but the segmentation and mirroring discussed in Section 5.4 reduce visual artefacts significantly. The method appears to be particularly attractive for high imaging frequencies, due to its robustness to the effects of frequency-dependent attenuation.

Preliminary experimental results suggest the methods could be successfully implemented in a commercial imaging system. Combining the method with the orthogonal code pairs and simultaneous transmission described in [12, 19, 20] could potentially provide the benefits of complementary signal coding at twice the frame-rate of conventional B-mode imaging. In a system using multiple transmit foci, it may be appropriate to use a number of different code lengths. Shorter codes or uncoded pulses could be used for focal regions near the transducer to minimise the occurrence of residual misalignment artefacts and longer codes used for deep imaging to maximise coding gain.

Chapter 6
Complementary Codes in Synthetic Transmit Aperture Medical Ultrasonography

6.1 Introduction

Synthetic aperture imaging was introduced in Chapter 2. The work described in this chapter all relates to synthetic transmit aperture (STA) imaging, which allows great flexibility in transmit focusing and apodisation; anything from a fixed transmit focal point to full dynamic transmit focusing and apodisation may be used without any increase in acquisition time. In sequential-scan imaging, by contrast, the acquisition time increases linearly in proportion to the number of focal depths used in transmission. Real-time synthetic aperture medical ultrasonography is beyond the capabilities of current commercial devices due to the high computational cost of aperture synthesis, though the area has been attracting considerable research interest in recent years.

Both STA imaging and conventional sequential-scan imaging involve the combination of data acquired over multiple acquisition intervals. In sequential-scan imaging, B-mode images are built up in a piece-wise fashion: a high-resolution image of a small section of the region of interest is formed during each acquisition interval and these multiple small images assembled into a larger high-resolution image. Motion between acquisition intervals may result in geometric distortion of large anatomical features but will not cause motion-blur type artefacts to appear. In STA imaging, on the other hand, a low-resolution image of the entire region of interest is formed during each acquisition interval and multiple low-resolution images are combined to form a high-resolution image. Motion between acquisitions results in misalignment of individual low-resolution images and causes blurring in the high resolution synthetic-aperture image. This topic is discussed in detail in [69], which suggests the adoption of a cross-correlation based motion-compensation algorithm in order to deal with it. A system of this type may be readily adapted to use motion-compensated complementary-coded imaging pulses at the cost

of very little additional computational overhead. The coding gain and robustness to attenuation of complementary binary-phase coded signals are particularly desirable in sparse STA imaging as the reduced number of transmitting elements reduces the focal gain of the transmit aperture.

A description of recursive STA imaging using single-transmit coded pulses is developed in Section 6.2, based on the work presented by Nikolov in [69]. This description is extended in Sections 6.3 and 6.4 to allow the use of motion-compensated complementary-coded signals. The discussion is supported by simulation results obtained using Field II and the Beam-Formation Toolkit (BFT). An alternative approach to complementary-coded STA imaging that may provide advantages in certain imaging situations is suggested in 6.5 and some conclusions are drawn in Section 6.6.

The simulation study described in this chapter was completed after an initial investigation of motion-compensation for complementary-coded sequential-scan B-mode imaging. It predates the implementation of the non-linear FM pulse design algorithm and the detailed study of coded-pulses for high-frequency imaging reported in Chapters 3 and 4, during which significant refinements were made to the simulation environment and the signal and filter design methods employed. The results reported here date from an earlier stage in this thesis research and used a lower imaging frequency and some different signal and scan parameters from those reported in previous chapters. These are described in Section 6.4.6. All the descriptions and simulations use single-element sources and full aperture synthesis, though the techniques are equally applicable using the virtual sources and sparse transmit aperture synthesis described in Chapter 2.

6.2 Synthetic Transmit Aperture Imaging

The block diagram of a recursive STA imaging system may be seen in Figure 6.1. In such a system, a full STA scan requires transmission of an imaging pulse through all E elements of the transmit aperture in turn. The signals received at each element in the receive aperture are compression-filtered and beam-formed to give a new low-resolution image of the entire region under examination after each acquisition interval. These low-resolution images, which will be referred to throughout this chapter as *L-images*, are acquired T_r seconds apart, where T_r is the reciprocal of the pulse repetition frequency, f_r. A full scan takes place over a single *aperture-cycle* of duration $T_a = ET_r$.

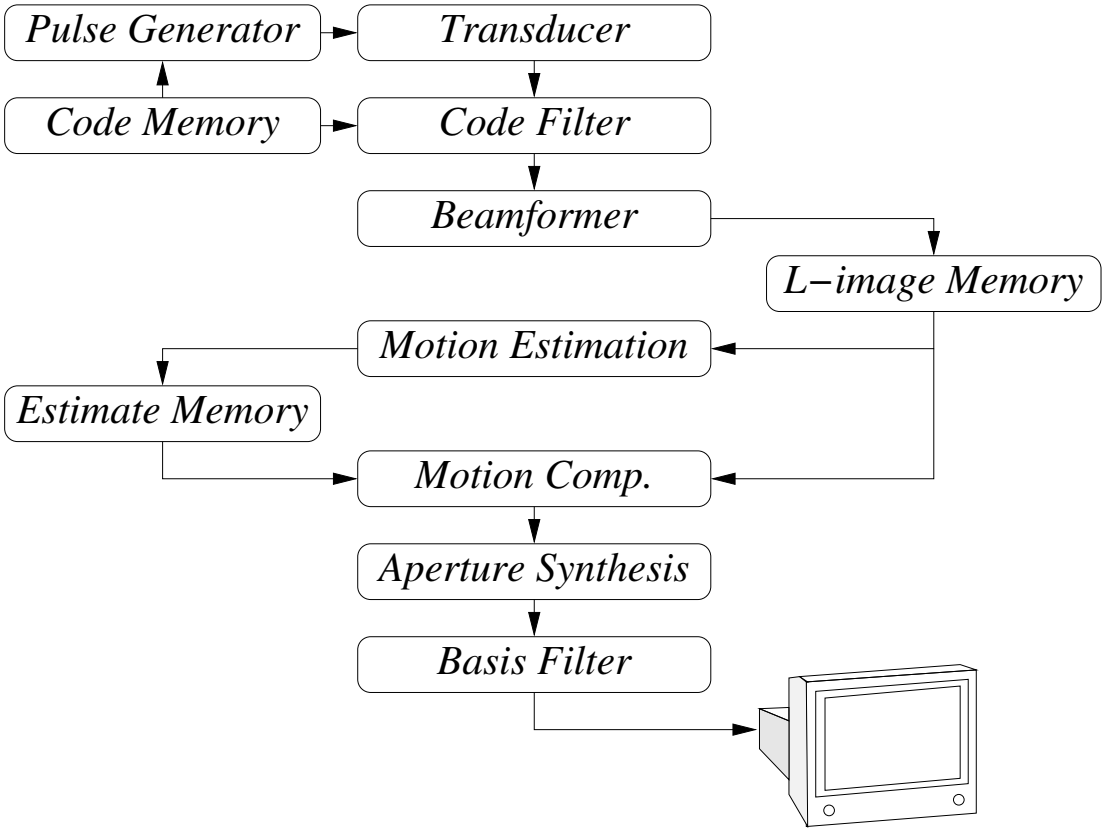

Figure 6.1: Signal flow: Recursive STA imaging

Any E time-adjacent L-images will include one L-image acquired using each element of the transmit aperture and may be used to form a high-resolution synthetic aperture image, or *H-image*. Transmit focusing may be performed by weighting and time-shifting the L-images during aperture synthesis. This allows the application of dynamic transmit focusing and apodisation, which is not possible in sequential-scan ultrasound imaging.

Motion between L-image acquisitions introduces artefacts in the synthetic-aperture image. These are reduced by aligning L-images based on estimates of the motion over the course of one or more aperture-cycles. Motion compensation can be performed recursively, allowing a new high resolution H-image to be synthesised after every emission based on the positions of scatterers during the most recent acquisition interval.

In practice, full recursive aperture compensation can result in frame-rates far higher than are required for video and require prohibitive amounts of computation. The advantage of recursion is that it allows the system frame-rate to be set independently of the aperture-cycle duration. A new H-image may be generated after every kth acquisition interval, for any $k \in \mathbb{N}_1$, yielding a frame rate of $\frac{f_r}{k}$.

In order to describe recursive aperture compensation clearly, it is convenient to derive a relationship between the transmitting *element index*, $e \in \{0, 1, ..., E-1\} \forall i$, and the *acquisition interval index*, $i \in \mathbb{N}_0$. Throughout this chapter, e_i will be used to indicate the element of the synthetic transmit aperture used during the ith acquisition interval and may be defined as follows:

$$e_i = i\%E \tag{6.1}$$

where $\%$ indicates the modulo operation.

6.2.1 Transmitted and Received Signals

Consider an E-element transducer array with elements located at $(x[e], 0, 0), \quad 0 \leq e \leq (E-1)$. During each acquisition interval, an imaging pulse, $g(t)$, is propagated using element e_i. Reflected signals are recorded using all of the E elements making up the receive aperture.

Let $s_p(i, j, t), \quad i \in \mathbb{N}_0, j \in \{0, 1, \ldots, E-1\}$ represent a *point impulse response*, or the response during the ith acquisition interval of a transducer element located at $(x[j], 0, 0)$ to a unit impulse transmitted from another transducer element located at $(x[e_i], 0, 0)$ and re-

flected from a point-scatterer with back-scattering coefficient σ_p and spatial coordinates $\vec{s}_p[i] = (x_p[i], y_p[i], z_p[i])$. Assuming a non-attenuating medium and ideal transducer elements with transmit and receive impulse responses $\delta(t)$, this may be written as:

$$s_p(i,j,t) = \sigma_p \delta\left(t - \tau_p[i,j,e_i]\right) \tag{6.2}$$

where $\tau_p[i,j,e]$ represents the bi-directional propagation delay:

$$\tau_p[i,j,e] = \frac{\sqrt{(x_p[i]-x[e])^2 + y_p[i]^2 + z_p[i]^2} + \sqrt{(x_p[i]-x[j])^2 + y_p[i]^2 + z_p[i]^2}}{c} \tag{6.3}$$

Using an imaging pulse, $g(t)$, and non-ideal transducer elements with transmit and receive impulse responses $a_t(t)$ and $a_r(t)$, respectively, (6.2) becomes:

$$\begin{aligned} r_p(i,j,t) &= g(t) * a_t(t) * \sigma_p \delta\left(t - \tau_p[i,j,e_i]\right) * a_r(t) \\ &= g(t) * a_{tr}(t) * s_p(i,j,t) \end{aligned} \tag{6.4}$$

where $a_{\text{tr}}(t)$ represents the combined response of the transmitting and receiving elements.

Modelling the tissue as a collection of point scatterers and applying the Born approximation, i.e. assuming the intensity of the scattered field is very low in comparison to the incident field and ignoring secondary scattering, the received signal, $r(i,j,t)$, may be approximated as the sum of individual point scatterer reflections:

$$\begin{aligned} r(i,j,t) &= \sum_p \sigma_p r_p(i,j,t) \\ &= g(t) * a_{tr}(t) * \sum_p \sigma_p s_p(i,j,t) \\ &= g(t) * a_{tr}(t) * s(i,j,t) \end{aligned} \tag{6.5}$$

where $s(i,j,t)$ is the lumped scattering impulse response of the medium using receiving element j during the ith acquisition interval:

$$s(i,j,t) = \sum_p \sigma_p \delta\left(t - \tau_p[i,j,e_i]\right) \tag{6.6}$$

6.2.2 Code Filtering and Beam-Forming

Received signals are compression-filtered prior to beam-formation. The filters used for the various signal types were generated using the methods described in Section 4.4. The remainder of this section describes the process for a system using binary-phase coded pulses in order to lead into the discussion of complementary-coded imaging in Section 6.3. As described in Chapter 3.2, binary-phase coded pulses may be decomposed as the convolution of a modulation sequence and a basis function, $g(t) = c(t) * b(t)$, and filtered using a time-reversed version of the modulation sequence, $c(T-t)$. Using (6.23), the filter output, $r_c(i,j,t) = c(T-t)*r(i,j,t)$ may be written:

$$\begin{aligned} r_f(i,j,t) &= c(T-t) * g(t) * a_{tr}(t) * s(i,j,t) \\ &= c(T-t) * c(t) * b(t) * a_{tr}(t) * s(i,j,t) \\ &= c_{xx}(t) * b_{tr}(t) * s(i,j,t) \end{aligned} \tag{6.7}$$

where $b_{tr}(t)$ represents the convolution of $b(t)$ and $a_{tr}(t)$ and $c_{xx}(t)$ is the auto-correlation sequence of $c(t)$. After each acquisition interval, the compression-filtered signals r_f are beam-formed into an L-line B-mode image, $r_{bf}(i,l,t) \quad l \in \{1,\ldots,L\}$.

$$r_{bf}(i,l,t) = \sum_j w_a(e_i,j,l,t) r_f(i,j,t-\tau_f(e_i,j,l,t)) \tag{6.8}$$

where $w_a(e_i,j,l,t)$ and $\tau_f(e_i,j,l,t)$ represent the apodisation weights and focusing delays as functions of the transmitting and receiving element indices, image line number and time/depth (to allow for dynamic receive focusing). Using a fixed focus and apodisation window, (6.8) becomes:

$$\begin{aligned} r_{bf}(i,l,t) &= \sum_j w_a[e_i,j,l] r_f(i,j,t-\tau_f[e_i,j,l]) \\ &= \sum_j w_a[e_i,j,l] * c_{xx}(t) * b_{tr}(t) * s(e_i,j,t-\tau_f[e_i,j,l]) \\ &= c_{xx}(t) * b_{tr}(t) * \sum_j w_a[e_i,j,l] * s(i,j,t-\tau_f[e_i,j,l]) \\ &= c_{xx}(t) * b_{tr}(t) * s_{bf}(i,l,t) \end{aligned} \tag{6.9}$$

where $s_{bf}(i,l,t)$ represents the scattering function of the medium including the effects of beamformation:

$$s_{bf}(i,l,t) = \sum_{j} w_a[e_i,j,l] * s(i,j,t-\tau_f[e_i,j,l]) \tag{6.10}$$

Unlike (6.8), the expressions in (6.9) and (6.10) are linear and time-invariant, facilitating the development of models for motion and compensation that follow.

6.2.3 Aperture Synthesis

Any E time-adjacent L-images will consist of a single L-image acquired using each of the E elements in the transmit aperture. The apodisation weights and time-delays required for transmit focusing were already applied in (6.9) along with those for receive focusing, allowing the transmit aperture to be synthesised simply by adding these L-images. Without aperture compensation, the synthetic aperture image $q_u(i,l,t)$ may be written:

$$\begin{aligned} q_u(i,l,t) &= \sum_{e=1}^{E} r_{bf}(i-E+e,l,t) \\ &= c_{xx}(t) * b_{\text{tr}}(t) * \sum_{e=1}^{E} s_{bf}(i-E+e,l,t) \end{aligned} \tag{6.11}$$

The effective scattering function for a single scatterer imaged using the synthesised aperture is a combination of those for each combination of transmit and receive apertures. If the scatterer positions are fixed between acquisition intervals, $s_{bf}(i,l,t) = s_{bf}(e_i,l,t) \quad \forall i$ and (6.11) simplifies to:

$$q_u(l,t) = c_{xx}(t) * b_{\text{tr}}(t) * \sum_{e=1}^{E} s_{bf}(e,l,t) \tag{6.12}$$

In this situation, the individual point-scattering-functions' (PSF) centres will coincide and their combined PSF will have a higher main-lobe and less pronounced side-lobes than the individual PSFs. If the scatterers move between acquisitions, the centres will no longer coincide exactly and the contrast and resolution of the synthetic aperture image will be reduced.

As with the complementary-coded imaging in Chapter 5, motion compensation may be used to maintain the subjective quality of the synthetic aperture image. A slightly different approach to motion estimation is required in this context, however, as L-images acquired using different transmitting elements exhibit low correlation due to differences in their point-spread functions,

as reported in [69]. As a result, they aren't sufficiently correlated for accurate motion estimation. The simple expedient adopted here is to perform the alignment of NL-images based on the average of estimates of τ_i^{i-E} and τ_{i+1}^{i+1-E}, which cover a time period extending one acquisition interval beyond either end of the aperture synthesis interval.

$$\hat{\tau}_i^j = \frac{j-i}{E}(\tilde{\tau}_i^{i-E} + \tilde{\tau}_{i+1}^{i+1-E}),\ i-E < j \leq i \tag{6.13}$$

Letting $m_{cc}(i,e,l,t)$ denote the outputs of the aperture compensation block:

$$m_{cc}(i,e,l,t) = r_{bf}(i-E+e,l,t-\hat{\tau}_i^{i-E+e}) \tag{6.14}$$

The compensated synthetic transmit aperture image is then:

$$\begin{aligned} q_c(i,l,t) &= \sum_{e=1}^{E} m_{cc}(i,e,l,t) \\ &= c_{xx}(t) * b_{\text{tr}}(t) * \sum_{e=1}^{E} s_{bf}(i-E+e,l,t-\hat{\tau}_i^{i-E+e}) \end{aligned} \tag{6.15}$$

This solution improves the alignment of the individual sub-aperture PSFs but doesn't account for any effects of motion on their geometry. It is assumed that this is negligible for the small displacements involved. The resulting composite PSF provides better contrast and resolution than in the uncompensated case, but may display less symmetry than that obtained in the absence of motion.

6.3 Complementary Coded STA Imaging

To perform a full complementary-coded synthetic transmit aperture scan, each of a set of N coded pulses must be transmitted through all E elements of the aperture. This may be accomplished by transmitting all N codes of the complementary set through each element in turn over E *code-cycles*, each of duration $T_c = NT_r$, or by performing a full aperture scan with each code of the set in turn over N aperture-cycles, each of duration T_a. Throughout this chapter, the former strategy will be referred to as *code-cycle scanning* and the latter as *aperture-cycle scanning*. In either case, the image data is collected over a full *scan-cycle* of duration $T_S = NET_r$.

There are advantages and disadvantages to both scanning strategies. In a code-cycle scanning

system, distinct sets of motion estimates are required for compensation of complementary L-images and for compensated aperture synthesis. As complementary L-images using the same element are acquired during time-adjacent acquisition intervals, however, the effects of motion on complementary side-lobe cancellation are minimised and coding compensation may arguably be dispensed with. In an aperture-cycle scanning system, the same velocity estimates are used for motion compensation of complementary-coded L-images and for motion compensation during aperture synthesis. The time-resolution of the velocity estimates used for aperture synthesis is finer by a factor of N, and a new H-image may be formed after every acquisition interval rather than after every N acquisition intervals. A detailed description of an aperture-cycle scanning system is developed in Section 6.5, as this is the scenario in which the effects of motion on complementary coding are most severe. Code-cycle scanning is discussed briefly in Section 6.5.

6.4 Aperture-Cycle Scanning

The block diagram of a complementary-coded, aperture-cycle scanning synthetic aperture imaging system may be seen in Figure 6.2. During a every aperture cycle, one pulse of the complementary set is transmitted using each aperture element in turn. As with the generic STA system described in Section 6.2, any E time-adjacent L-images will include one L-image acquired using each element of the transmit aperture. In a complementary-coded system, however, these will usually have been acquired using two different pulses of the complementary set. Acquisitions using the same transmitting element occur E acquisition cycles apart. Any N time-adjacent L-images acquired using the same transmitting element or sub-aperture include one image acquired using each constituent pulse of the complementary set. The most recent L-image is combined recursively with those from the previous $N-1$ acquisitions using the same element to form a low-resolution image with increased coding gain and lower side-lobes, which will be referred to as an *NL-image*. Similarly, any E time-adjacent NL-images will include one NL-image acquired using each element of the transmit aperture and may be used to synthesise a H-image – complementary coding and coding compensation are transparent from the point of view of aperture synthesis.

In a practical implementation, the motion compensation required for aperture synthesis and complementary L-image combination would be performed simultaneously and the signal flow would resemble that of the single-transmit code STA system shown in Figure 6.1. Separate

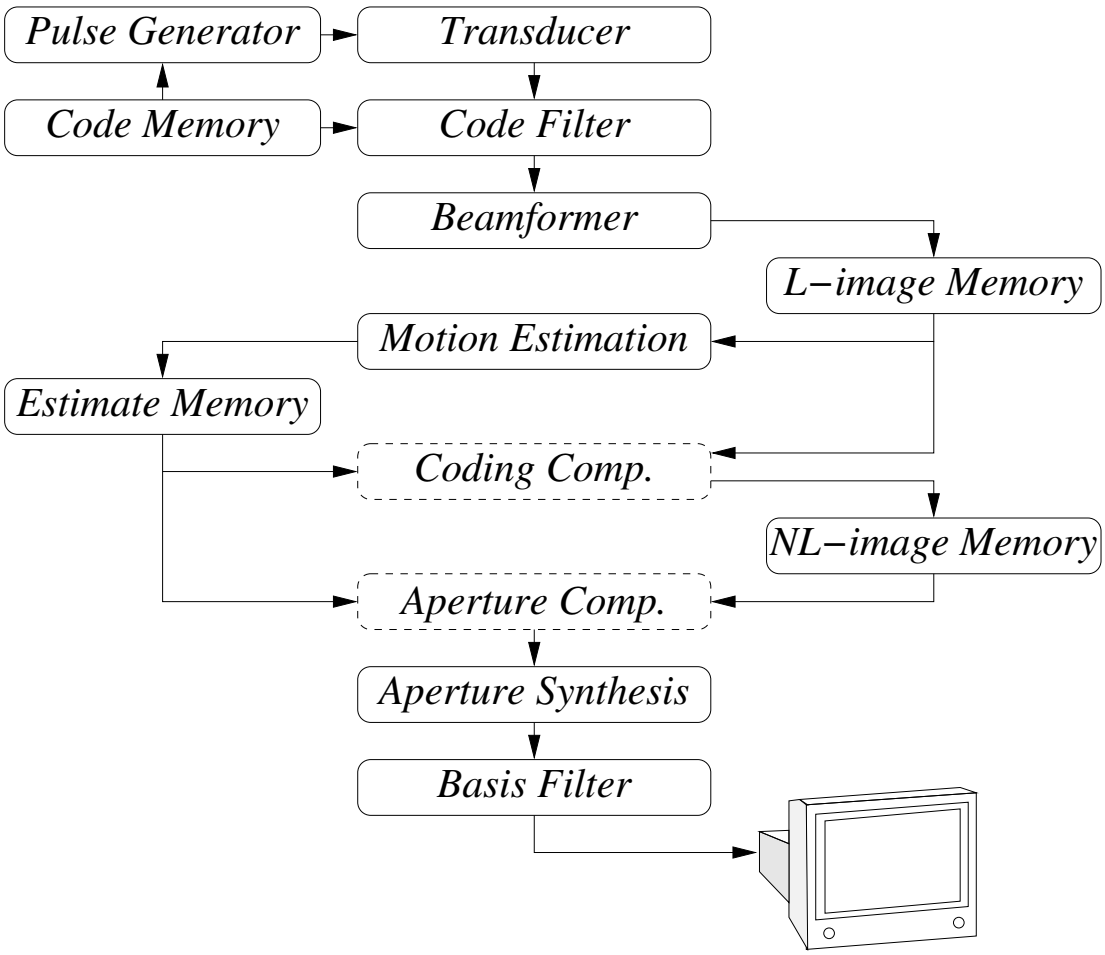

Figure 6.2: Signal flow: Aperture-cycle scanning

compensation stages have been adopted here to facilitate a clearer description of the system. The first, which will be referred to as *coding compensation*, aims to compensate for the effects of motion on side-lobe cancellation in the sets of L-images acquired using different codes of a complementary set and the same transmitting transducer element(s). The second, which will be referred to as *aperture compensation*, compensates for the effects of motion on aperture synthesis and is identical to that used in the single-transmit code STA system described in Section 6.2.

In order to describe the two compensation stages clearly, it is convenient to define a number of indices in addition to the element and acquisition interval indices introduced in Section 6.2. The *code index*, $o_i \in \{0, 1, ..., N-1\}$ indicates which code of the complementary set is being transmitted during a particular acquisition interval. In an aperture-cycle scanning system, each code is transmitted in turn for a full aperture-cycle and it proves convenient to define an *aperture-cycle index*, $m_i \in \mathbb{N}_0 \forall i$. These may be defined as follows, with $\%$ indicating the modulo operation as before:

$$\begin{aligned} o_i &= (\frac{i - e_i}{E})\%N \\ m_i &= \frac{i - e_i}{E} \end{aligned} \tag{6.16}$$

It is clear from (6.16) that o_m, the index of the coded pulse being transmitted during the mth aperture-cycle, is:

$$o_m = m\%N \tag{6.17}$$

and that:

$$i = m_i E + e_i \tag{6.18}$$

6.4.1 Transmit Coding

Consider an E-element transducer array with elements located at $(x[e], 0, 0), \quad 0 \leq e \leq (E-1)$. Let $g_{\text{cpc}}(n, t)$ represent a set of complementary-coded imaging pulses, as defined in (3.37). The individual signals of the set are transmitted from each of E elements in the synthetic transmit aperture in a repeating series such that $g_m(m, t)$, the signal transmitted during the mth

aperture-cycle is:

$$\begin{aligned} g_m(m,t) &= g_{\text{cpc}}(m\%N,t) \\ &= g_{\text{cpc}}(o_m,t) \\ &= c_c(o_m,t) * b(t) \end{aligned} \tag{6.19}$$

Combining (6.19) and (6.16), the signal transmitted during the ith acquisition interval, $g(i,t)$, is:

$$\begin{aligned} g(i,t) &= g_m(\tfrac{i-e_i}{E},t) \\ &= g_{\text{cpc}}(\tfrac{i-e_i}{E}\%N,t) \\ &= g_{\text{cpc}}(o_i,t) \end{aligned} \tag{6.20}$$

Using (3.37), define $c_m(m,t)$ and $c(i,t)$ as the modulation sequences (see Section 3.2.2) associated with $g_m(m,t)$ and $g(i,t)$:

$$c(i,t) = c_m(m_i,t) = c_c(m_i\%N,t) = c_c(o_i,t) \tag{6.21}$$

Their associated auto-correlation sequences, $c_{\text{mm}}(m,t)$ and $c_{\text{ii}}(i,t)$, and those of the set of complementary coded pulses, $c_{\text{oo}}(o,t)$, are related as follows:

$$\sum_{n=1}^{N} c_{ii}(i \pm nE,t) = \sum_{n=1}^{N} c_{mm}(m_i \pm n,t) = \sum_{n=1}^{N} c_{oo}(n,t) \; = NL\delta(t) \tag{6.22}$$

6.4.2 Received Signals

Using a signal of the form of (6.20) in (6.5), the received signal during the ith acquisition interval, $r(i,j,t)$, becomes:

$$\begin{aligned} r(i,j,t) &= \sum_p \sigma_p r_p(i,j,t) \\ &= g(i,t) * a_{tr}(t) * \sum_p \sigma_p s_p(i,j,t) \\ &= g(i,t) * a_{tr}(t) * s(i,j,t) \end{aligned} \tag{6.23}$$

where $s(i,j,t)$ is the lumped scattering impulse response of the medium using receiving element j during the ith acquisition interval as defined in (6.6).

6.4.3 Code Filtering and Beam-Forming

Received signals are compression-filtered using $c(i, T-t)$, a time-reversed version of the modulation sequence matching the coded pulse. Using (6.23) and (6.20), the filter output, $r_f(i,j,t) = c(i,T-t) * r(i,j,t)$ may be written:

$$r_f(i,j,t) = c_{ii}(i,t) * b_{tr}(t) * s(i,j,t) \tag{6.24}$$

where $b_{tr}(t)$ represents the convolution of $b(t)$ and $a_{tr}(t)$, as before. Using (6.9) and (6.10), the beam-formed L-image lines, $r_{bf}(i,l,t)$, become:

$$r_{bf}(i,l,t) = c_{ii}(i,t) * b_{tr}(t) * s_{bf}(i,l,t) \tag{6.25}$$

6.4.4 Complementary Code Combination and Compensation

In the absence of motion compensation, the sum of N time-adjacent complementary L-image lines acquired using the same element is:

$$\begin{aligned} m_u(i,l,t) &= \sum_{n=1}^{N} r_{bf}(i-[N-n]E,l,t) \\ &= \sum_{n=1}^{N} c_{ii}(i-[N-n]E,t) * b_{\text{tr}}(t) * s_{bf}(i-[N-n]E,l,t) \\ &= b_{\text{tr}}(t) * \sum_{n=1}^{N} c_{mm}(m_i+n,t) * s_{bf}(i-[N-n]E,l,t) \end{aligned} \tag{6.26}$$

If the region within the beam is stationary between aperture-cycles:

$$s_{bf}(i+aE,l,t) = s_{bf}(i,l,t) \quad \forall\{i,a\} \in \mathbb{N}_0 \tag{6.27}$$

i.e. as L-images from acquisition intervals separated by integer multiples of E are acquired using the same transmitting element or sub-aperture:

$$s_{bf}(i,l,t) = s_{bf}(e_i,l,t) \quad \forall i \in \mathbb{N}_0 \tag{6.28}$$

Combining (6.26) and (6.27):

$$\begin{aligned} m_u(i,l,t) &= b_{\text{tr}}(t) * s_{bf}(e_i,l,t) * \sum_{n=1}^{N} c_{mm}(m_i+n,t) \\ &= NL\delta(t-T) * b_{\text{tr}}(t) * s_{bf}(e_i,l,t) \end{aligned} \tag{6.29}$$

Movement of a point scatterer between acquisition intervals results in a change in the propagation time for signals reflected from it. For a given point, p, in the absence of attenuation, the point impulse responses during acquisition intervals i_a and i_b are identical but for a time shift:

$$\begin{aligned} s_p(i_b,j,t) &= \sigma_p \delta\left(t - \tau_p[i_a,j] - \Delta\tau_p[i_a,i_b,j]\right) \\ &= s_p(i_a,j,t-\Delta\tau_p[i_a,i_b,j]) \end{aligned} \tag{6.30}$$

where $\Delta\tau_p[i_a,i_b,j]$ is the change in round-trip time due to a change in scatterer position between the i_ath and i_bth acquisitions.

$$\Delta\tau_p[i_a,i_b,j] = \tau_p[i_b,j] - \tau_p[i_a,j] \tag{6.31}$$

The same cannot be said of $s(i_a,j,t)$ and $s(i_b,j,t)$, as $\Delta\tau_p$ is a function of the point/transducer geometry as well as the point displacement between acquisition intervals. Combining (6.6) and (6.30):

$$s(i_b,j,t) = \sum_p s_p\left(i_a,j,t-\Delta\tau_p[i_a,i_b,j]\right) \tag{6.32}$$

In order for motion compensation to be possible, it is necessary to approximate the effects of motion as a time-shift. This is not reasonable for the unfocused scatterer functions. After focusing and apodisation, however, the relationship between $s_{bf}(i_a,l,t)$ and $s_{bf}(i_b,l,t)$ may be written as:

$$s_{bf}(i_b,l,t) \cong s_{bf}(i_a,l,t-\tau_a^b) \tag{6.33}$$

The approximate relationship in (6.33) relies on the assumptions that the motion within a focal cell is homogeneous and predominantly in the direction of the beam axis, and that the same transmitting element was used during both acquisition intervals, i.e. $i_b = i_a \pm kE, \quad \forall k \in \mathbb{N}_0$. This assumption is reasonably strong in STA imaging: as individual L-images are acquired using unfocused transmissions, the beam-width is comparatively high (remembering from Chapter 2 that beam-width is inversely related to aperture width) and increases with depth.

Define $r_s(i,n,l,t)$ as reference complementary L-image lines and $m_s(i,l,t)$, their sum, as reference NL-image lines. Note that the identity $c_m(m+N,t) = c_m(m,t)$ has been used to simplify these somewhat.

$$r_s(i,n,l,t) = c_{mm}(m_i+n,t) * b_{\text{tr}}(t) * s_{bf}(i,l,t) \tag{6.34}$$

$$\begin{aligned} m_s(i,l,t) &= \sum_{n=1}^{N} r_s(i,n,l,t) \\ &= NL\delta(t-T) * b_{\text{tr}}(t) * s_{bf}(i,l,t) \end{aligned} \tag{6.35}$$

Combining Equation (6.26) with Equations (6.33) and (6.34) allows the sum of uncompensated filter outputs to be written as:

$$\begin{aligned} m_u(i,l,t) &= \sum_{n=1}^{N} r_s(i,n,l,t-\tau_i^{i-[N-n]E}) \\ &= b_{\text{tr}}(t) * \sum_{n=1}^{N} c_{mm}(m_i+n,t) * s_{bf}(i,l,t-\tau_i^{i-[N-n]E}) \end{aligned} \tag{6.36}$$

Let $r_c(i,n,l,t), \quad 1 \le n \le N$ represent the outputs of the coding compensation block after the ith acquisition interval, with $r_c(i,N,l,t) = r_{bf}(i,l,t)$. If $\tilde{\tau}_a^b$ represents the estimated change in round-trip time due to motion between the a^{th} and b^{th} emissions and ϵ_a^b the estimate error, $\epsilon_a^b = \tau_a^b - \tilde{\tau}_a^b$,

$$\begin{aligned} r_c(i,n,l,t) &= r_{bf}(i-[N-n]E, t-\tilde{\tau}_i^{i-[N-n]E}) \\ &= r_s(i,n,l,t+\epsilon_i^{i-[N-n]E}) \end{aligned} \tag{6.37}$$

The sum of compensated outputs is then:

$$\begin{aligned} m_c(i,l,t) &= \sum_{n=1}^{N} r_c(i,n,l,t) \\ &= b_{\text{tr}}(t) * \sum_{n=1}^{N} c_{mm}(m_i+n,t) * s_{bf}(i,l,t+\epsilon_i^{i-[N-n]E}) \end{aligned} \tag{6.38}$$

The role of the motion compensation block is to minimise the $\epsilon_i^{i-[N-n]E}$ term in (6.38) and ensure that the sum of compensated outputs $m_c(i,l,t)$ approaches $m_s(i,l,t)$. Taking the limit

as ϵ approaches 0:

$$\begin{aligned}\lim_{\epsilon\to 0} m_c(i,l,t) &= NL\delta(t-T) * b_{\text{tr}}(t) * s_{bf}(i,l,t) \\ &= m_s(i,l,t)\end{aligned} \tag{6.39}$$

This is accomplished using a segmented motion-compensation algorithm identical to that described in Chapter 5.

6.4.5 Aperture Synthesis

In an aperture-cycle scanning system, the process of aperture compensation is unaffected by the introduction of complementary coding. The only difference is that the inputs to the aperture synthesis stage are now the E most recent outputs of the coding compensation block, $m_c(i,l,t)$, rather than the most recently formed L-images. Without aperture compensation, the synthetic aperture image $q_u(i,l,t)$ may be written:

$$\begin{aligned}q_u(i,l,t) &= \sum_{e=1}^{E} m_c(i-E+e,l,t) \\ &= NL\delta(t-T) * b_{\text{tr}}(t) * \sum_{e=1}^{E} s_{bf}(i-E+e,l,t)\end{aligned} \tag{6.40}$$

The estimates of τ_i^{i-E} and τ_{i+1}^{i+1-E} required for aperture compensation have already been generated during coding compensation and may be inserted in (6.13) to obtain $\hat{\tau}_i^j$. The outputs of the aperture compensation block, $m_{cc}(i,a,l,t)$, may be written:

$$m_{cc}(i,e,l,t) = m_c(i-E+e,l,t-\hat{\tau}_i^{i-E+e}) \tag{6.41}$$

and the compensated synthetic transmit aperture image becomes:

$$\begin{aligned}q_c(i,l,t) &= \sum_{e=1}^{E} m_{cc}(i,e,l,t) \\ &= NL\delta(t-T) * b_{\text{tr}}(t) * \sum_{e=1}^{E} s_{bf}(i-E+e,l,t)\end{aligned} \tag{6.42}$$

6.4.6 Simulation Results

The simulation results presented here all used a 64-element linear array transducer with a 4MHz centre frequency and a fractional bandwidth of 66%. The sampling frequency for the simulated ultrasound system was set to 100MHz, 25 times the centre frequency, as was that of the Field II simulator. This value was chosen to be an integer multiple of the transducer centre frequency to minimise sampling effects. Frequency-dependent attenuation of 0.5 dB/MHz/cm was used during simulation, and Gaussian white noise was added to the simulated data prior to filtering and beam-formation. The noise level was set at -40dB relative to the maximum received signal level for a single transducer element. In the sequential scan imaging simulations reported in previous chapters, noise was added after beam-formation and the noise levels are not directly comparable as a result.

All of the simulations used a Hanning apodisation weighting, dynamic focusing and an F-number of 1 on receive. A rectangular apodisation window was used during transmit aperture synthesis. Compression filtering was performed prior to delay-sum beam-forming. As with the sequential-scan simulations reported in Chapters 4 and 5, log-linear time-gain control was applied to the filtered signals immediately prior to envelope detection and generation of the B-mode images.

Each figure consists of a set of simulated synthetic transmit aperture B-mode images obtained using a Golay code pair, a linear FM signal and a uncoded pulse, as well as a plot of the central lines of the Golay and FM images. The images were obtained using a simulated point phantom, consisting of 10 point scatterers placed 10mm apart along the central axis of the transducer. The uncoded pulse used throughout was a single-cycle square wave of duration 0.25 μs, while the Golay-coded pulses and LFM signals were of either 4μs or 10μs duration. The ramp evident in the noise floor of the centre-line plots is due to the application of log-linear time-gain control. The poor lateral resolution of the B-mode images in regions close to the transducer is due to the relatively simple aperture synthesis algorithm used, in which the width of the synthetic transmit aperture was fixed and equal weight was given to each of its constituent elements. As mentioned in Section 6.1, this was an exploratory piece of work and time constraints prevented it being revisited in light of subsequent research developments.

Figures 6.3 and 6.4 were generated without simulated motion and are provided for reference purposes. The SNR benefits and improved axial resolution of the Golay-coded pulses are

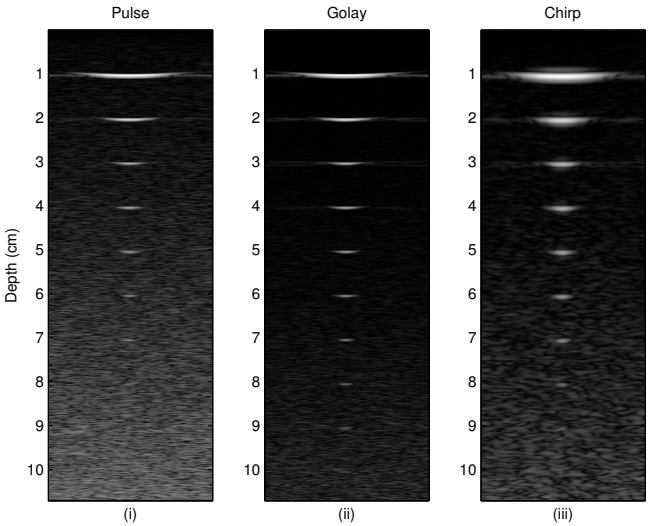

(a) B-mode images

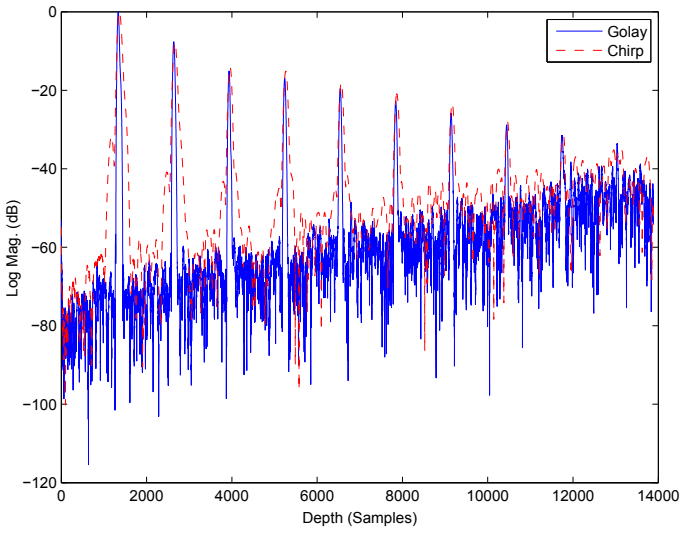

(b) Envelope of central image lines

Figure 6.3: Aperture-cycle scanning: No motion, code length 16 (4μs)

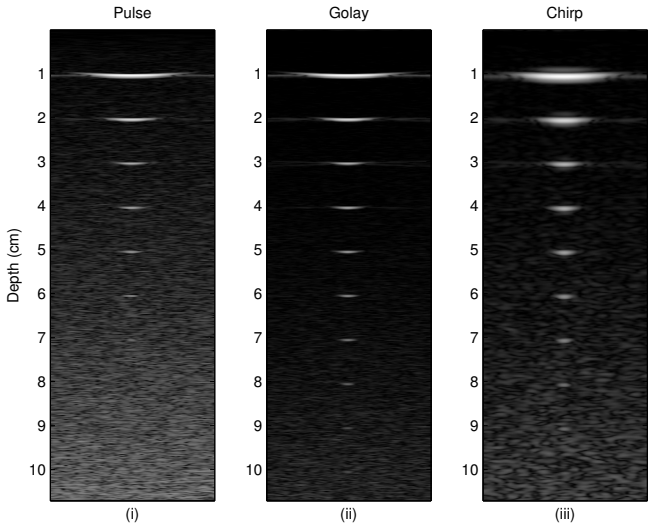

(a) B-mode images

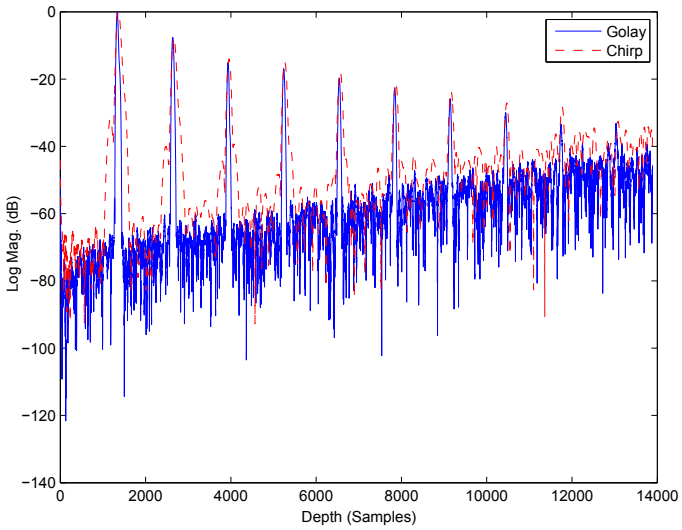

(b) Envelope of central image lines

Figure 6.4: Aperture-cycle scanning: No motion, code length 40 (10μs)

clearly discernible in the B-mode images in Figures 6.3(a) and 6.4(a). Examining Figures 6.3(b) and 6.4(b), the increased SNR gain of the Golay-coded pair is evident from a comparison between its noise floor and that of the chirp and transmit-aperture synthesis does not appear to affect complementary side-lobe cancellation. The increased resistance of binary-phase coded pulses to depth effects described in Chapter 4 is not clearly in evidence here, as these effects are highly frequency dependent and the imaging frequency of 4 MHz used during the synthetic aperture simulations was significantly lower than the 7.5 MHz used in those described in earlier chapters.

The introduction of simulated motion does not adversely affect the imaging characteristics of the LFM and uncoded sinusoidal pulses, as shown in Figures 6.5 and 6.6, but movement between adjacent Golay pulse emissions results in high side-lobes. These cause the severe blurring in the Golay-coded B-mode images of Figures 6.5(a) and 6.6(a). Examination of Figures 6.5(b) and 6.6(b) reveals that these side-lobes occur approximately 20dB below the main-lobe peak.

Motion compensation proves effective in reducing these side-lobes significantly, as evidenced by Figures 6.7 and 6.8. Examination of the centre-line envelope plots in Figures 6.7(b) and 6.8(b) reveals that the envelope of the motion-compensated Golay code pair exhibits lower side-lobe levels than the LFM signals at both signal lengths. The severe blurring evident in the Golay-coded B-mode images of Figures 6.5(a) and 6.6(a) has been all but eliminated in Figures 6.7(a) and 6.8(a). Residual misalignment artefacts are visible towards the left- and right-most sections of the images at a depth of 1 cm – these are due to the use of a fixed transmit aperture and should be eliminated by the application of a more sophisticated aperture synthesis algorithm.

6.5 Code-Cycle Scanning

In a code-cycle scanning system, all N codes of the complementary set are transmitted through each element in turn over E *code-cycles*, each of duration $T_c = NT_r$. A new NL-image is formed after every code cycle, and E time-adjacent NL-images may be used to synthesise a H-image.

In a system of this type, the implementation of motion compensation is more complicated than in an aperture-cycle scanning system as a result of the altered order of acquisitions. Motion

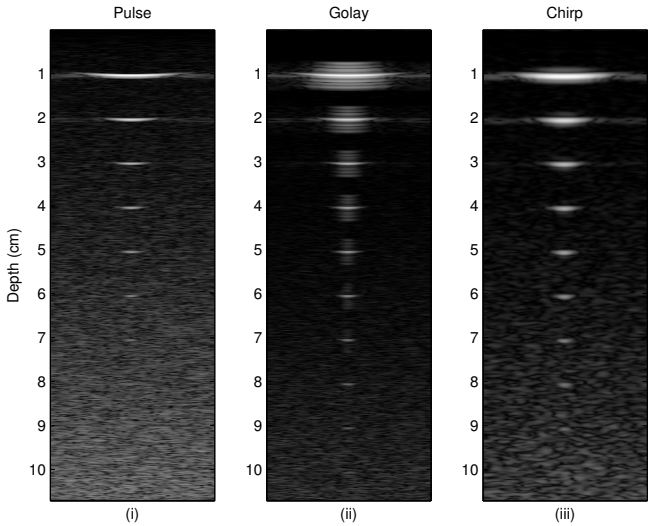

(a) B-mode images

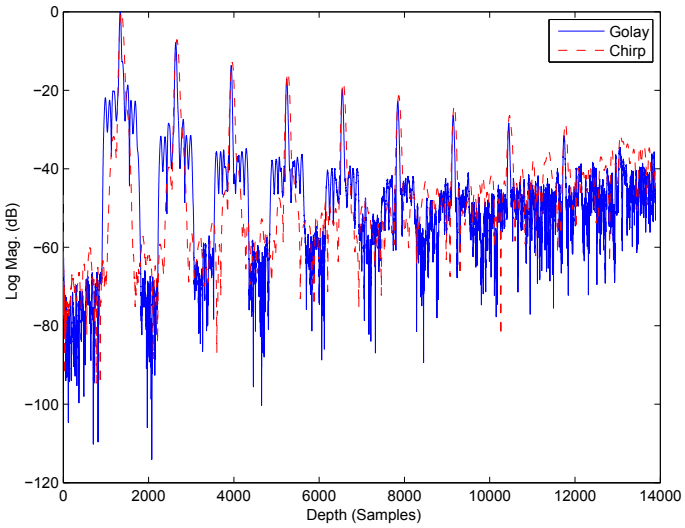

(b) Envelope of central image lines

Figure 6.5: Aperture-cycle scanning: Uncompensated motion, code length 16 (4μs)

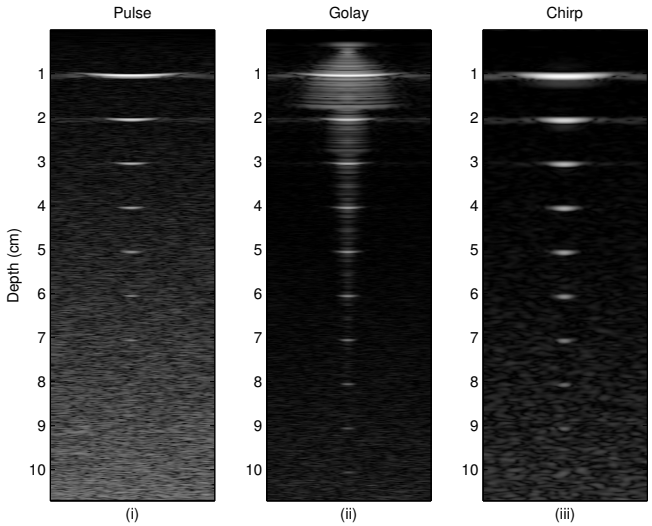

(a) B-mode images

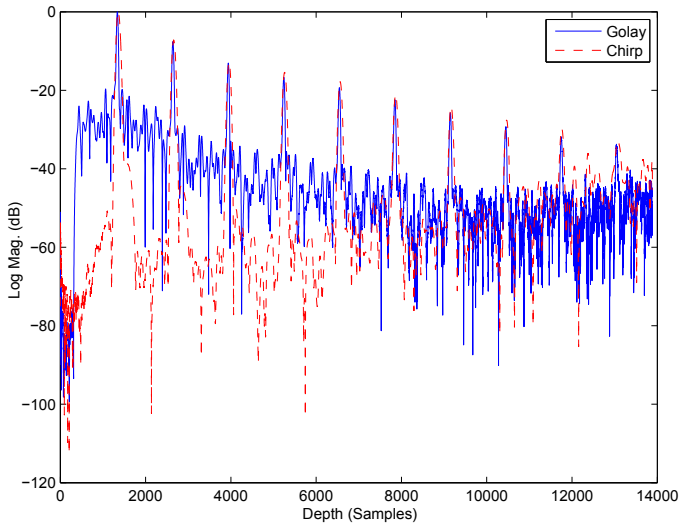

(b) Envelope of central image lines

Figure 6.6: Aperture-cycle scanning: Uncompensated motion, code length 40 (10μs)

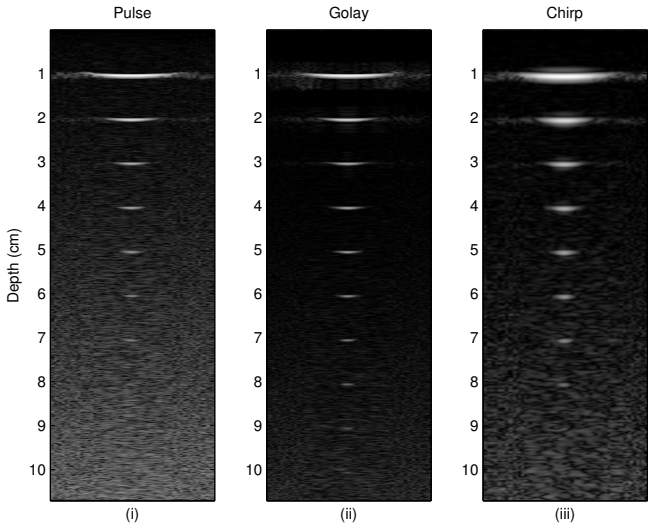

(a) B-mode images

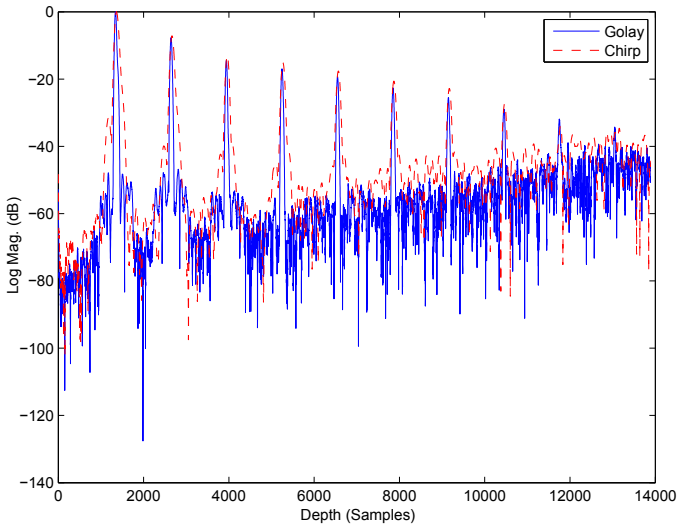

(b) Envelope of central image lines

Figure 6.7: Aperture-cycle scanning: Compensated motion, code length 16 (4 μs)

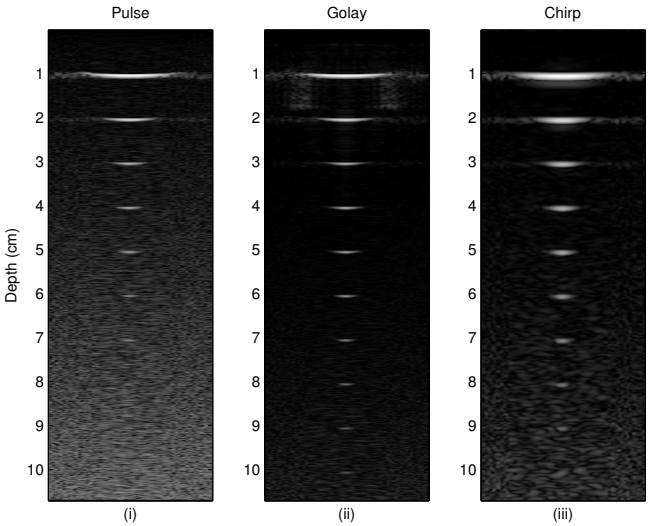

(a) B-mode images

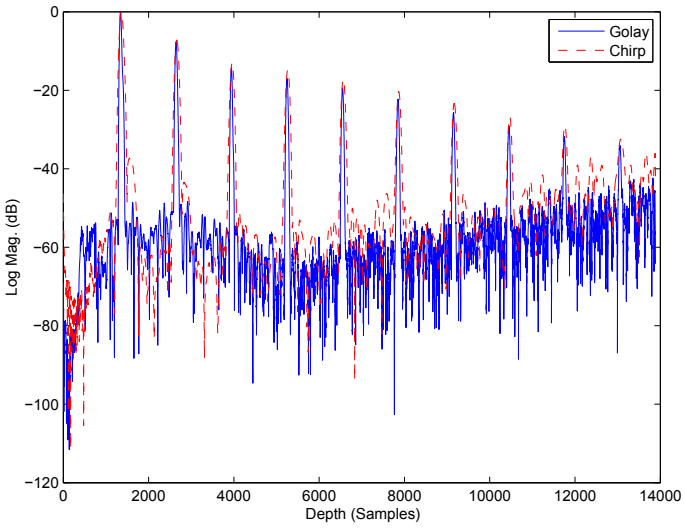

(b) Envelope of central image lines

Figure 6.8: Aperture-cycle scanning: Compensated motion, code length 40 (10μs)

estimates made using the complementary L-images acquired during each coding cycle provide high (temporal) resolution velocity data that may be used for coding compensation. There are gaps in this high-resolution data corresponding to the transitions between emitting elements. As a result, a second set of lower (temporal) resolution *aperture-motion estimates* is required for aperture compensation, as illustrated in Figure 6.9. An advantage of code-cycle scanning

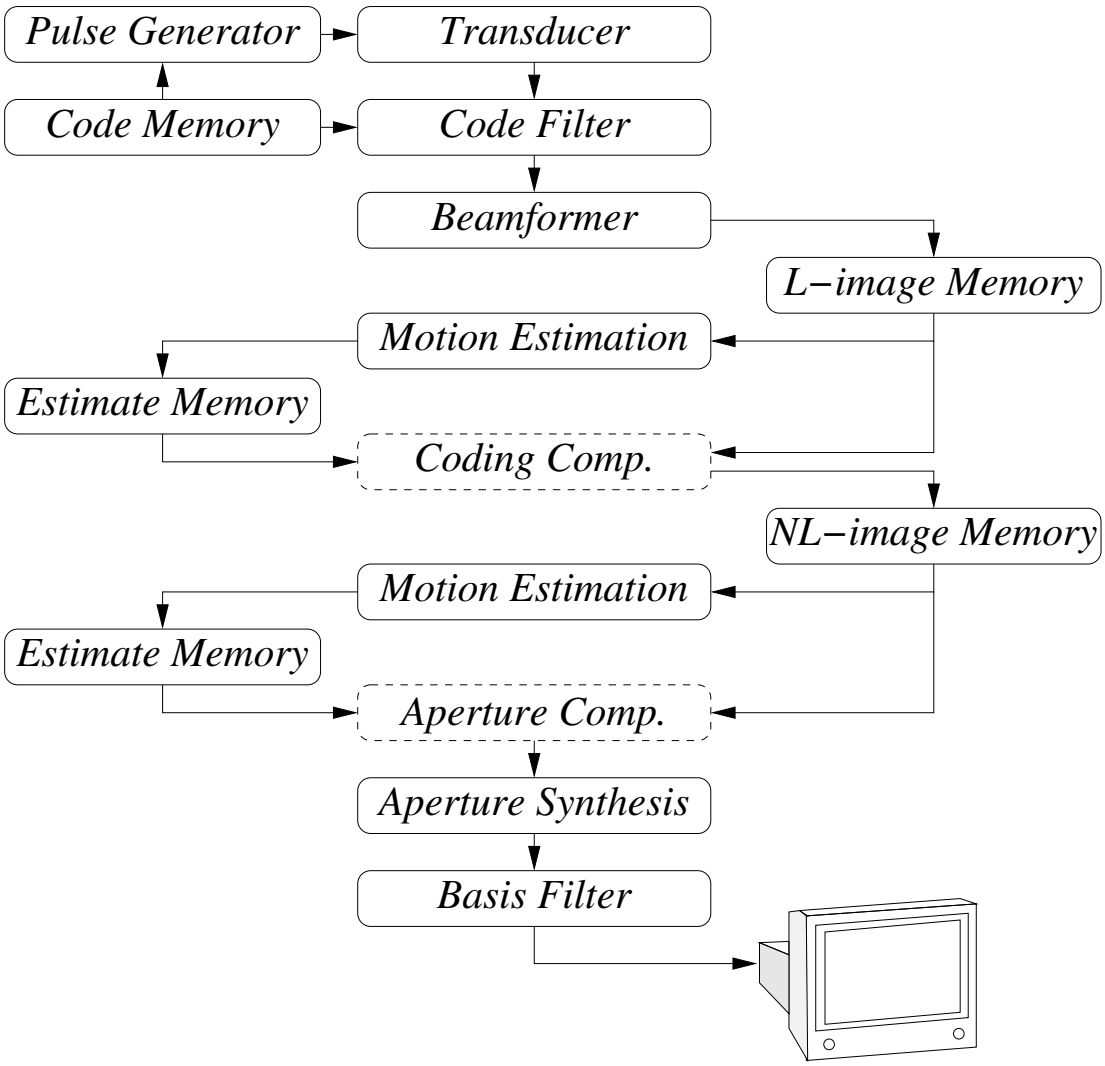

Figure 6.9: Signal flow: Motion-compensated code-cycle scanning

is that, foregoing recursive coding compensation, the serial emission of complementary pulses from each element will minimise the degree of misalignment to be compensated and reduce the occurrence of misalignment errors, which have the most visible impact on the quality of the synthetic image. It may be possible to dispense with coding compensation entirely, as illustrated in Figure 6.10, provided the intervals between complementary acquisitions are sufficiently short to

prevent the occurrence of severe misalignment side-lobes. Recursive aperture synthesis ensures that high frame-rates may be maintained without recursive coding compensation. The resolu-

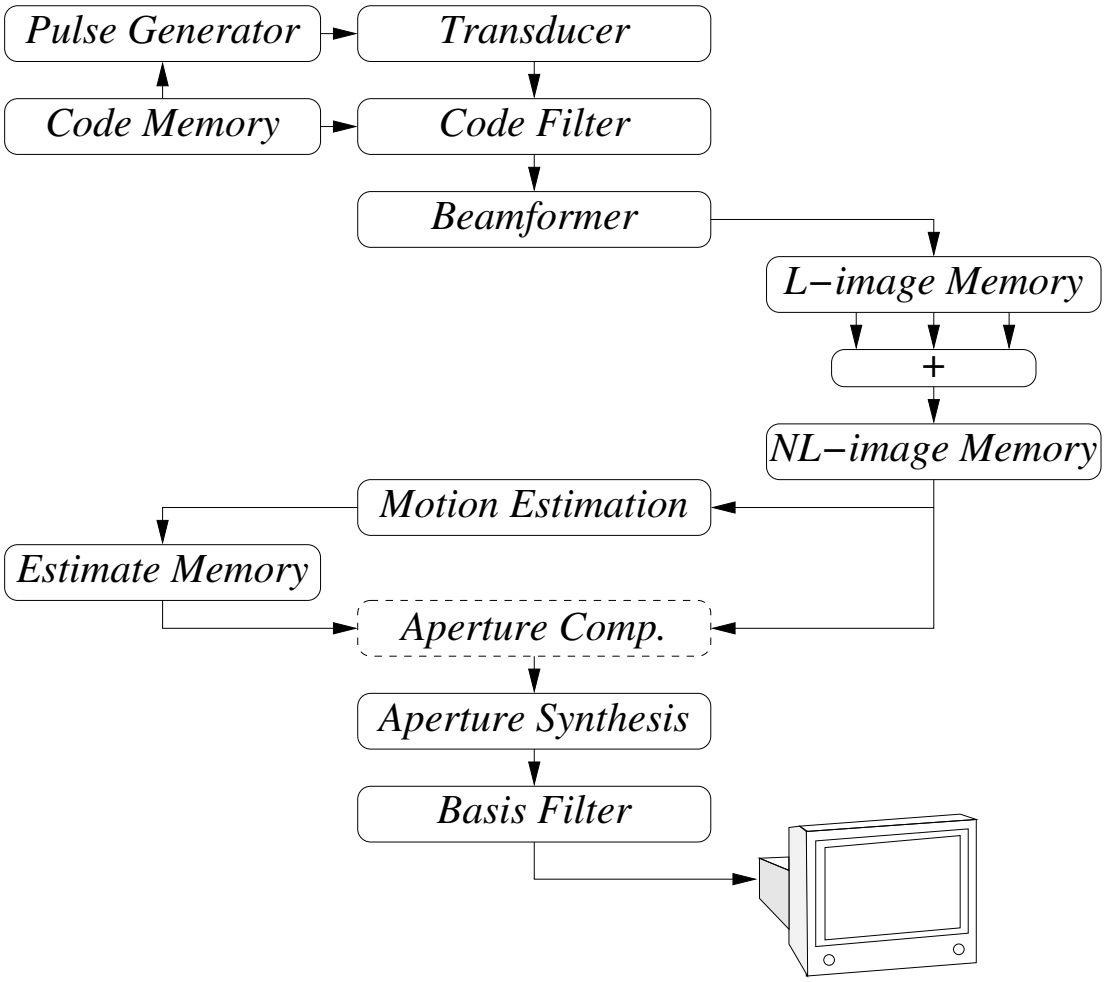

Figure 6.10: Signal flow: Simplified motion-compensated code-cycle scanning

tion of aperture-motion estimates is dictated by the time between adjacent coding cycles using the same transmitting element, i.e. NE acquisition intervals compared to the N acquisition intervals resolution of the aperture-cycle scanning system. As time-adjacent aperture-motion estimates are obtained using different elements of the transmit aperture, the variation in their associated point-scattering functions may introduce inconsistencies in adjacent synthetic aperture images formed using the estimates. Both of these issues could be circumvented by adding a pulse to each coding-cycle. This pulse would always be transmitted using the central element or elements of the transmit aperture and allow the formation of another set of velocity estimates, simultaneously increasing the temporal resolution of aperture-motion estimates and providing a consistent basis for aperture compensation.

6.6 Conclusions

The work presented in this chapter demonstrates some of the potential of complementary BPC pulses in synthetic transmit aperture imaging. Two different methods for complementary-coded STA imaging have been proposed. Both methods are suitable for full aperture synthesis using a series of low-resolution images acquired by emitting each of the coded pulses from every element of the transducer array individually, or for aperture synthesis using a sparse subset of the individual array elements. An uncoded or single-transmit coded STA imaging system could be readily adapted for aperture-cycle scanning at very little additional computational expense, as the motion estimates required for aperture synthesis may also be used for coding compensation. Code-cycle scanning minimises the effects of motion on complementary side-lobe cancellation but may require a more elaborate motion estimation strategy.

Chapter 7
Conclusions and Future Work

7.1 Conclusions

The research described in this thesis began with a broad remit: to identify areas in medical diagnostic ultrasound in which some material "improvement" could be made using coded signals. Initially, a period was spent reviewing the principles of ultrasonic fields, wave propagation, ultrasonic pulse-echo imaging and velocity estimation, the fruits of which are summarised in Chapter 2. Over the course of this review, it became apparent that attenuation and regulatory limits on peak intensity levels were two key factors limiting increases in the resolution and subjective "quality". Attenuation causes a depth-dependent reduction in signal-to-noise ratio, limiting the maximum depth at which clinically useful images may be obtained, while regulatory limits prevent signal-to-noise ratio from being increased directly by increasing transmitted signal power. These factors also limit image resolution, albeit indirectly. The size of a resolution cell is a function of signal centre frequency and fractional bandwidth. Increasing resolution by increasing pulse centre frequency, however, results in a rapid reduction in the maximum clinically useful imaging depth as the effects of attenuation are highly frequency dependent.

Both of these issues have been addressed using a variety of signal processing methods by a number of other authors. Pulse compression allows the duration of imaging pulses to be extended without reducing signal bandwidth, increasing pulse-average flux intensity while remaining within peak-intensity limits and thereby increasing SNR without adversely affecting the resolution characteristics of a system. This increase in SNR translates directly to an increase in the depth-in-tissue at which clinically useful images may be obtained. Alternatively, the increased SNR headroom can be traded off against the additional attenuation losses incurred by moving to higher imaging frequencies, facilitating an increase in resolution without a reduction in depth-of-imaging. A range of pulse-compression waveforms and filter design methods were discussed in Chapter 3, with reference to techniques current in the ultrasound literature and challenges particular to pulse compression in ultrasonic imaging.

A review of the literature on pulse-compression in medical diagnostic imaging revealed a range

of conflicting conclusions as to the relative merits of different signals and filters for imaging purposes. A variety of the more successful of these were implemented and compared using simulation tools as well as experimental facilities provided by our research partners. In simulation, point phantoms were used to quantify the envelope characteristics of the various signals and filters while more complex speckle phantoms were used to assess the subjective image quality. The results of these comparisons were described in Chapter 4. It became clear that, while considerable research effort had been expended previously on methods to reduce filter side-lobe levels, relatively little consideration had been given to the effects of these methods on the compression characteristics of high-frequency modulated signals under frequency-dependent attenuation. Measures commonly used to reduce the side-lobes of frequency-modulated signals were found to reduce the magnitude of the low-frequency signal components least affected by attenuation, resulting in a depth-dependent reduction in coding gain, i.e. the SNR advantages of coding were evident in the regions close to the transducer, where they were unnecessary, but not at depth, where they were most required. Binary discrete-phase coded signals, on the other hand, were found not to be affected by this issue due to their different time-frequency structure. They were also found to provide sharper axial resolution and have features allowing the costs of hardware implementation to be reduced.

Complementary binary-phase coded signals were shown to combine the strengths of binary-phase coding with ideal side-lobe performance. In simulated B-mode imaging at a centre frequency of 7.5 MHz, for example, a complementary BPC signal pair provides an approximately 30mm increase in imaging depth compared to LFM and NLFM pulses of the same duration. An additional consideration is that the sidelobe characteristics of complementary signals are not length dependent, whereas FM signals with time-bandwidth products of 50 or more are required in order to achieve side-lobe levels suitable for imaging purposes. Using complementary coded signals, however, an increased number of pulse emissions are required to form each image. This increases image acquisition time considerably, potentially reducing the frame-rate of an imaging system by a factor of two or more. Another potential obstacle to the adoption of complementary coded signals is that motion between complementary acquisitions can also degrade side-lobe performance significantly.

During the course of this simulation study, an issue was identified in an extremely widely used simulation tool that has serious implications for simulation studies using wide-band signals. Using complementary binary-phase coded pulses, the issue is manifested as side-lobes that ap-

pear to be due to aliasing and are eliminated or substantially reduced by appropriate filtering of signals prior to simulation. The issue does not affect band-limited analogue-phase modulated signals and appears to have influenced other published conclusions as to the suitability of complementary-coded pulses for imaging in the presence of high levels of attenuation.

In order to study motion effects, facilities for time-varying homogeneous and inhomogeneous (elastic) motion were added to the simulation environment. A novel algorithm was developed for motion-compensated complementary-coded ultrasonic imaging. It performs an interpolated re-alignment of complementary scan-lines on the basis of motion estimates obtained using the normalised cross-correlation method (or RF cross-correlator) described in Chapter 2. The method was designed primarily to reduce motion side-lobe artefacts but also allowed acquired data to be used recursively, eliminating the frame-rate reduction usually associated with complementary codes. In Chapter 5, simulation results were presented demonstrating the effects of per-scanline, or single-segment, motion compensation. The method was shown to be effective in the presence of homogeneous motion, but its performance was compromised when a wide range of velocities were present within a scan volume. This issue was successfully dealt with by dividing individual scan lines into multiple segments and compensating segments individually. A dual "mirrored" compensation structure was adopted in order to further reduce the effects of small degrees of misalignment due to partial compensation. These methods were shown to be very effective, reducing misalignment side-lobes to levels comparable with those obtained using single-transmit FM signals while maintaining the desirable resolution properties and robustness to attenuation of BPC signals. Subjective assessments of B-mode images of point and speckle phantoms indicate that mirrored multi-segment motion compensation is very effective in eliminating motion artefacts in images containing regions with both high and low concentrations of scatterers. Long pulse durations were found to reduce the efficacy of motion compensation in the presence of a significant spread of velocities, although comparatively short complementary signals can provide a useful increase in SNR as a complementary pair of BPC signals provides two or more times the coding gain of a single coded signal of similar bandwidth and duration.

The motion-compensated imaging algorithm was subsequently adapted for used in synthetic transmit aperture ultrasonic imaging. Complementary-coded imaging pulses are ideally suited to a system of this type as motion compensation is required during the synthesis of the transmit aperture, even in the absence of complementary coding, and the same velocity estimates

may be used for aperture synthesis and complementary side-lobe compensation, i.e. motion-compensated complementary coding may be adopted at the cost of very little additional computational overhead. A simulated synthetic transmit aperture imaging system was implemented using MATLAB and Field II, and results were presented demonstrating the success of the method in simulated synthetic transmit aperture imaging of moving point-phantoms. Two different methods for complementary-coded synthetic-aperture imaging were suggested, although time constraints prevented a full comparative evaluation of the two.

7.2 Future Work

Given appropriate facilities and more time, an experimental evaluation of some of the B-mode imaging results using a tissue-mimicking phantom would be very useful. The experimental facilities available during the course of this thesis research used single-element transducers that were designed for velocity estimation, non-destructive testing or materials characterisation, all inadequate to perform B-mode imaging. B-mode imaging facilities were available, but not ones that could be driven with coded signals. A logical progression of the work would be verification of the attenuation and motion compensation results reported in Chapters 4 and 5 using a research scanner capable of driving multi-element transducers with coded signals and providing access to unprocessed received signals for off-line analysis.

The results reported in Chapter 4 suggest that investigation of non-linear FM signals whose lowest frequency components occur at or about the temporal midpoint of the signal could prove interesting. Using signal-design methods current in the literature, these frequency components, which are the least affected by attenuation, are heavily suppressed by measures designed to reduce filter side-lobe levels. Also of interest would be a comparison of motion-compensated complementary-coded imaging with a system using binary-phase Barker codes and inverse "spiking" filters.

With regard to motion-compensated imaging, further investigation of the impact of various focusing and motion estimation parameters on the compensation process would seem to be called for, as observations of simulated results under a range of conditions suggest that focal settings have a small but appreciable influence on Golay side-lobe complementarity under heavy attenuation. It could also be useful to identify sets of complementary codes with optimal misalignment side-lobe characteristics for imaging purposes. The baseband 4-bit Golay code pair,

for example, exhibits misalignment side-lobes at $\frac{1}{2L}$ the level of the main-lobe, provided the degree of misalignment doesn't exceed the bit period. The number of code sets/pairs available to choose from increases with code length, and some time spent identifying the code pairs or sets of a particular length with these optimal Barker code-like side-lobe characteristics could be useful.

The synthetic aperture imaging results in Chapter 6 were generated some time before the sequential scan B-mode imaging results in Chapters 4 and used a lower pulse centre frequency. The signal and filter design procedures and focusing parameters were refined considerably subsequent to generation of the synthetic aperture results. Given more time, the synthetic transmit aperture simulation scripts could be modified to reflect these refinements. It would also be interesting to compare results obtained using a few different variations on the sequence of transmitting elements and signals, as was discussed briefly in Chapter 6.

References

[1] A. Mertins, *Signal Analysis: Wavelets, Filter Banks, Time-Frequency Transforms and Applications*, ch. 2. John Wiley & Sons Ltd., 1999.

[2] T. L. Szabo, *Diagnostic Ultrasound Imaging: Inside Out*, ch. 3. Elsevier Academic Press, 2004.

[3] D. M. Howard and J. Angus, *Acoustics and psychoacoustics*, ch. 2. Focal Press, 2 ed., 2001.

[4] T. L. Szabo, *Diagnostic Ultrasound Imaging: Inside Out*, ch. Appendix B. Elsevier Academic Press, 2004.

[5] M. H. Repacholi and D. A. Benwell, *Essentials of Medical Ultrasound: A Practical Introduction to the Principles, Techniques and Biomedical Applications*, ch. 1. Humana Press, 1982.

[6] F. A. Duck, A. Baker, and H. Starritt, *Ultrasound in Medicine (Medical Science)*, ch. 1. Taylor & Harris, 1998.

[7] K. K. Shung, *Diagnostic Ultrasound: Imaging and Blood Flow Measurements*, ch. 3. CRC Press, 2005.

[8] K. K. Shung, *Diagnostic Ultrasound: Imaging and Blood Flow Measurements*, ch. 2. CRC Press, 2005.

[9] K. Asafusa, T. Azuma, R. Shinomura, H. Kanda, and S. Umernura, "Ultrasound imaging system using combinational coded excitation," in *Proceedings of the IEEE Ultrasonics Symposium*, pp. 2045 – 2048, IEEE, IEEE, 2004.

[10] R. Barker, "Group synchronizing of binary digital sequences," in *Communications Theory*, pp. 273 – 287, Butterworth, 1953.

[11] S. Nikolov, *Users' guide for the beamformation toolbox*, August 2000.

[12] M.-H. Bae, W.-Y. Lee, M.-K. Jeong, and S.-J. Kwon, "Orthogonal golay code based ultrasonic imaging without reducing frame rate," in *Proceedings of the IEEE Ultrasonics Symposium*, vol. 2, pp. 1705–1708, IEEE, IEEE, 2002.

[13] M. Bennett, *Signal Processing Techniques for Ultrasonic Tissue Doppler and Real-time B-mode Imaging in Cardiology*. PhD thesis, The University of Edinburgh, March 2005.

[14] R. Bjerngaard and J. A. Jensen, "Should compression of coded waveforms be done before or after focusing?," *Medical Imaging 2002: Ultrasonic Imaging and Signal Processing*, vol. 4687, no. 1, pp. 47–58, 2002.

[15] P. Brands, A. Hoeks, and L. Ledoux, "A radio-frequency domain complex cross-correlation model to estimate blood flow velocity and tissue motion by means of ultrasound," *Ultrasound in Medicine and Biology*, pp. 911–920, 1997.

[16] A. Brenner, K. Eck, W. Wilhelm, and T. Noll, "Improved resolution and dynamic range in medical ultrasonic imaging using depth-dependent mismatched filtering," in *Proceedings of the IEEE Ultrasonics Symposium*, vol. 2, pp. 1475 – 1480, IEEE, IEEE, October 1997.

[17] D. Cathignol, "Signal-to-clutter ratio in pseudo random doppler flowmeter," *Ultrasonic Imaging*, vol. 8, pp. 272–284, October 1986.

[18] R. Chiao, L. Mo, A. Hall, S. Miller, and K. Thomenius, "B-mode blood flow (b-flow) imaging," in *Proceedings of the IEEE Ultrasonics Symposium*, vol. 2, pp. 1469 – 1472, IEEE, IEEE, Oct 2000.

[19] R. Chiao and X. Hao, "Coded excitation for diagnostic ultrasound: A system developer's perspective," *IEEE Transactions on Ultrasonics, Ferroelectrics and Frequency Control*, vol. 52, pp. 160 – 170, February 2005.

[20] R. Chiao and L. Thomas, "Synthetic transmit aperture imaging using orthogonal golay coded excitation," in *Proceedings of the IEEE Ultrasonics Symposium*, pp. 1677 – 1680, IEEE, IEEE, 2000.

[21] M. J. Bennett, "Development of an automated test rig," tech. rep., BIAS Consortium, 2007.

[22] K. Hynynen and N. McDannold, "Focused ultrasound for the treatment of patients with cancer," *Progress in Oncology*, pp. 269 – 289, 2004.

[23] D. Gunn, P. Jackson, M. Lovell, S. Assous, C. Hopper, and L. Linnett, "Physical properties characterisation rig," tech. rep., BIAS consortium, 2007.

[24] P. De Jong, T. Arts, A. Hoeks, and R. Reneman, "Determination of tissue motion velocity by correlation interpolation of pulsed ultrasonic echo signals," *Ultrasonic Imaging*, vol. 12, pp. 84 – 98, April 90.

[25] C. Deane, "Safety of diagnostic ultrasound in fetal scanning," in *Doppler in obstetrics*, Centrus, 2002.

[26] C. Dolph, "A current distribution for broadside arrays which optimizes the relationship between beam width and side-lobe level," *Proceedings of the IRE*, vol. 34, pp. 335–348, June 1946.

[27] F. A. Duck, "Medical and non-medical protection standards for ultrasound and infrasound," *Progress in Biophysics and Molecular Biology*, vol. 93, no. 1-3, pp. 176–191, 2007.

[28] EC, "Council directive 93/42/eec of 14 june 1993 concerning medical devices," *Official Journal of the European Communities*, July 1993.

[29] K. Eck, R. Schwann, A. Brenner, and T. Noll, "Depth-dependent mismatched filtering using ultrasonic attenuation as a filter design parameter," in *Proceedings of the IEEE Ultrasonics Symposium*, vol. 2, pp. 1639–1644, IEEE, IEEE, 1998.

[30] D. Evans and W. McDicken, *Doppler Ultrasound*. John Wiley & Sons Ltd., 2nd edition ed., 2000.

[31] FDA, "Information for manufacturers seeking marketing clearance of diagnostic ultrasound systems and transducers," tech. rep., U.S. Food and Drug Administration, U.S. Dept. of Health and Human Services, Food and Drug Administration, Center for Devices and Radiological Health, September 2008.

[32] J. Jensen, "Linear description of ultrasound imaging systems," tech. rep., Technical University of Denmark, June 2001.

[33] J. Jensen, *User's guide for the Field II program*. Technical University of Denmark, 2.86 ed., August 2001.

[34] S. Foster, P. Embree, and W. O'Brien Jr., "Flow velocity profile via time-domain correlation: error analysis and computer simulation," *IEEE Transactions on Ultrasonics, Ferroelectrics and Frequency Control*, vol. 37, no. 3, pp. 164–175, May 1990.

[35] D. L. Franklin, W. Schlegel, and R. F. Rushmer, "Blood flow measured by doppler frequency shift of back-scattered ultrasound," *Science*, vol. 134, pp. 564–565, August 1961.

[36] J. Gao and D. Liu, "Ultrasound flow motion detection using reverse golay codes for decoding," in *International Conference on Bioinformatics and Biomedical Engineering 2007, Proceedings*, pp. 1253 – 1256, 2007.

[37] M. Golay, "Complementary series," *IEEE Transactions on Information Theory*, vol. 7, no. 2, pp. 82–87, Apr 1961.

[38] Y. Gorfu, *Development of a Low-Power Ultrasonic Data Acquisition and Imaging System*. PhD thesis, University of Strathclyde, 1988.

[39] F. Gran and J. Jensen, "Designing waveforms for temporal encoding using a frequency sampling method," *Ultrasonics, Ferroelectrics and Frequency Control, IEEE Transactions on*, vol. 54, pp. 2070–2081, October 2007.

[40] F. J. Harris, "On the use of windows for harmonic analysis with the discrete fourier transform," *Proceedings of the IEEE*, vol. 66, pp. 51 – 83, January 1978.

[41] I. Hein and W. O'Brien Jr., "Current time-domain methods for assessing tissue motion by analysis from reflected ultrasound echoes-a review," *IEEE Transactions on Ultrasonics, Ferroelectrics and Frequency Control*, vol. 40, pp. 84–102, March 1993.

[42] Y. Hirao, K. Tamukai, Y. Kinouchi, and H. Yamaguchi, "Synchronized measurements of blood flow velocity distributions in carotid, brachial and femoral arteries, and ecg in human during exercise," in *[Engineering in Medicine and Biology, 1999. 21st Annual Conf. and the 1999 Annual Fall Meeting of the Biomedical Engineering Soc.] BMES/EMBS Conference, 1999. Proceedings of the First Joint*, vol. 1, pp. 224 vol.1–, 1999.

[43] A. Hoeks, P. Brand, T. Arts, and R. Reneman, "Subsample volume processing of doppler ultrasound signals," *Ultrasound in Medicine and Biology*, vol. 20, no. 9, pp. 953 – 965, 1994.

[44] A. P. Hoeks, T. G. Arts, P. Brands, and R. Reneman, "Comparison of the performance of the rf cross correlation and doppler autocorrelation technique to estimate the mean velocity of simulated ultrasound signals," *Ultrasound in Medicine and Biology*, vol. 19, pp. 727 – 740, June 1993.

[45] P. Hoskins and W. McDicken, "Colour ultrasound imaging of blood flow and tissue motion," *British Journal of Radiology*, vol. 70, pp. 878–890, September 1997.

[46] J. Hossack, "Introduction to the special issue on coded waveforms," *Ultrasonics, Ferroelectrics and Frequency Control, IEEE Transactions on*, vol. 52, pp. 158–159, Feb. 2005.

[47] D. H. Howry, D. A. Sott, and W. R. Bliss, "The ultrasonic visualization of carcinoma of the breast and other soft tissue structures," *Cancer*, vol. 7, pp. 354–358, March 1954.

[48] K. Hoyt, F. Forsberg, and J. Ophir, "Comparison of shift estimation strategies in spectral elastography," *Ultrasonics*, vol. 44, pp. 99 – 108, January 2006.

[49] IEC, "Iec 60601-2-37 edition 2.0 2007-08 medical electrical equipment – part 2-37: Particular requirements for the basic safety and essential performance of ultrasonic medical diagnostic and monitoring equipment," tech. rep., Internation Electrotechnical Commission, August 2007.

[50] C. Kasai, K. Namekawa, A. Koyano, and O. R., "Real-time two-dimensional blood flow imaging using an autocorrelation technique," *IEEE Transactions on Ultrasonics, Ferroelectrics and Frequency Control*, vol. 32, pp. 458–464, May 1985.

[51] B.-H. Kim, T.-H. Kim, and T.-K. Song, "Generation of mutually orthogonal polyphase complementary sequences for use in ultrasound imaging," in *Proceedings of the IEEE Ultrasonics Symposium*, vol. 2, pp. 1693–1696, IEEE, IEEE, October 2002.

[52] B.-H. Kim, G.-D. Kim, and T.-K. Song, "A post-compression based ultrasound imaging technique for simultaneous transmit multi-zone focusing," *Ultrasonics*, vol. 46, no. 2, pp. 148–154, 2007.

[53] X. Lai, H. Torp, and K. Kristoffersen, "An extended autocorrelation method for estimation of blood velocity," *IEEE Transactions on Ultrasonics, Ferroelectrics and Frequency Control*, vol. 44, pp. 1332 – 1342, Nov 1997.

[54] X. Lai and H. Torp, "Interpolation methods for time-delay estimation using cross-correlation method for blood velocity measurement," *IEEE Transactions on Ultrasonics, Ferroelectrics and Frequency Control*, vol. 40, pp. 277 – 290, March 1999.

[55] S. Langeland, J. D'hooge, H. Torp, B. Bunens, and P. Suetens, "Comparison of time-domain displacement estimators for two-dimensional rf tracking," *Ultrasound in Medicine and Biology*, vol. 29, pp. 1177 – 1186, April 2003.

[56] C. Leavens, R. Willams, P. Burns, and M. Sherar, "The use of phase codes in ultrasound imaging: Snr gain and bandwidth requirements," *Applied Acoustics*, vol. In Press, Corrected Proof, pp. –, 2008.

[57] P.-C. Li, E. Ebbini, and M. O'Donnell, "A new filter design technique for coded excitation systems," *IEEE Transactions on Ultrasonics, Ferroelectrics and Frequency Control*, vol. 39, no. 6, pp. 693 – 699, 1992.

[58] T. Loupas, J. Powers, and R. Gill, "An axial velocity estimator for ultrasound blood flow imaging, based on a full evaluation of the doppler equation by means of a two-dimensional autocorrelation approach," *IEEE Transactions on Ultrasonics, Ferroelectrics and Frequency Control*, vol. 42, pp. 672 – 688, July 1995.

[59] T. Loupas, R. Peterson, and R. Gill, "Experimental evaluation of velocity and power estimation for ultrasound blood flow imaging, by means of a two-dimensional autocorrelation approach," *IEEE Transactions on Ultrasonics, Ferroelectrics and Frequency Control*, vol. 42, pp. 689 – 699, July 1995.

[60] P. Lynch, "The dolph-chebyshev window: A simple optimal filter," *Proceedings of the American Meteorological Society*, vol. 125, pp. 655–660, April 1997.

[61] K. Miller and M. Rochwarger, "A covariance approach to spectral moment estimation," *IEEE Transactions on Information Theory*, vol. 18, pp. 588–596, 1972.

[62] T. Misaridis and J. Jensen, "Use of modulated excitation signals in medical ultrasound. part i: basic concepts and expected benefits," *IEEE Transactions on Ultrasonics, Ferroelectrics and Frequency Control*, vol. 52, pp. 177 – 191, Feb 2005.

[63] T. Misaridis and J. Jensen, "Use of modulated excitation signals in medical ultrasound. parts i – iii," *IEEE Transactions on Ultrasonics, Ferroelectrics and Frequency Control*, vol. 52, pp. 177 – 219, Feb 2005.

[64] T. Misaridis and J. Jensen, "Use of modulated excitation signals in medical ultrasound. part ii: design and performance for medical imaging applications," *IEEE Transactions on Ultrasonics, Ferroelectrics and Frequency Control*, vol. 52, pp. 192 – 207, Feb 2005.

[65] T. Misaridis and J. Jensen, "Use of modulated excitation signals in medical ultrasound. part iii: high frame rate imaging," *IEEE Transactions on Ultrasonics, Ferroelectrics and Frequency Control*, vol. 52, pp. 208 – 219, Feb 2005.

[66] V. Newhouse, K. Dickerson, D. Cathignol, and J. Chapelon, "Three-dimensional vector flow estimation using two transducers and spectral width," *IEEE Transactions on Ultrasonics, Ferroelectrics and Frequency Control*, vol. 41, pp. 90–95, January 1994.

[67] V. Newhouse and J. Reid, "Invariance of doppler bandwidth with flow axis displacement," in *Proceedings of the IEEE Ultrasonics Symposium*, vol. 3, pp. 1533–1536, IEEE, IEEE, December 1990.

[68] S. Nikolov, K. Gammelmark, and J. Jensen, "Recursive ultrasound imaging," *Proceedings of the IEEE Ultrasonics Symposium*, vol. 2, pp. 1621–1625 vol.2, 1999.

[69] S. Nikolov, *Synthetic aperture tissue and flow ultrasound imaging*. PhD thesis, Center for Fast Ultrasound Imaging, Technical Unviersity of Denmark, August 2001.

[70] C. Oakley, "Calculation of ultrasonic transducer signal-to-noise ratios using the klm model," *Ultrasonics, Ferroelectrics and Frequency Control, IEEE Transactions on*, vol. 44, pp. 1018 – 1026, Sep 1997.

[71] W. D. O'Brien Jr., "Assessing the risks for modern diagnostic ultrasound imaging," *Japanese Journal of Applied Physics*, vol. 37, pp. 2781–2788, 1998.

[72] M. O'Donnell, "Coded excitation system for improving the penetration of real-time phased-array imaging systems," *IEEE Transactions on Ultrasonics, Ferroelectrics and Frequency Control*, vol. 39, pp. 341–351, May 1992.

[73] M. O'Donnell and Y. Wang, "Coded excitation for synthetic aperture ultrasound imaging," *IEEE Transactions on Ultrasonics, Ferroelectrics and Frequency Control*, vol. 52, no. 2, pp. 171 – 176, 2005.

[74] A. V. Oppenheim and R. W. Schafer, *Discrete-time signal processing*. Prentice Hall, 1989.

[75] P. Pallav, T. Gan, and D. Hutchins, "Elliptical-tukey chirp signal for high-resolution, air-coupled ultrasonic imaging," *IEEE Transactions on Ultrasonics, Ferroelectrics and Frequency Control*, vol. 54, pp. 1530 – 1540, September 2007.

[76] A. D. Pierce, *Acoustics: An introduction to its physical principles and applications*, ch. 1. American Institute of Physics, 2 ed., 1989.

[77] J. G. Proakis and D. G. Manolakis, *Digital Signal Processing*. International Editions, Prentice Hall, 3rd ed., 1996.

[78] N. Levanon and E. Mozeson, *Radar Signals*. John Wiley & Sons, 2004.

[79] J. Rubin, "Spectral doppler us," *Radiographics*, vol. 14, no. 1, pp. 139 – 150, 1994.

[80] S. Satomura, "Study of the flow pattern in peripheral arteries by ultrasonics," *Journal of the Acoustic Society of Japan*, pp. 151 – 158, June 1959.

[81] M. Schlaikjer, S. Torp-Pedersen, and J. Jensen, "Simulation of rf data with tissue motion for optimizing stationary echo canceling filters," *Ultrasonics*, vol. 41, pp. 415 – 419, 2003.

[82] M. Schlaikjer, S. Petersen, J. Jensen, and P. Stetson, "Tissue motion in blood velocity estimation and its simulation," in *Proceedings of the IEEE Ultrasonics Symposium*, vol. 2, pp. 1495–1499, IEEE, IEEE, Oct 1998.

[83] W. Siebert, "The early history of pulse compression radar-the development of an/fps-17 coded-pulse radar at lincoln laboratory," *Aerospace and Electronic Systems, IEEE Transactions on*, vol. 24, pp. 833–837, Nov 1988.

[84] P. Stepanishen, "The time-dependent force and radiation impedance on a piston in a rigid infinite planar baffle," *Journal of the Acoustical Society of America*, vol. 49, pp. 841–849, 1971.

[85] P. Stepanishen, "Transient radiation from pistons in an infinite planar baffle," *Journal of the Acoustical Society of America*, vol. 49, pp. 1629–1638, 1971.

[86] Y. Takeuchi, "An investigation of a spread energy method for medical ultrasound systems. part one: theory and investigation.," *Ultrasonics*, vol. 17, pp. 175 – 182, July 1979.

[87] Y. Takeuchi, "An investigation of a spread energy method for medical ultrasound systems. part two: proposed system and possible problems.," *Ultrasonics*, vol. 17, pp. 219 – 224, September 1979.

[88] G. Tupholme, "Generation of acoustic pulses by baffled plane pistons," *Mathematika*, vol. 16, pp. 209–224, 1969.

[89] F. Viola and W. Walker, "A comparison of the performance of time-delay estimators in medical ultrasound," *IEEE Transactions on Ultrasonics, Ferroelectrics and Frequency Control*, vol. 50, pp. 392–401, April 2003.

[90] F. Viola and W. Walker, "A spline-based algorithm for continuous time-delay estimation using sampled data," *IEEE Transactions on Ultrasonics, Ferroelectrics and Frequency Control*, vol. 52, pp. 80–93, January 2005.

[91] R. Waag, J. Myklebust, W. Rhoads, and R. Gramiak, "Instrumentation for noninvasive cardiac chamber flow rate measurement," in *Proceedings of the IEEE Ultrasonics Symposium*, pp. 74–77, IEEE, IEEE, 1972.

[92] Y. Wang, K. Metzger, D. Stephens, G. Williams, S. Brownlie, and M. O'Donnell, "Coded excitation with spectrum inversion (cexsi) for ultrasound array imaging," *IEEE Transactions on Ultrasonics Ferroelectrics and Frequency Control*, vol. 50, pp. 805 – 823, July 2003.

[93] J. Wilhjelm and P. Pedersen, "Target velocity estimation with fm and pw echo ranging doppler systems - part i: Signal analysis," *IEEE Transactions on Ultrasonics, Ferroelectrics and Frequency Control*, vol. 40, no. 4, pp. 366 – 372, 1993.

[94] J. Wilhjelm and P. Pedersen, "Target velocity estimation with fm and pw echo ranging doppler systems - part ii: Systems analysis," *IEEE Transactions on Ultrasonics, Ferroelectrics and Frequency Control*, vol. 40, no. 4, pp. 373 – 380, 1993.

[95] J. Wilhjelm and P. Pedersen, "Comparisons between pw doppler system and enhanced fm doppler system," in *Proceedings of the IEEE Ultrasonics Symposium*, pp. 1548 – 1551, IEEE, IEEE, 1995.

[96] J. Woo, "A short history of the development of ultrasound in obstetrics and gynaecology." Website, 2002. http://www.ob-ultrasound.net/history1.html.

[97] E. Yoxen, "Seeing with sound: A study of the development of medical images," in *The social construction of technological systems. New directions in the sociology and history of technology* (W. E. Bijker, T. P. Hughes, and T. J. Pinch, eds.), The MIT Press, 1987.

[98] H. Zhao, L. Mo, and S. Gao, "Barker-coded ultrasound color flow imaging: theoretical and practical design considerations," *IEEE Transactions on Ultrasonics Ferroelectrics and Frequency Control*, vol. 54, pp. 319 – 331, February 2007.

Publications

[99] C. Cannon, J. Hannah, and S. McLaughlin, "Segmented motion compensation for complementary coded ultrasonic imaging," *Accepted for publication in IEEE Transactions on Ultrasonics, Ferroelectrics and Frequency Control*, May 2010.

[100] C. Cannon, J. Hannah, and S. McLaughlin, "Mirrored motion compensation for complementary-coded medical ultrasonic imaging," in *Proceedings of the IEEE International Ultrasonics Symposium*, IEEE, November 2008.

[101] C. Cannon, J. Hannah, and S. McLaughlin, "Motion compensated complementary coding for medical ultrasound," in *Proceedings of the IEC Irish Signals and Systems Conference*, IEEE, November 2008.